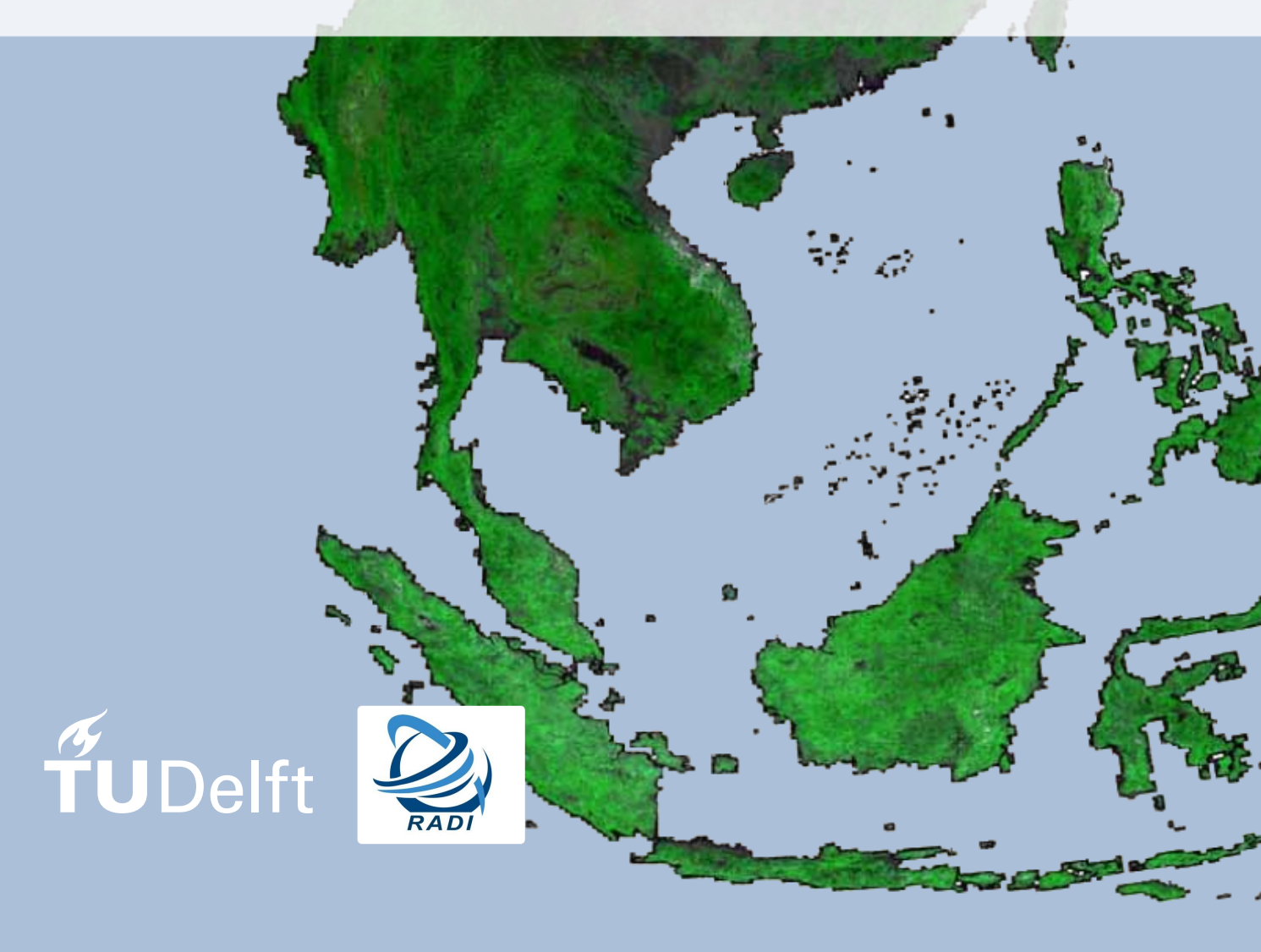


Performance evaluation of the CWI BRDF-fitting method under cloud-contaminated conditions

A numerical experiment using PROSAIL

J.N.N. Klein



Performance evaluation of the CWI BRDF-fitting method under cloud-contaminated conditions

A numerical experiment using PROSAIL

by

J.N.N. Klein

to obtain the degree of Master of Science at the Delft University of Technology. to be defended publicly on Friday July 3rd, 2020 at 09:45 AM.

Student number: 4110692

Project duration: March 27, 2018 – July 3, 2020

Thesis committee: Prof. dr. M. Menenti (chair), TU Delft, RADI, CAS

Prof. dr. LIU Qinhuo, RADI, CAS
Dr. S. L. M. Lhermitte, TU Delft
Dr. R. C. Lindenbergh, TU Delft

An electronic version of this thesis is available at http://repository.tudelft.nl/.



Preface

The following master thesis project is my graduation project from the MSc track Geoscience and Remote Sensing, a program followed at the faculty of Civil Engineering and Geosciences, Delft University of Technology. During this master's program several topics of remote sensing were covered, and the fields which interested me the most were surface reflectance retrieval and NDVI estimation. As one of multiple ways in which we monitor the Earth's surface, it seemed particularly relevant in the context of the climate crisis we are facing.

The subject of this thesis is the Changing Weight-Iterative (CWI) algorithm for the fitting of bidirectional reflectance distribution functions (BRDF), published [61] by Yelu Zeng at the Institute of Remote Sensing and Digital Earth (RADI) under the supervision of Professor Liu Qinhuo and dr. Li Jing. Their research team is part of the State Key Laboratory of Remote Sensing Science, RADI, Chinese Academy of Sciences (CAS). And for a period of 12 months, I was fortunate to be hosted by the team in Beijing, China, while I conducted research on the performance of the CWI algorithm. The exact topic and focus of the thesis was formed over this period of time, and finalised upon my return to the Netherlands, with guidance from my thesis supervisor Prof. dr. Massimo Menenti. Thank you Massimo, for all the discussions and the advice you have given me over the course of this project.

I would also like to thank Professor Liu Qinhuo and dr. Li Jing, for welcoming me into their research team and making me feel at home in RADI. Visiting China, let alone living in the country, had never crossed my mind before so I didn't know what to expect. Looking back on it, I don't have a single regret - and I am very grateful for the truly life-changing opportunity. Also a special thanks to Roderik and Stef, not only for the very interesting courses you taught during the master's programme, but for agreeing to be on my thesis committee. Thank you Sandra for your support as the coordinator of the GRS track, and also for the courses (and observation theory MOOC which we worked together on!). I would be remiss not to also mention my Data & Technology colleagues at EY, whom I would like to thank for their support and mentorship.

Finally, a short paragraph dedicated to my friends, and to my loving and supporting family: Sonam, Julie, Tsewang, Kinley and Ama and Apa. Thank you for being just that, my family. Excellent work all-round. To my friends: I would like to think that I wear my heart on my sleeve, and that you are all already aware of how much I appreciate you sticking around with me. I can proudly say that there are too many of you to list here. I still consider myself close to all the friends I have made, from all the paths I have walked in my life thus far, from the Hague, to Delft, Austin, Beijing and of course Bhutan.

Thank you, dank je, merci, xièxie, kadrinche!

J.N.N. Klein Utrecht, June 2020

Abstract

Remote retrieval of Normalized Difference Vegetation Index (NDVI) over the Earth's surface is a critical component of monitoring the surface processes of our planet. NDVI is a widely used and useful indicator of vegetation health and quantity - however its retrieval using satellite data is hindered by the frequent presence of clouds in the Earth's atmosphere. These can block or severely contaminate measurements of the red and near-infrared (NIR) band reflectances, the bands on which NDVI is based. A common method to avoid this is to create a composite value from multiple observations retrieved over several days, by reconstructing the surface's bidirection reflectance distribution function (BRDF) and using it to calculate the NDVI at a standardized geometry.

Zeng et al. [61] developed a novel technique that estimates a susrfaces's Bidirectional Reflectance Distribution Function (BRDF) with a Ross-Li-Maignan (RLM) model from a set of observations. This method, the Changing-Weight Iterative (CWI) method, use iterative *a posteriori* estimation of observations errors to reduce the impact of cloud-contaminated measurements in the sample. Its performance was comapred to two conventional methods, ordinary-least squares (OLS) and Li-Gao[11] methods.

The three different BRDF-fitting methods and their ability to reduce the impact of noisy observations were compared in a numerical experiment. 6,000 surfaces covering a broad range of surface types were modeled using the canopy radiative transfer model PROSAIL. For each surface, sets of pseudo-observations of the surface's red and NIR band reflectance were generated using realistic sun-target-view geometries from the MODIS and MERSI satellite sensors.

The effects of cloud-contamination were simulated by adding different numbers of cloud-contaminated observation (α) to the sample, with varying degrees of contamination (f_c). The RLM BRDF model was fitted to these samples using the three different methods. These were subsequently used to calculate a NDVI composite value.

Each method's estimate was compared to a reference-value generated by PROSAIL. Results for the 6,000 surfaces confirmed that the CWI method is more noise-resistant than OLS and Li-Gao in situations with many observations (i.e. a large sample), and resulted in estimates that more closely matched the reference values from PROSAIL, compared to the conventional Li-Gao and OLS methods.

In scenarios of low-cloud contamination, all three methods failed to detect and significantly suppress the impact of noisy observations, which was expected from existing literature [11].

For a large-sized sample of 13 pseudo-observations studied for the validation site Mongu, Zambia, the CWI method was observed to have a very accurate performance, for up to 5 contaminated observations ($\alpha=5$) in the sample. With smaller sized samples of 8 and 10 for two other validation sites, it was found that the RMSE of the CWI method would suddenly increase approximately tenfold when α increased beyond 2 and 3, respectively. After these 'tipping points', the Li-Gao method was more accurate and outperformed CWI.

The CWI method therefore performed promisingly when given a large enough sample size, and in these cases it was more accurate than the conventional Li-Gao and OLS methods. However, when it fails to correctly identify noisy observations, its accuracy could decrease suddenly, which should be taken into consideration for operational use. Since the results of the experiment were averaged over 6,000 different sampling points of the PROSAIL model's parameter space, it is suggested that the conclusions apply to a wide range of surface types found all over the Earth.

Contents

Lis	st of	Figures	ix
Lis	st of	Tables	xiii
No	men	clature	χv
1	Intro	oduction	1
2	The 2.1	ory: NDVI Retrieval and Surface BRDF Estimation Surface reflectance anisotropy	
	2.2	NDVI and clouds	. 7
		NDVI compositing	. 11
	2.4	MuSyQ	. 12
	2.5	BRDF fitting methods	. 14 . 15
		Validating BRDF estimates	. 19 . 19
		Theory - conclusion	
3	Met l 3.1	hodology: Numerical Experiment Using PROSAIL Roadmap	23
		Assumptions made	
		Creating a set of representative surfaces	
	5.5	3.3.1 Removing unrealistic surfaces	
	3 4	Extracting actual geometry	
	0	3.4.1 Pre-screening	
	3.5	Simulating pseudo-observations and determining reference BRDF model parameters 3.5.1 Baseline Ross-Li-Maignan BRDF model fitting	. 29
	3.6	Cloud noise contamination scenarios / Noise contamination	
	3.7 3.8	Estimating Ross-Li-Maignan model with OLS, LiGao and CWI methods	
4	Res	ults and Discussion	35
		Clear-sky conditions	. 37 . 39 . 39
	4.2	Estimating from noisy samples	. 41 . 42

viii Contents

		4.3 Evaluating the experiment	48 49 50			
	5	Conclusion and Recommendations 5.1 Conclusion	53 54			
I	Ар	pendices	57			
	A	PROSAIL input variables				
	В	Variance of RLM model parameters	62			
	С	Comparison of estimated nadir-normalised NDVI to reference - noisefree case	63			
	D	BRDF parameters estimates	65			
	Ε	Comparison of estimated nadir-normalised NDVI to reference - Low cloud contamination				
	F	Comparison of estimated nadir-normalised NDVI to reference - Medium cloud contamination	71			
	G	Comparison of estimated nadir-normalised NDVI to reference - High cloud contamination	76			
	Н	Tables of RMSE analysis results	81			
	Bil	bliography	83			

List of Figures

2.1	Scattered radiation by a perfectly Lambertian surface and a non-Lambertian surface	6
2.2	Diagram of the bidirectional reflectance factor BRF, adapted from [19]	7
2.3	Red band reflectance of a surface covered with vegetation canopy, simulated by radiative transfer model PROSAIL. The directionality effect is clearly visible as the reflectance varies with viewing zenith angle. Including background soil in the simulation (blue line) further adds a directionality effect, as the proportion of soil reflectance in the signal varies with viewing angle.	7
2.4	Spectrum of solar radiation for Earth. Comparison of the irradiance of sunlight as observed at the top of the atmosphere (yellow line), and at sea level (red line). Taken from [7]	8
2.5	Atmospheric effect and TOA reflectance illustrated. Figure taken from [36]	8
2.6	Reflectance in the red and NIR bands and corresponding NDVI value for healthy vegetation compared to stressed vegetation. The stressed vegetation exhibits a lower absorption in the red band, and higher reflectance in the NIR, resulting in a lower NDVI.	9
2.7	Model map of cloud-free, cloud shadow, and cloud pixels taken from [58]	9
2.8	3-year time series of MODIS sensor NDVI data, overlaid with two different smoothened trends. A seasonal variation in NDVI is observed, as is expected for most surfaces, with higher NDVI values in warm months and lower values in the colder months. Noise due to cloud-contamination and other atmospheric effects lead to lower measured NDVI values, causing temporal discontinuities that cannot be attributed to smooth seasonal changes.	
0.0		10
2.9	Diagram of multiple observations of the same surface, taken at different points in time, and at different sun-target-view geometries	11
2.10	A single NDVI composite value is formed from a sample. In this case, the NDVI is standardised to a sun-target-view geometry with nadir-viewing, fixed solar zenith angle $(\theta_S = 30^\circ)$	12
2.11		12
2.12	BRF anisotropy of an example surface modelled using the Ross-Li parametric BRDF model. Shown here for the wavelengths of the MODIS sensor's band 3 $\lambda=459-479nm$. Left: Variation in reflectance along the principal plane (illumination direction and viewing direction in same vertical plane), with varying θ_V . Right: polar plot of surface reflectance for fixed illumination zenith angle $\theta_S=30^\circ$, θ_V between 0° and 45° and ϕ_r between 0° and 360° . Taken from [28]	14
2.13	Weights assigned to each observation in a sample according to the Li-Gao BRDF fitting method. The NDVI value highlighted in red is a cloud-contaminated observation with a NDVI significantly lower than the mea NDVI value of all observations. Its weight is reduced according to equations 2.10 and 2.12. Adapted from Gao et al. (2002)[11]	16
2.14	Flowchart of the Changing-Weight Iterative (CWI) BRDF fitting method . Adapted from [61]	17
2.15	Dual-view goniometer system used to take field BRDF measurements. Adapted from [40].	19
2.16	Simulating bidirectional reflectance factor for a canopy using the PROSAIL model. Leaf transmittance and scattering as modelled by PROSPECT is passed on as input to the	24
	SAIL canopy model to which it is coupled [5]	21

x List of Figures

3.1	in the top row are the types of variables used: variables describing the canopy and background soil types (inputs for PROSPECT and SAIL), variables describing the suntarget-view observation geometry (input for SAIL) and variables describing the different cloud contamination scenarios. The pseudo-observations simulated with PROSAIL form noise-free samples of the surfaces' BRDFs, and these are combined with the reflectance of cloudy pixels using a linear spectral mixing model (not shown here, see subsection 3.6 for details on simulated noise). For each surface in total 15 noisy samples are simulated, and for each one the Ross-Li-Maignan BRDF model parameters are estimated	
2.0	using the OLS, Li-Gao, and CWI fitting methods	25
3.2	curve was drawn in the 'corners' of the joint distribution, selecting surfaces at the edges of the bi-variate parameter space to be removed	27
3.3	Grayscale image of band 1 of a single MODIS image tile, overlaid on a Google Earth image of northeastern China.	28
3.4	Reflectance spectrum from 400 to 2500 (nm) for a vegetated surface with $NDVI = 0.9$ and acquisition geometry of $(\theta_V, \theta_S, \phi_r) = (0, 30, 0)$, as simulated by PROSAIL	30
3.5	Spectral Response Function (SRF) of MODIS Aqua sensor overlaid on surface reflectance spectrum as simulated by PROSAIL	31
3.6	Comparison of noise-free (blue points) pseudo-observations in sample and contaminated observations (red points). Generated along principal plane ($\phi_r=0$) so that the v-shaped directionality is clearly visible, as well as the red points deviation from it. The observations are contaminated with a low cloud fraction of $f_c=0.5\%$ using the linear spectral mixing model	32
3.7	Spread of BRDF model parameters $(f_{iso}, f_{vol}, f_{geo})_{CWI}$ estimated using the CWI method. For each permutation of 2 noisy measurements, a noisy sample was calculated according to the method described in section 3.6. The histogram visualises the distribution of possible estimates, depending on which random 2 pseudo-obervatios are contaminated. The median value of each coefficient was used as the resulting estimate for the given surface and scenario.	33
4.1	Skyplot of all valid MODIS and MERSI measurements for a single pixel containing the study site. 8 observations were extracted for the site Chang Baishan (China), 10 for Harvard Forest (USA), and 13 for Mongu (Zambia). The pixel closest to the site was used. Red squares indicate retrievals from the MODIS sensor, while blue triangles are from the MERSI sensor.	36
4.2	Histogram of possible RLM model parameter estimates from noise-free sample for the NIR band. Shown here for a single surface, for site Harvard Forest. Each triplet of observations within the sample yielded one set of solutions $(f_{iso}, f_{vol}, f_{geo})_e$. The coefficients are all focused on narrow bands of values with some outliers, with low variances	37
4.3	of $(\sigma_{f_{iso}}^2, \sigma_{f_{geo}}^2, \sigma_{f_{geo}}^2) = (3.55e-8, 2.15e-6, 2.99e-7)$	38
4.4	Side by side comparison of a noise-free sample as simulated by PROSAIL, compared to same observations as calculated by a fitted RLM model. The model parameters used are the median of the spread shown in figure 4.2, which had a narrow spread within the estimates. The RMSE of the estimated NDVI is 0.0083.	38
4.5	Side by side comparison of surface reflectance pseudo-observations as simulated by PROSAIL, compared to reflectance as calculated by the RLM model fitted to the noise-free sample. The model parameters used are for a surface with high variance in the estimated kernel coefficients. The RMSE of the estimated NDVI is 0.0942	38
4.6	Distribution of RLM BRDF model parameters from noise-free samples, for 6,000 surfaces. Angular sampling is for the site Harvard Forest.	39
	iaoco. Angulai bamping ib ioi the bite marvaru i olebt	J

List of Figures xi

4.7	Scatter plot of estimated NDVI compared to reference NDVI value from PROSAIL, for site Harvard Forest. Shown here are NDVI values calculated using BRDF parameters estimated from noise-free samples using OLS, Li-Gao, and CWI methods. Dotted line is 1:1 line, green lines are $\pm 5\%$.	40
4.8	Direct validation of CWI method using imagery from the ETM+ sensor, Harvard Forest site, as reported by Zeng et al. [61].	41
4.9	Estimates of the red band kernel coefficients, for the scenario $(\alpha, f_c) = (2, 3.0\%)$ at site Harvard Forest. Top: distributions of the baseline f_{iso} parameters and OLS, Li-Gao, and CWI estimates. Bottom: distributions of deviations from baseline f_{iso} values for OLS, Li-Gao, and CWI estimates. Note the scale of the x-axis.	42
4.10	Same as figure 4.9, for $\alpha=5$, at site Harvard Forest. Top: distributions of the baseline f_{iso} parameters and OLS, Li-Gao, and CWI estimates. Bottom: distributions of deviations from baseline f_{iso} values for OLS, Li-Gao, and CWI estimates. Note the scale of the x-axis.	43
4.11	Estimated nadir-normalised NDVI versus reference PROSAIL values for study site Harvard Forest - for the case of low noise $f_c=0.5\%$. Fitted RLM BRDF models were used to calculate the NDVI values, using the fitting methods OLS (left), LiGao (middle), CWI (right). Angular spread of the 10 observations used for the BRDF fitting can be seen in 4.1b.	
	Each point represents the calculated values for one surface type, the black dotted line a 1:1 relationship and the green dotted indicates the threshold for the references values $\pm 5\%$	45
4.12	Estimated nadir-normalised NDVI versus reference PROSAIL values for study site Harvard Forest - for the case of high noise $f_c=3.0\%$. Fitted RLM BRDF models were used to calculate the NDVI values, using the fitting methods OLS (left), LiGao (middle), CWI (right). Angular spread of the 10 observations used for the BRDF fitting can be seen in 4.1b.	
	Each point represents the calculated values for one surface type, the black dotted line a 1:1 relationship and the green dotted indicates the threshold for the references values $\pm 5\%$	47
4.13	Side by side of results from this experiment (upper), and Zeng et al. (2016) [61] (lower). Zeng et al. (2016) performed direct validation of CWI method using imagery from the ETM+ sensor as a reference, while this experiment used NDVI values modelled by PRO-SAIL as a reference.	
	The sample used by Zeng et al. (2016). to calculate the estimates contained an average of 16 observations, with 6 being suspected contaminated outliers. In the results of this experiment, for site Harvard Forest the simulated sample contained 10 observations, 3 of which are contaminated in this particular scenario.	48
4.14	Intercomparison of the red and NIR spectral response functions (SRF) of the MODIS, AVHRR and VIRR sensors. X-axis is the wavelength in nanometers, y-axis is the responsivity	49
A.1	Pair plot of the sampling of the surface parameter space. Along the diagonal axis are the uni-variate distributions (i.e. histograms) of individual variables, and along the horizontal and vertical axes are the joint distribution density functions (JDDFs) per variable pair.	60
A.2	'Trimmed' pair plot of the sampling of the surface parameter space. Unrealistics pairings of variables were removed according to the methodology section 3.3.1	61
B.1	Variance of the possible RLM model parameter estimates for each surface, for a subset of 1000 randomly selected surfaces. Red band, study site Harvard Forest	62
C.1	Scatter plot of estimated NDVI compared to reference NDVI value from PROSAIL, for site Harvard Forest. Shown here are NDVI values calculated using BRDF parameters estimated from noise-free samples using OLS, Li-Gao, and CWI methods. Dotted line is 1:1 line, green lines are $\pm 5\%$.	63

xii List of Figures

C.2	Scatter plot of estimated NDVI compared to reference NDVI value from PROSAIL, for site Harvard Forest. Shown here are NDVI values calculated using BRDF parameters estimated from noise-free samples using OLS, Li-Gao, and CWI methods. Dotted line is 1:1 line, green lines are $\pm 5\%$.	64
D.1	Distribution of estimated red band BRDF parameters, for site Harvard Forest. Left-most histogram is the baseline distribution of parameters from the noise-free sample, and the remaining histograms are estimates for the scenario of ($\alpha=2$, $f_c=1.5\%$), with a total sample size of 10 observations. Angular spread of the 10 observations used for the BRDF fitting can be seen in 4.1b	65
E.1	Estimated nadir-normalised NDVI versus reference PROSAIL values for study site Harvard Forget for our terret view geometry one fig. 4.1b.	60
E.2	vard Forest, for sun-target-view geometry see fig.4.1b	68
	for sun-target-view geometry see fig.4.1c	69
E.3	Estimated nadir-normalised NDVI versus reference PROSAIL values for study site Chang Baishan, for sun-target-view geometry see fig.4.1a	70
F.1	Estimated nadir-normalised NDVI versus reference PROSAIL values for study site Harvard Forest, for sun-target-view geometry see fig.4.1b	73
F.2	Estimated nadir-normalised NDVI versus reference PROSAIL values for study site Mongu,	
F.3	for sun-target-view geometry see fig.4.1c	74
1.5	Baishan, for sun-target-view geometry see fig.4.1a	75
G.1	Estimated nadir-normalised NDVI versus reference PROSAIL values for study site Harvard Forest, for sun-target-view geometry see fig.4.1b	78
G.2	Estimated nadir-normalised NDVI versus reference PROSAIL values for study site Mongu,	70
	for sun-target-view geometry see fig.4.1c	79
G.3	Estimated nadir-normalised NDVI versus reference PROSAIL values for study site Chang	0.0
	Baishan, for sun-target-view geometry see fig.4.1a	80

List of Tables

2.1	Input leaf biophysical parameters for the PROSPECT-5 model, with associated descriptions and units	20 20
3.1	Input biophysical parameters of PROSPECT-5 model, with associated descriptions and units	26
3.2 3.3 3.4	Name and location of EOS validation sites used as study sites for accuracy evaluation. Summary of sub-datasets used from MODIS and MERSI sensors	27 28
3.5	1st 2015	29 31
4.1	Mean error for each scenario, quantified by the RMSE using PROSAIL as a reference value. Summarized here for α from 1 to 5 for the case of low cloud contamination $f_c=0.5\%$, which results in a mean relative NDVI noise of 15.5% in the contaminated observations. Greener boxes indicate lower RMSE value, and red indicates higher. Note: all tables are standardised to the same scale of RMSE-colour.	44
4.2	Mean error for each scenario, quantified by the RMSE using PROSAIL as a reference value. Summarized here for α from 1 to 5 for the case of low cloud contamination $f_c=3.0\%$, which results in a mean relative NDVI noise of 53.2% in the contaminated observations. The simulated samples have size 8 (Chang Baishan), 10 (Harvard Forest) and 13 (Mongu). Greener boxes indicate lower RMSE value, and red indicates higher. Note: all tables are standardised to the same scale of RMSE-color	44
H.1	Mean error for each scenario, quantified by the RMSE using PROSAIL as a reference value. Summarized here for α from 1 to 5 for the case of low cloud contamination $f_c=0.5\%$, which results in a mean relative NDVI noise of 15.5% in the contaminated observations. Greener boxes indicate lower RMSE value, and red indicates higher. Note:	
H.2	all tables are standardised to the same scale of RMSE-color	81
H.3	value. Summarized here for α from 1 to 5 for the case of low cloud contamination $f_c=3.0\%$, which results in a mean relative NDVI noise of 53.2% in the contaminated observations. Greener boxes indicate lower RMSE value, and red indicates higher. Note:	82
	all tables are standardised to the same scale of RMSE-color	82

Nomenclature

BRDF Bi-directional Reflectance Distribution Function

HDF Hierarchical Data Format

MVC Maximum Value Composite

NBAR Nadir BRDF-Adjusted Reflectance

NIR Near-infrared

RMSE Root-Mean-Square Error

TOA Top of Atmosphere

CWI Changing-Weight Iterative

ETM+ Enhanced Thematic Mapper Plus

MERSI Medium Resolution Spectral Imager

MODIS MODerate Resolution Imaging Spectroradiometer

MuSyQ Multi-source Data Synergized Quantitative Remote Sensing Production System

OLS Ordinary Least Squares

PROSAIL Coupled PROSPECT and SAIL models

RLM Ross-Li-Maignan parametric BRDF model

SLC Soil-leaf-canopy model

 ϕ_r Relative azimuth angle (RAA)

 ϕ_S Solar azimuth angle (SAA)

 ϕ_V Viewing azimuth angle (VAA)

 θ_S Solar zenith angle (SZA)

 θ_V Viewing zenith angle (VZA)

 λ Wavelength

 ρ Observed reflectance

 ρ_e Estimated reflectance

 $(f_{iso}, f_{vol}, f_{geo})_e$ Estimated kernel coefficients/BRDF parameters

 f_{geo} Coefficient of geometric scattering kernel

xvi

f_{iso}	Coefficient of isometric scattering kernel
f_{vol}	Coefficient of volumetric scattering kernel
α	Number of noisy/contaminated observations in sample
f_c	Fractional cloud cover/degree of contamination

1

Introduction

The Earth's surface is constantly changing; these are changes seen both seasonally due to our orbit around the sun, and long-term inter-annual changes due to anthropogenic climate forcing. Understanding these dynamic changes necessitates regular and repeated measurements, with an understanding of the associated uncertainties. The development and use of methods for monitoring the Earth's surface was therefore deemed of critical importance by the International Panel on Climate Change (IPCC) [2].

The field of satellite-based remote sensing has grown tremendously to support the geosciences, offering cost-efficiency with respect to the amount of data collected, global coverage, and long-term consistency. Quantitative remote sensing in geoscience is engaged with estimating surface and atmospheric variables through the measurement of propagated electromagnetic signals - in effect, retrieving information from a surface at a distance, without physical interaction. From this data stems a wide range of applications, from surface temperature monitoring, crop yield modelling, and vegetation and land cover changes.

Spectral vegetation index data have been used to study, among other things, vegetation activity and health, with one of the conventionally used and robust indicators being the Normalised Difference Vegetation Index (NDVI) [48]. As a spectral index, NDVI is physically based on how a surface's reflectance varies within the electromagnetic spectrum. A contrast between the reflectance in the red and NIR bands has been observed for surfaces covered with healthy vegetation, with a high level of absorption in the red band, at wavelengths of 400-700nm, and a high level of scattering in the near-infrared (NIR) band, at wavelengths of 750-1400nm [26] [52].

This contrast is therefore a useful land surface variable, that can be remotely observed and quantified using sensors aboard satellites orbiting the Earth. Mathematically, it is defined as the ratio of the difference between the reflectance in the red and NIR bands, ρ_{red} and ρ_{NIR} , over the sum of the two band reflectances: [52] $NDVI = \frac{\rho_{NIR} - \rho_{red}}{\rho_{NIR} + \rho_{red}}$. A higher, positive NDVI value generally indicates more 'greenness' [48]. It is crucial to achieve the highest possible accuracy for NDVI time-series, to bring the field of geoscience closer to reliably and consistently map and understand the Earth's surface and its processes.

NDVI retrieval and its challenges

Measuring surface reflectance, and subsequently calculating NDVI, comes with its challenges and practical considerations. The recorded surface reflectance value is a function of multiple factors, which can be broadly classified into the surface's scattering properties, which is the signal of interest, and everything else, which is noise.

Perhaps the most prevalent source of noise is the Earth's atmosphere. Due to the presence of clouds in a sensor's line-of-sight, it may record a combination of both the surface and the cloud's reflectance, or only the top of cloud reflectance. Approximately 55% of the Earth's surface is covered in clouds on average [24] - and there is an enormous variability in types and thickness, leading to many different possible cloud cover scenarios. In general, however, all clouds have a NDVI value close to 0 or negative, because they reflect nearly equally in the red and NIR band [33]. The impact of this is

2 1. Introduction

two-fold: firstly, surface reflectance retrievals often fail or are heavily contaminated (noisy) due to cloud cover; and secondly, it's not always possible to discriminate contaminated and clear-sky retrievals, especially for thin cirrus clouds [54].

Cloud-contamination, its detection, and the minimisation of its impact is a longstanding obstacle in earth observation. As a consequence it is nearly impossible to achieve daily retrievals of clear-sky surface reflectance, and noise in a mixed-pixel retrieval ¹ can severely impact the accuracy of a retrieval.

Furthermore, the variable of interest, surface reflectance, is inherently anisotropic - it varies both with viewing direction and illumination direction. The scattering properties of a vegetated surface is the net result of the leaves, stems, and other plant material transmitting, absorbing, and reflecting incoming solar radiation to varying degrees, with an element of interaction between the objects as well [50]. For a soil-vegetation mixture, the apparent fraction of background soil and vegetation differs depending on the observation angle, further adding to the surface reflectance anisotropy [34]. Each surface type has a different directionality effect as described by its Bidirectional Reflectance Function (BRDF).

Due to the BRDF, observing a surface with different sun-target-view geometry results in different measured reflectance values. A surface may be observed several times in a short timeframe and yield different values for each retrieval as a result of this, cloud-cover aside. It is considered to be an inherent property of a surface [32], and an essential consideration in remote sensing if creating a time-series of NDVI data for geoscientific purposes.

These are thus some of the major challenges to creating a continuous and accurate dataset: failed surface reflectance retrievals due to clouds, undetected cloud-contamination introducing noise into retrievals, and the anisotropic scattering properties of surface, also known as the BRDF.

NDVI compositing

An option for working around failed or heavily contaminated retrievals in a time series is to use gap-filling techniques. The NDVI value on cloudy days is estimated by making a projection based on clear-sky retrievals adjacent in time, known as gap-filling, in order to create (daily) time-series from a discontinuous dataset. However, these are prone to being inaccurate when the gaps between usable data points are large, and when cloud masks fail to detect noisy observations [55]. Another option is to assume that the surface remained unchanged over a period of several days, and combine the observations from different moments in time into a single so-called composite value. One compositing technique is the Maximum-Value Composite (MVC), which for each pixel selects the maximum NDVI value observed during a period of time. As clouds generally have a lower NDVI than clear-sky retrievals, this method avoids cloud-contaminated observations [49]. However, it doesn't consider the surface's anisotropy, and simply selecting the highest NDVI value would mis-represent the observations.

A better approach to extract meaningful information on a surface's scattering properties is to estimate the surface's Bidirectional Reflectance Distribution Function. As a physical concept, the BRDF can never be directly measured, but a surface's anisotropy can be approximated using parametric BRDF models [45]. Parametric BRDF models are typically kernel-driven: meaning that multiple functions (kernels) that describe different scattering modes are superposed, each one's contribution weighted with a coefficient [31] [11]. Within a set of multiple observations, each one taken at different sun-target-view geometries, the reflectance anisotropy behaviour is observed - the set of observations therefore forms a finite sample of the surface's BRDF. The process of estimating a surface's BRDF from a sample is known as BRDF reconstruction, and a part of this process is to reduce the impact of noisy observations.

Reconstruction of a BRDF using a kernel-driven model is performed by inverting said model to find the coefficients, or model parameters, that result in the best description of the sample. Fitting is done separately for both the red and NIR band, as the BRDF is spectrally dependent. When the BRDFs models have been estimated, the red and NIR band reflectance can be calculated at nadirviewing geometry - a normalised value that is called Nadir BRDF-Adjusted Reflectance (NBAR). A NDVI timeseries is more consistent and physically meaningful when directionality effect is accounted for, which is why the composite is calculated for this standardized geometry.

¹A mixed-pixel occurs when there are multiple features or surface types present in an area smaller than the spatial resolution of a sensor [33].

The Changing-Weight Iterative BRDF fitting method

This is the approach to NDVI compositing by the Changing-Weight Iterative (CWI) method [61][22], a BRDF-fitting algorithm that reduces the impact of cloud-contaminated observations. CWI iteratively fits a Ross-Li-Maignan (RLM) BRDF model to a set of observations, while using *a posteriori* variance estimation to reduce the impact of inaccurate observations in the sample [61]. In this way the estimated model parameters and NDVI composite should be less sensitive to noisy observations in the sample.

CWI is at the heart of the Multi-Source Data Synergized Quantitative Remote Sensing Production System (MuSyQ) algorithm, a multi-sensoral satellite product developed by RADI's State Key Laboratory of Remote Sensing Science. It is a 1km resolution NDVI composite product with global coverage ², covering a range of ecosystems, with a composite cycle or temporal resolution of 5 days [21]. Per 5-day period, MuSyQ combines surface reflectance observations from multiple sensors: the MODerate Resolution Imaging Spectroradiometer (MODIS) sensor aboard NASA's Terra and Aqua satellites, as well as the Medium Resolution Spectral Imager (MERSI) sensor on the Chinese satellites FY-3A and FY-3B. It can make use of additional datasets as well, though not in the version that was accessed for this research project.

The benefit of a multi-sensoral approach allows for a larger sample size, and also increases the chance of retrieving clear-sky observations. MuSyQ's operational algorithm involves additional preprocessing steps to normalise these different datasets (i.e. geolocationm, sensor cross-calibration) and correct for atmospheric effects, however these are not addressed here. The focus of this thesis is the Changing-Weight Iterative method, and evaluating its performance in reducing the impact of cloud-contaminated surface reflectance observations.

Problem statement

The proposed improved method CWI requires thorough study and comparison to existing techniques. CWI was published in Zeng et al. (2016) [61], in which it was stated that: "[...] the effect of the contaminated observations is suppressed in the BRDF retrieval by the CWI approach, and the inversion results are less affected by the un-detected clouds or high aerosols". However, the primary method of evaluation was comparing the CWI estimate to near-nadir reflectance images from the Landsat 7 satellite mission, as well as to similar composite products from the MODIS sensors. When validating with satellite imagery there is limited insight into the ground truth and the actual noise conditions, leaving some uncertainty as to the actual performance of the BRDF fitting algorithm.

The objective of this thesis is to use a numerical experiment to confirm that the CWI BRDF estimation method is more effective at suppressing the impact of cloud-contaminated observations than conventional methods. These are namely Ordinary Least Squares (OLS) model inversion, and the Li-Gao method [11]. OLS assumes the observations have Gaussian, zero-mean noise, while Li-Gao accounts for the fact that the noise is actually negatively-biased in the NDVI [11] by using a NDVI-based indicator to assign weights to each observation. CWI improves on both of these by combining the Li-Gao method and a novel a posteriori variance estimation approach to quantify the noise in each observation, and reduce the weight of inaccurate observations.

Scope and approach

The accuracy of a BRDF reconstruction is influenced by other factors than noise, such as the number of observations, their angular distribution, or the choice of parametric model used to describe the BRDF. Due to time constraints, this experiment therefore primarily addresses the effect that noise from cloud contamination has on the accuracy of the BRDF reconstruction, and how this compares to the OLS and Li-Gao fitting methods.

For this, it was decided to design a numerical experiment: it allows us to synthesize pseudoobservations for any surface type, and we can pre-define which observations in the sample are contaminated and by how much. Furthermore, to be able to compare the accuracy of the method, there should be a reference value. In a numerical experiment, this 'true' value is known and can be used for validation purposes.

The approach of this thesis centers on the use of an advanced radiative transfer model to simulate pseudo-observations. Using the leaf optical properties model PROSPECT [15] and canopy bidirectional

²The cover page of this report is a map of this NDVI composite over South-East Asia.

4 1. Introduction

reflectance model SAIL [50] (together, PROSAIL), a single pixel of a mixed vegetation-soil surface can be simulated. The bidirectional reflectance factor (BRF) of this physical model is then evaluated at multiple sun-target-view geometries, creating a sample of the surface's BRDF. Synthetic noise can selectively be added to observations in the sample to create a contamination scenario. Then, the three different methods are used to fit a Ross-Li-Maignan model to the observations and the results are compared to reference values.

In order to be a globally representative analysis, the numerical experiment must be repeated many times. The explained approach applied for the entire parameter space of PROSAIL, covering every possible type of vegetated surface and background soil brightness. Additionally, cloud contamination scenarios of low, medium and high cloud mixing are considered, with the number of noisy pseudo-observations in the sample being varied between 1 and 5. In this way we can thoroughly compare the accuracy of CWI to existing methods for a globally-representative set of surface types, each with their respective BRDFs, for variable noise conditions.

Key research questions

This numerical experiment encompasses various cloud contamination scenarios, a globally representative set of surface types and their respective BRDFs, and realistic angular sampling conditions. With the large amount of data gathered, this thesis aims to answer the following research questions about the performance of the novel CWI BRDF-fitting and compositing algorithm at the heart of MuSyQ:

- Can the Ross-Li-Maignan parametric BRDF model be an accurate representation of the surface BRDF?
- 2. How accurate is the nadir-normalised NDVI value, calculated using the fitted RLM model, for the noise-free scenario?
- 3. How accurate is the CWI BRDF fitting method, as compared to the OLS and Li-Gao methods. at reconstructing the BRDF model from a sample containing cloud-contaminated observations?

Report structure

In order to document the approach taken to answer the above research questions, this thesis adopts a conventional report structure as follows: firstly, in chapter 2 'Theory' the relevant principles on the topic of surface reflectance retrieval and NDVI compositing are reviewed. With an understanding of the underlying concepts, the methodology of the numerical experiment is presented in chapter 3 'Methodology'. Following this, in chapter 4 'Results and Discussion' the findings from the large amount of data simulated are analysed, and discussed, and related to existing literature. Finally in chapter 5 'Conclusion and Recommendations' the research questions are answered and conclusions are drawn on the outcome of the study. Some recommendations for further research are also given at the end of this thesis.

Theory: NDVI Retrieval and Surface BRDF Estimation

The principle of remote sensing is to observe and record information about a target using propagated signals and without physically interacting with it. Broadly speaking, there are two types of remote sensing: active remote sensing and passive remote sensing.

Active sensors emit an electromagnetic signal at the target, and measure the resulting back-scattered and/or reflected radiation. Passive sensors detect radiation that is naturally backscattered and/or reflected by a target, without adding energy to the system. As an object backscatters incoming radiation, the reflected signal's spectral characteristics contain valuable information on the object [59]. The NASA EarthData website [1] provides a comprehensive overview of the different types of remote sensors.

Remote sensing is therefore a powerful tool that has been used to observe targets on different scales: at different spatial, temporal, and spectral resolutions, and in different ranges of the electromagnetic spectrum. Of particular interest for this thesis is satellite-based sensors with the purpose of monitoring vegetated terrestrial surfaces, such as MODIS¹ and MERSI².

The observations of these two sensors are used together in the MuSyQ algorithm developed by the State Key Laboratory of Remote Sensing Science's³. This algorithm was designed to create a NDVI composite from a multi-sensoral dataset of surface reflectance measurements, while most composites rely on data from a single sensor. At its heart the CWI BRDF-fitting method [61], a novel method which has not yet been studied extensively, and the main focus of this thesis.

This chapter covers the underlying theory necessary to understand the concepts of surface reflectance, NDVI compositing, the BRDF, and the CWI method. The aim is to first inform the reader on the concepts of surface reflectance retrieval and the estimation of the BRDF with parametric BRDF models. Then, the concept of NDVI and challenges to retrieving it are presented. Following this the MuSyQ algorithm is outlined, with a focus on the CWI method which it employs. This method is explained in detail, along with more conventional BRDF fitting methods. Finally, the theory behind the radiative transfer model PROSAIL is reported - this model is used to simulate pseudo-observations which are ultimately used to assess the accuracy of the CWI BRDF-fitting method.

2.1. Surface reflectance anisotropy

A surface is described as being a Lambertian scatterer when its reflectance factor is independent of illumination and viewing geometry. This means that it is perfectly isotropic, as illustrated in figure 2.1a, and reflects equally in all directions. However, terrestrial surfaces are virtually never Lambertian scatterers, and typically exhibit anisotropic reflectance as illustrated in figure 2.1b.

The bidirectional reflectance factor (BRF) is defined as the ratio of the reflected flux from a surface in a particular viewing direction, to the reflected flux by an ideal Lambertian surface for the same illumi-

¹ More information on the MODIS sensor can be found on https://modis.gsfc.nasa.gov/

²More information on the MERSI sensor can be found on http://www.nsmc.org.cn/en/NSMC/Channels/FY 3A.html

³Part of the Chinese Academy of Science's Remote Sensing and Digital Earth Institute. For more information the reader is referred to http://english.radi.cas.cn/

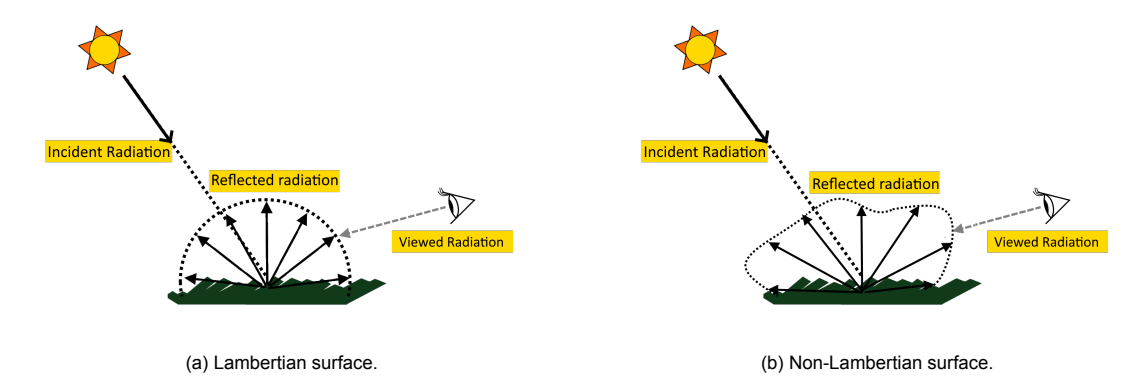


Figure 2.1: Scattered radiation by a perfectly Lambertian surface and a non-Lambertian surface.

nation and viewing angles [32]. From its definition we see that the BRF is not a fixed value, but varies for each combination of illumination and viewing angles - this is called anisotropic behaviour. As a ratio it is unitless, and is a measure of the anisotropy feature of a surface's reflectance [45]. In figure 2.3, the directionality of surface reflectance is clearly visible as the viewing zenith angle is varied.

This surface scattering behaviour is specified for any given illumination direction and scattering direction by its Bidirectional Reflectance Distribution Function (BRDF) [32]. Each wavelength, or band of wavelengths, has its own BRDF - light interacts differently with a target depending on its wavelength.

The concept of a BRDF was first defined in 1977, by Nicodemus et al. (1997) [37], and is mathematically described by equation 2.1.

$$f_r(\theta_i, \phi_i; \theta_v, \phi_v; \lambda) = \frac{dL_r(\theta_i, \phi_i; \theta_v, \phi_v; \lambda)}{dE_i(\theta_i, \phi_i; \lambda)}$$
(2.1)

Where dE_i is the irradiance from a particular illumination direction described by the zenith and azimuth angles θ_i , ϕ_i , and dL_r is the radiance reflected into differential solid angle θ_v , ϕ_v . λ is the wavelength or band of wavelengths which the BRDF describes, as it is a spectrally dependent function.

This angular convention is illustrated in figure 2.2. As phrased by Schaepman-Strub et al. (2006) [41], it "describes the scattering of a parallel beam of incident light from one direction in the hemisphere into another direction in the hemisphere".

The incident irradiance dE_i and the reflected radiance dL_r are defined for infinitesimally small solid angles, so it is in principle impossible to directly measure the BRDF. However, BRF measurements are a result of the surface's anisotropic reflectance, and therefore contain its characteristics. This information can be used to estimate the BRDF, as will be explained further in section 2.3.1.

Furthermore, the BRDF of a surface is linked to its physical and chemical properties. It is the net result of the transmission, absorption, and scattering of the objects within a pixel of surface, and the resulting interactions in between them. As a result, each surface exhibits a different anisotropical behaviour - and hence the challenge for NDVI retrieval.

2.1.1. Atmospheric effects

The atmosphere, the medium for electromagnetic radiation as it is measured from space, is not a perfect transmitter. The measured radiance at the satellite sensor is therefore different to the surface-leaving radiation. It is called top of atmosphere (TOA) radiance, and the atmospheric effects are compensated for with what is known as atmospheric correction.

Gases such as water vapor, CO_2 and aerosols in the atmosphere absorb, emit, and scatter radiation in varying degrees across the electromagnetic spectrum. The measurement recorded by a sensor is the sum of all these effects, which is simplified and shown in diagram 2.5.

Atmospheric absorption is shown in figure 2.4, for wavelengths 250-2500nm. Here we can see that specific atmospheric composition at the time of a sensor's measurement must therefore be accounted for and corrected.

There are multiple methods for peforming correction, and it is an active subject of research. An inappropriate or failed atmospheric correction can negatively impact the accuracy of surface reflectance

2.2. NDVI and clouds 7

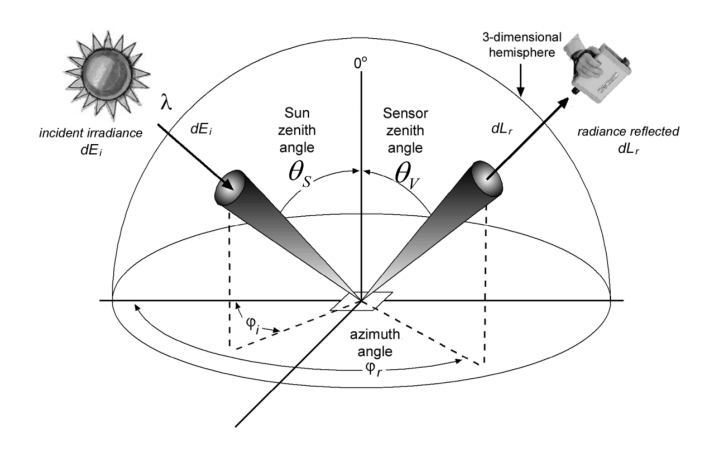


Figure 2.2: Diagram of the bidirectional reflectance factor BRF, adapted from [19].

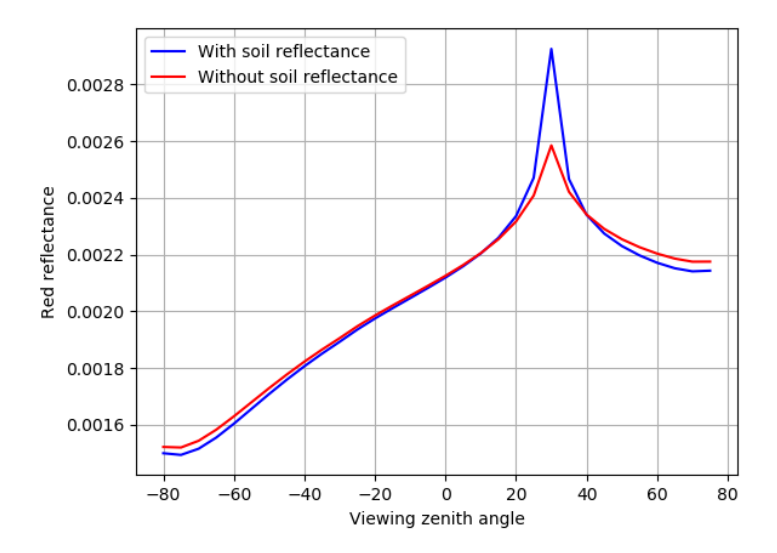


Figure 2.3: Red band reflectance of a surface covered with vegetation canopy, simulated by radiative transfer model PROSAIL. The directionality effect is clearly visible as the reflectance varies with viewing zenith angle. Including background soil in the simulation (blue line) further adds a directionality effect, as the proportion of soil reflectance in the signal varies with viewing angle.

retrieval, and is therefore an important consideration⁴.

Surface-leaving radiation is scattered by the atmosphere, leading to a diffuse component of observed radiance. So, i.e. TOA measurements cannot capture surface anisotropy completely. The CWI algorithm studied for this thesis focus on surface BRDFs and their estimation, which is a separate process to atmospheric correction. It was therefore chosen chosen to neglect the impact of imperfect atmospheric correction.

2.2. NDVI and clouds

The Normalized Difference Vegetation Index (NDVI) is a nonlinear combination of two spectral bands: the visible red band, which is in the optical region, and the near-infrared band, in the infrared region. It is based on the contrast in reflectance between these two bands, which can be used as an indicator of vegetation parameters such as biomass and plant health.

Healthy green vegetation has a relatively high absorption of solar radiation in the visible portion of

⁴See [3] [54] [52] for more information on operational atmospheric correction of TOA reflectance data. Additionally, two common algorithms used are FLAASH [8] and 6S [53].

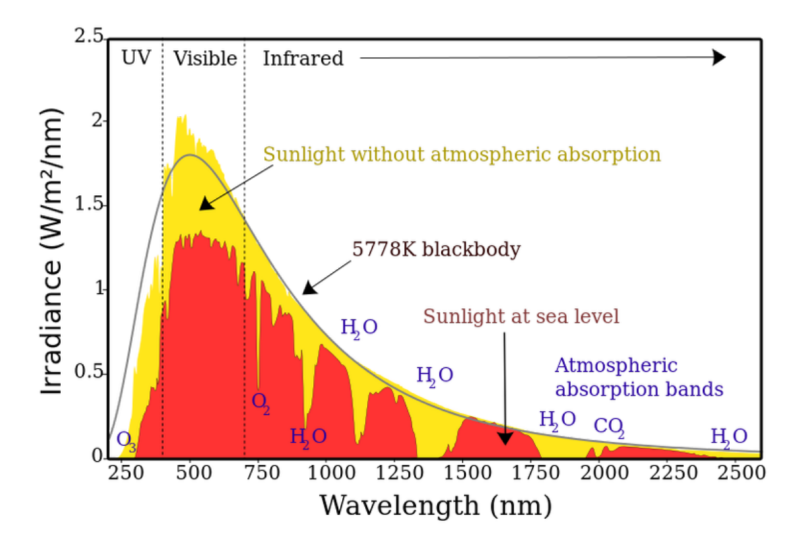


Figure 2.4: Spectrum of solar radiation for Earth. Comparison of the irradiance of sunlight as observed at the top of the atmosphere (yellow line), and at sea level (red line). Taken from [7].

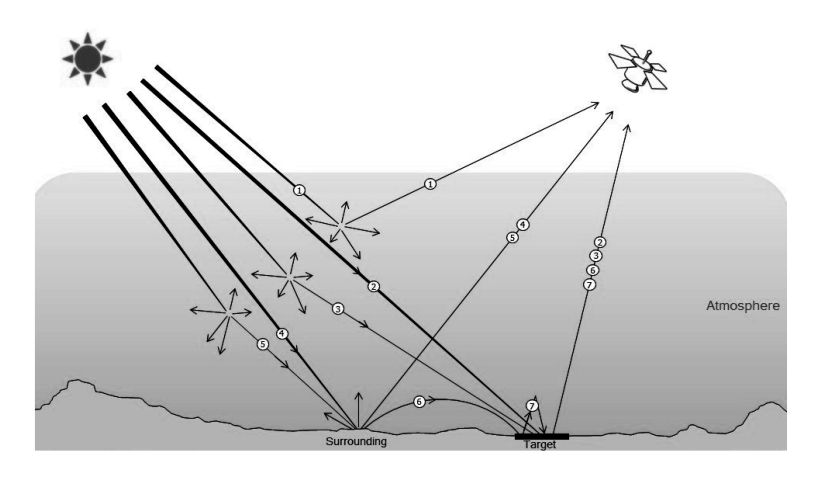


Figure 2.5: Atmospheric effect and TOA reflectance illustrated. Figure taken from [36].

the electromagnetic spectrum with wavelengths of 400-700nm due to the presence of chlorophyll [11]. Meanwhile, the spongy mesophyll leaf structure is a relatively strong scatterer in the Near-Infrared (NIR) band, which has wavelengths of 700-1000nm. This is illustrated in figure 2.6. The NDVI indicator was developed to exploit this contrast by making a non-linear combination of these two bands. It is defined as the ratio of the difference between the NIR and red band reflectance, over the sum of the two band reflectances [52] - in this way normalised to values between -1.0 and 1.0. It is shown in equation form in 2.2:

$$NDVI = \frac{NIR - Red}{NIR + Red} \tag{2.2}$$

2.2.1. Cloud cover and cloud masking

A challenge of NDVI retrieval is the presence of clouds. This is a widely recognized issue, as clouds are nearly completely optically opaque for wavelengths from 400 to 1300nm [42], meaning they are very strong reflectors in the visible and NIR regions. Hence why they are optically bright and have the color white. This can cause a failure of red and NIR reflectance retrievals when entirely blocking the view of a surface, as shown in figure 2.7.

Due to the high reflectivity of clouds in the visible region, if a cloud obstructs a sensor's line-ofsight then instead of only the surface reflectance being measured, the top of cloud reflectance, or a 2.2. NDVI and clouds

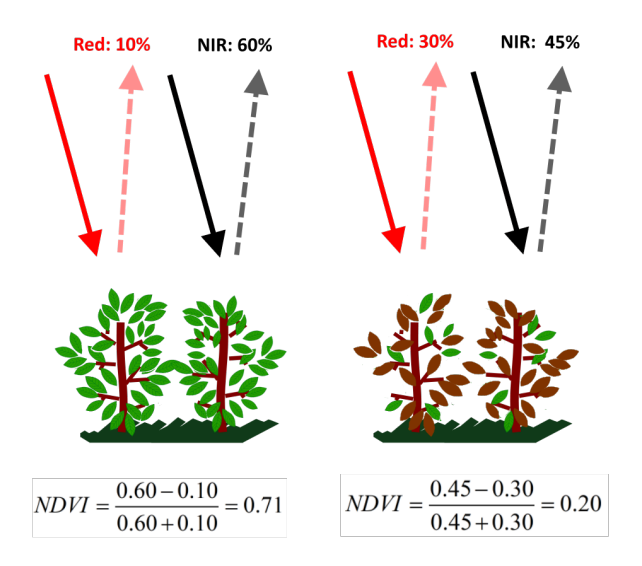


Figure 2.6: Reflectance in the red and NIR bands and corresponding NDVI value for healthy vegetation compared to stressed vegetation. The stressed vegetation exhibits a lower absorption in the red band, and higher reflectance in the NIR, resulting in a lower NDVI.

combination of both the surface and the cloud's reflectance, is retrieved. It is also possible that the surface is observed by a satellite sensor through a thin layer of high-altitude clouds.

In either case, this introduces a noise signal into the red and NIR BRF retrieval. It has been shown in literature and from past studies that the noise introduced by clouds is positively biased in the red and NIR bands, and negatively biased in NDVI [61] [12]. As stated in [12]: "Indeed, the negative bias caused by unfavourable atmospheric conditions and anisotropic bidirectional effects are a prevalent and well-recognised feature of noisy NDVI data sets."

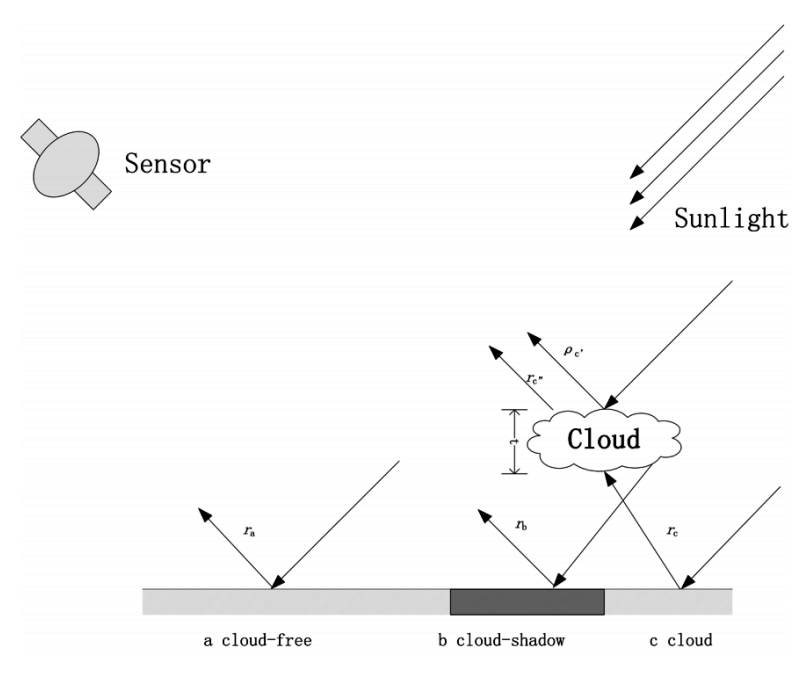


Figure 2.7: Model map of cloud-free, cloud shadow, and cloud pixels taken from [58].

Due to the presence of clouds blocking a retrieval or introducing a negatively-biased noise in the NDVI, outliers may be introduced into a dataset, as shown in figure 2.8. Sudden dips are observed in the retrieved NDVI, instead of the expected smooth seasonal change. This temporal discontinuity has

negative implications for the monitoring of both long-term as well as sudden spatiotemporal vegetation changes [48] [59].

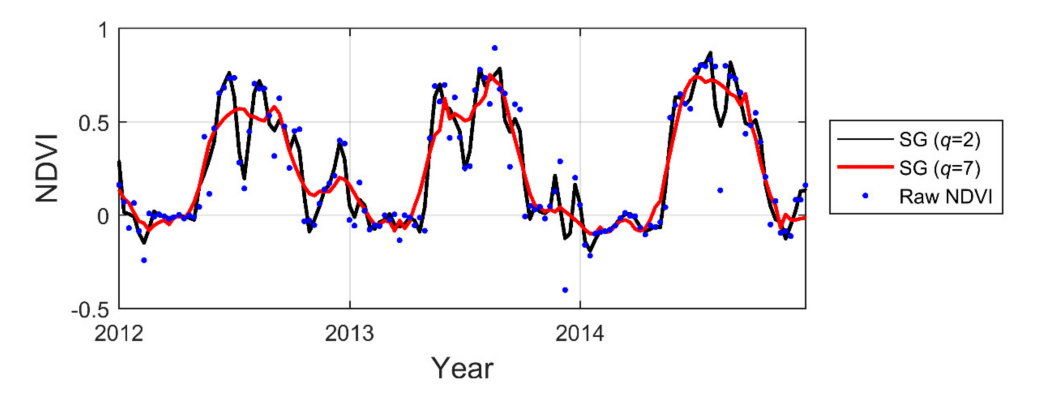


Figure 2.8: 3-year time series of MODIS sensor NDVI data, overlaid with two different smoothened trends. A seasonal variation in NDVI is observed, as is expected for most surfaces, with higher NDVI values in warm months and lower values in the colder months. Noise due to cloud-contamination and other atmospheric effects lead to lower measured NDVI values, causing temporal discontinuities that cannot be attributed to smooth seasonal changes. Taken from [6].

To prevent this, satellite data products come with associated cloud masks. The MOD35 cloud mask product of the MODIS sensor uses an advanced algorithm which takes empirical data, ancillary data and statistics to identify cloudy pixels [10]. End-users may then use this information to select cloud-free retrievals, with the possible mask values being "confident clear", "probably clear", "uncertain/probably cloudy", or "cloudy". These are based on statistical tests and thresholds used in the algorithm [10], and therefore have a degree of uncertainty.

Consequently, cloud masks such as MOD35 can fail, especially in cases of light contamination [61]. And although improvements have been suggested [56], sub-pixel clouds in particular can be left undetected in surface reflectance measurements⁵.

In summary, it is often impossible to retrieve daily cloud-free red and NIR band measurements. This is due to cloud cover either heavily contaminating or blocking observations, which cloud detection algorithms attempt to detect on a per-pixel basis. In practice, challenging scenarios arise where the algorithms fail, leading to undetected cloud contamination in a set of observations.

2.3. NDVI compositing

To work around the discontinuity in NDVI datasets due to clouds and noisy observations, methods have been developed to improve temporal coverage. These are primarily NDVI-compositing, or gap-filling. The latter estimates the NDVI value of failed or noisy retrievals by extrapolating it from adjacent periods⁶. However, due to the anisotropic reflectance of surfaces explained in section 2.1, gap-filling is susceptible to misrepresenting a surface's NDVI.

Another option is to combine observations from different moments in time to obtain a so-called composite observation. Over a period between 5 and 16 days or more, known as a composite cycle, a single NDVI value is estimated from all the measured values. In figure 2.9 we see an illustration of multiple observations of the same surface.

One class of composites is called maximum-value compositing (MVC) [49]. Since cloud contamination is negatively biased in the NDVI, an MVC simply selects the highest NDVI value from a set of observations, assuming it's the most likely one to be a clear-sky retrieval. However, this method is prone to failure if all the observations are noisy, and furthermore fails to consider the directionality effect. The MVC method may calculate a change in NDVI between composite cycles when there is no actual change in vegetation cover, but only an apparent change due to differences in sun-target-view geometry. This highlights the importance of correcting for the BRDF of surface reflectance.

⁵For further reading see [23].

⁶See [27] for further reading on gap-filling techniques.

2.4. MuSyQ 11

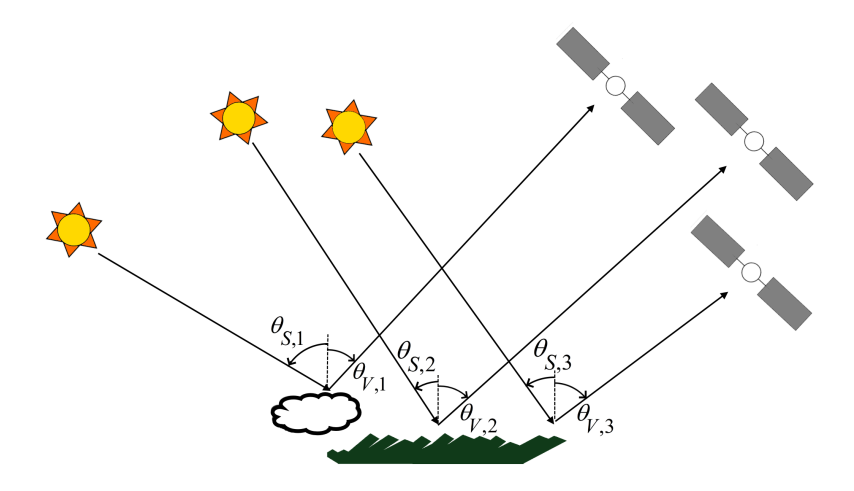


Figure 2.9: Diagram of multiple observations of the same surface, taken at different points in time, and at different sun-target-view geometries.

2.3.1. Compositing by BRDF reconstruction

The favourable method for NDVI compositing is by estimating the surface's BRDF and correcting for it. This method estimates the BRDF characteristics of a surface from the observations - which together form a sample of the surface's anisotropic behaviour - then calculate the NDVI value for a standardised geometry. Estimating a BRDF is done by first choosing a model for the surface's BRDF, and then reconstructing that model's parameters to best describe the observed surface reflectance measurements. This is explained in section 2.4.1.

By normalising the set of observations to a single sun-target-view geometry, variations in sun and view geometry between composite cycles are corrected for. A simplified diagram of normalising a set of observations to a standard geometry is seen in figure 2.10. The convention is to use a fixed-sun, nadirviewing geometry, with the illumination source and viewing angle in the same horizontal plane - i.e. at $(\theta_S, \theta_V, \phi_T) = (30^\circ, 0^\circ, 0^\circ)$. This has the benefit of allowing NDVI composite values to be comparable with each other.

During reconstruction of the BRDF, there remains a need to account for noisy observations either through pre-screening, methods to mitigate the impact of noisy observations, or both. In any case, it is beneficial to have as many observations as possible available. Together, these observations form a sample of the surface reflectance's anisotropy. A larger sample has a higher likelihood of containing clear-sky measurements, making it easier to distinguish contaminated observations, and contains more information on the anisotropical feature of the surface. However, there is a tradeoff with temporal resolution - with longer composite cycles, short-term variations in NDVI cannot be detected.

The main problem with BRDF-composites identified by MuSyQ in [21] and [22], is that the current global synthetic NDVI products have a composite cycle that is too long, with the MODIS NDVI product being 16 days. They state that the change of vegetation can not be identified accurately and effectively with these NDVI products, while acknowledging that a minimum amount of valid (i.e. clear) observations are necessary to ensure the accuracy of synthesis. This was one of the reasons that the MuSyQ algorithm, presented in section 2.4, combines retrievals from multiple sensors to increase the sample size in a shorter period of time.

2.4. MuSyQ

The MuSyQ NDVI product⁷ was developed to be an improvement over existing NDVI products by using a multi-satellite dataset to increase the number of observations per composite cycle.

In the MuSyQ algorithm, observations from the MODIS and MERSI sensors are used⁸, with a frame-

⁷Developed by the State Key Laboratory of Remote Sensing Science, Remote Sensing and Digital Earth Institute (RADI), Chinese Academy of Sciences (CAS)

⁸At the start of this thesis the algorithm was only operational for the MODIS and MERSI sensors, later AVHRR sensor measurements were also incorporated. The MuSyQ algorithm is in principle able to accommodate even more sensors still.

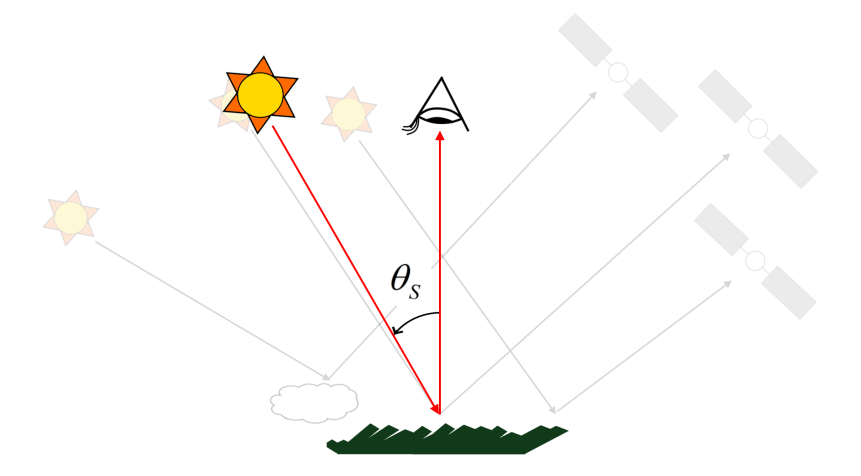


Figure 2.10: A single NDVI composite value is formed from a sample. In this case, the NDVI is standardised to a sun-target-view geometry with nadir-viewing, fixed solar zenith angle ($\theta_S = 30^{\circ}$).

work for including even more sensors. A multi-sensoral approach therefore allows for the minimum sample size to be achieved in a shorter time-frame. In figure 2.11 the number of valid observations averaged over all pixels in a test area is shown - over a 5-day period more than 70% of pixels were found to have at least 5 valid observations.

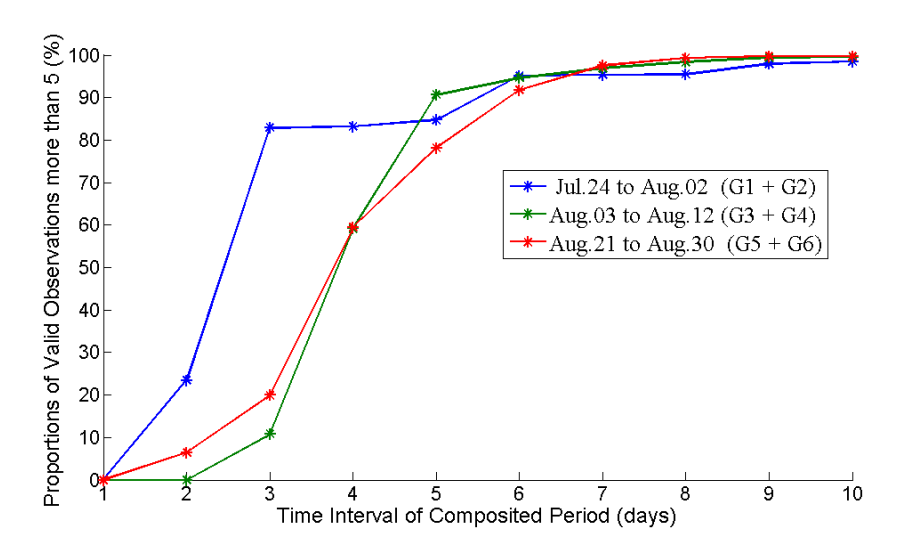


Figure 2.11: Number of valid observations available for BRDF inversion, taken from [21].

Due to the nature of using multi-sensoral data, MuSyQ's algorithm involves additional pre-processing steps, such as geolocation, pre-processing, and cross-calibrating measurements between sensors. However, these aspects are not addressed in this thesis. The focus is on a novel BRDF fitting technique at the core of MuSyQ: the Changing-Weight Iterative (CWI) method that reduces the impact of cloud-contaminated observations. This is presented in section 2.5.3. To better understand the CWI method and it's nuances, conventional BRDF fitting is firstly explained.

2.4.1. Estimating the BRDF-effect parametric models

As stated in section 2.1, the BRDF of a surface cannot be directly measured. It is possible, however, to estimate the BRDF using a model. There exists three types of BRDF models: physical, empirical, and semi-empirical. Physical models describe the physical processes that lead to a surface's anisotropy, and empirical models take a mathematical approach and characterise the BRDF using functions that describe the observed surface reflectances [28].

2.4. MuSyQ 13

Semi-empirical models describe the BRDF as a linear combination of empirical functions that approximate scattering behaviours. Weights are given to each function in the linear combination, in this way there are as many variables as there are empirical functions. These are the most commonly used in the field of remote sensing, due to their relative ease of use and practicality. The physical and empirical models require a larger amount of observations than is possible in space-based remote sensing in order to be inverted.

By inverted, what is meant is as follows: a set of bidirectional reflectance factor observations are retrieved for different viewing and illumination angles. An anisotropic feature is present in these observations due to the variation in angles, and together they form a sample of the surface's BRDF. A BRDF model is chosen that sufficiently approximates the surface's BRDF, and an attempt is made to find a solution for the model's variables which best describes the directional signature of the observed BRFs. This is known as an inverse problem.

With this method, we can get analytical inversion results using observed surface reflectance. However, for there to be at least one non-trivial solution to the BRDF inverse problem, there must be at least as many observations as there are unknown function weights. The most commonly used BRDF models are variations of the three kernel RossThick - LiSparse model, which requires a minimum of three observations to be inverted. However, as has been outlined, in practice observations have a chance of being contaminated and noisy, which can cause the BRDF inversion to fail or be highly inaccurate.

Therefore most operational BRDF inversion algorithms used in practice require a minimum of between 5 and 7 observations, and apply various methods to mitigate the impact of suspected noisy observations in the sample, while estimating the BRDF from the 'good' BRF retrievals [11]. An existing method for this is the Li-Gao approach, described in section 2.4.2, which infers that observations with a lower NDVI than the rest of the sample are noisy, and their impact should be reduced in the inversion process. This thesis focuses on an improvement on this method, the CWI method, which also estimates the variance of the observations in the sample to adjust their weight. This is explained in section 2.5.3.

2.4.2. Ross-Li-Maignan BRDF model

The BRDF model used in the MuSyQ algorithm to create a global NDVI composite product is a hotspot-corrected variation of the RossThick - LiSparse model, hereafter referred to as the Ross-Li-Maignan (RLM) model [31]. The hotspot effect is a peak in reflected radiation in the backwards direction, observable in figure 2.12, caused by the effect of shadows being reduced when viewing a canopy from the same direction as the illumination source [25] ⁹.

As a kernel-driven model, the RLM model is a linear combination of three terms, and is formulated as:

$$\rho(\theta_S, \theta_V, \phi_r, \lambda) = f_{iso}(\lambda) + f_{vol}(\lambda) K_{vol}(\theta_S, \theta_V, \phi_r) + f_{aeo}(\lambda) K_{aeo}(\theta_S, \theta_V, \phi_r)$$
(2.3)

Where θ_S is the solar/illumination zenith angle, θ_V the view zenith angle, and ϕ_r the relative azimuth angle ($\phi_{sun} - \phi_{view}$). f_{iso} , f_{vol} and f_{geo} are the weight coefficients of each of the three kernels, which empirically approximate different scattering modes. λ is the wavelength or waveband for which the BRDF is describing the anisotropical surface reflectance.

The first kernel of the Ross-Li-Maignan model describes isometric scattering: the general brightness of a surface. It is non-directional and mathematically equal to unity 1. $K_{vol}(\theta_S, \theta_V, \phi_r)$ is based on the Ross-thick function and describes volumetric scattering caused by multiple scattering of objects within a canopy (e.g. leaf surfaces) [62] [30]. The kernel $K_{geo}(\theta_S, \theta_V, \phi_r)$ is based on the Li-sparse-reciprocal function which describes geometric-optical scattering associated with the three-dimensional structure of the canopy [62] [61] [30]. Compared to the normal RossThick - LiSparse kernel, the BRDF model used by MuSyQ uses a version of the kernel K_{geo} that is modified according to Maignan et al. (2004) [31] to better account for the hotspot effect.

As we can see from the wavelength term (λ) in equation 2.3, surface BRDFs differ with wavelength due to the different scattering and absorption properties. This is the reason for the observed contrast

⁹For further reading on the hotspot effect (which is also observed outside of vegetation canopies in meteorology, astronomy, and photography, see *The Hot Spot Effect in Plant Canopy Reflectance* by A. Kuusk [25]

in red and NIR reflectance for healthy vegetation, which NDVI is based on. A BRDF can also be used to describe the scattering properties for an entired band, rather than a single wavelength. The BRDF of a surface is shown in figure 2.12 for MODIS band 3 (blue band), modelled using the conventional Ross-Li kernel model.

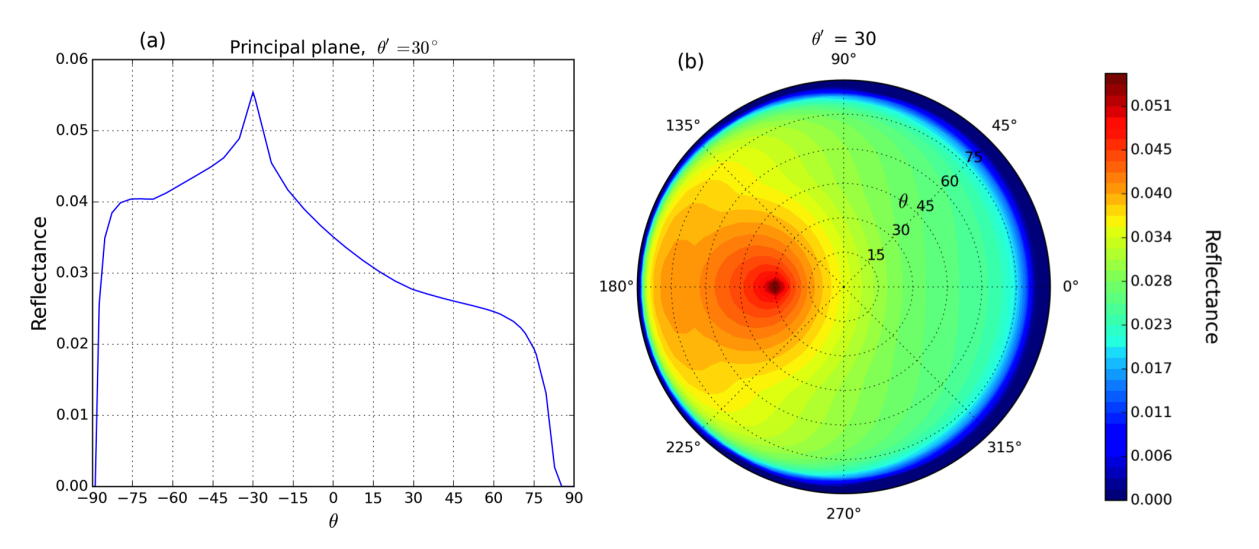


Figure 2.12: BRF anisotropy of an example surface modelled using the Ross-Li parametric BRDF model. Shown here for the wavelengths of the MODIS sensor's band 3 $\lambda = 459-479nm$. Left: Variation in reflectance along the principal plane (illumination direction and viewing direction in same vertical plane), with varying θ_V . Right: polar plot of surface reflectance for fixed illumination zenith angle $\theta_S = 30^\circ$, θ_V between 0° and 45° and ϕ_T between 0° and 360° . Taken from [28].

2.5. BRDF fitting methods

The estimation of a surface's BRDF using a kernel-driven BRDF model is done by estimating the weights of each kernel type, also known as the BRDF model parameters. The intent is to vary these such that the reflectance values computed by the estimated BRDF model match the observed values as closely as possible, when being evaluated at the same acquisition geometries $(\theta_S, \theta_V, \phi_r)$ as the observations. Hence the need to reduce the impact of noisy observations in the sample, as they can lead to BRDF model parameters that are fitted to measurements that do not accurately describe the actual surface BRDF.

For a three-kernel model such as the Ross-Li-Maignan model, three parameters must be estimated. This process is called BRDF reconstruction, or BRDF-fitting, and there exist different mathematical approaches to perform it. In this section, the OLS, Li-Gao and CWI methods that are compared to each other by this thesis will be explained.

2.5.1. Ordinary Least Squares fitting method

Model inversion for estimating the BRDF model parameters f_{iso} , f_{vol} , f_{geo} is often performed using Ordinary Least Squares (OLS). The three-parameter Ross-Li-Maignan kernel model from equation 2.3 can be written in matrix form for a single wavelength or band as:

$$M_{n\times 1} = K_{n\times 3}X_{3\times 1} + E_{n\times 1} \tag{2.4}$$

Where $M_{n\times 1}$ is the observation vector, with n BRF observations at different sun-target-view geometries. $K_{n\times 3}$ is the kernel matrix, evaluated at the n different sun-target-view geometries (as the kernels are functions of θ_S , θ_V and ϕ_r). $X_{3\times 1}$ is a matrix of the three kernel weights f_{iso} , f_{vol} , f_{geo} , and $E_{n\times 1}$ is the observation error.

For this inverse, the cost function is based on the measurement noise vector E, and in matrix form is [61]:

$$(M_{n\times 1} - K_{n\times 3}X_{3\times 1})^T \Sigma_{n\times n}^{-1} (M_{n\times 1} - K_{n\times 3}X_{3\times 1})$$
 (2.5)

The ordinary least squares solution for the kernel weights vector *X* then is calculated as:

$$X_{3\times 1} = (K_{3\times n}^T \Sigma_{n\times n}^{-1} K_{n\times 3})^{-1} (K_{n\times 3} \Sigma_{n\times n}^{-1} M_{n\times 1})$$
(2.6)

In this equation, $\Sigma_{n\times n}$ is the observation error covariance matrix. For the OLS solution, the criterion of noise being Gaussian and having zero-mean is assumed during the inversion of BRDF model parameters. This signifies an equal variance for all observations - under this assumption, the covariance matrix Σ simplifies to the identity matrix:

$$\Sigma_{OLS} = I$$

$$\Sigma_{OLS}^{-1} = I$$
(2.7)

So with independent observations, with zero-mean, and all of equal variance, the OLS solution to the BRDF model parameters simplifies to [61][20]:

$$X_{3\times 1} = (K_{3\times n}^T \Sigma_{n\times n}^{-1} K_{n\times 3})^{-1} (K_{n\times 3} \Sigma_{n\times n}^{-1} M_{n\times 1})$$
(2.8)

2.5.2. Li-Gao fitting method

The Li-Gao BRDF fitting method improves on OLS inversion by using a NDVI-based indicator to account for the asymmetric distribution of noise [61] [11]. Since the noise due to clouds and atmospheric contamination is negatively biased in the NDVI, this is accounted for by assigning lower weights to suspected cloudy observation with a weight matrix W^k . It addresses the fact that the OLS criterion is violated by the presence of clouds and aerosols, and that the noise in the measurements is not Gaussian [61].

The Li-Gao approach is iterative, where k is the iteration number. At each iteration the observations are weighted while inverting the Ross-Li-Maignan models, by setting the error covariance matrix Σ_{LiGao}^{-1} as:

$$\Sigma_{LiGao}^{-1} = W^k \tag{2.9}$$

Recall that for the OLS solution of section 2.5.1, where the criterion of independent errors with equal variance and zero-mean was assumed, Σ^{-1} was treated as an identity matrix [20] [61].

The main steps of the Li-Gao approach are as follows. For the first iteration k=0, the initial weights are set as:

$$W_{li}^{k=0}(\theta_S, \theta_V, \phi_r) = \left(\frac{NDVI_{i,obs}(\theta_S, \theta_V, \phi_r)}{NDVI_{mean}}\right)^2$$
(2.10)

Where i is the observation number, k is the iteration number, and the weight matrix is only filled along the principal diagonal at indices ii. During this first iteration of solving the inverse problem, no NDVI values have been calculated, so the surface anisotropy cannot be accounted for. From the weight matrix in 2.10 higher NDVI values are assigned a higher weight than low NDVI ones. The red and NIR BRDF models are then inverted with $(\Sigma^{-1})_{ii}^k = W_{ii}^k$, the solution for the BRDF model parameters vector being:

$$X_{red} = (K^T \Sigma^{-1} K)^{-1} (K \Sigma^{-1} M_{red})$$

$$X_{NIR} = (K^T \Sigma^{-1} K)^{-1} (K \Sigma^{-1} M_{NIR})$$
(2.11)

Then, the red and NIR BRFs are calculated using the estimated red and NIR BRDF model parameters, using equation 2.3. They are computed at the same sun-target-view geometry as each of the observations in the sample. As opposed to the initial iteration, the directionality effect is now accounted for in the weight matrix, because the calculated NDVI values are used to determine the weights of each observation:

$$W_{ii}^{k\geq 1}(\theta_S, \theta_V, \phi_r) = \left(\frac{NDVI_{i,obs}(\theta_S, \theta_V, \phi_r)}{NDVI_{i,calc}(\theta_S, \theta_V, \phi_r)}\right)^2$$
(2.12)

Where $NDVI_{i,calc}$ is the calculated NDVI using the first BRDF model solution, which has an anisotropic feature due to the Ross-Li-Maignan model. The BRDF model is once again inverted, using the new weight matrix W_{ii}^k , to find the solutions for the red and NIR BRDFS X_{red} and X_{NIR} .

This process is iterated a maximum of 5 times, or until the change in weights between subsequent iterations is less than 0.001, as determined to be sufficient by Gao et al. (2002)[11].

The iteratively calculated weights are demonstrated in 2.13. For a sample of 10 observations with one obviously contaminated observation, the heavily contaminated observation was successfully detected. The final estimated BRDF model parameters were found by Gao et al. (2002)[11] to be more accurate than the traditional OLS approach. However, one of the conclusions was that their approach works well in situations with few, heavily contaminated observations, but that the improvement over OLS is reduced in situations with light atmospheric/cloud contamination in over 60% of the sample.

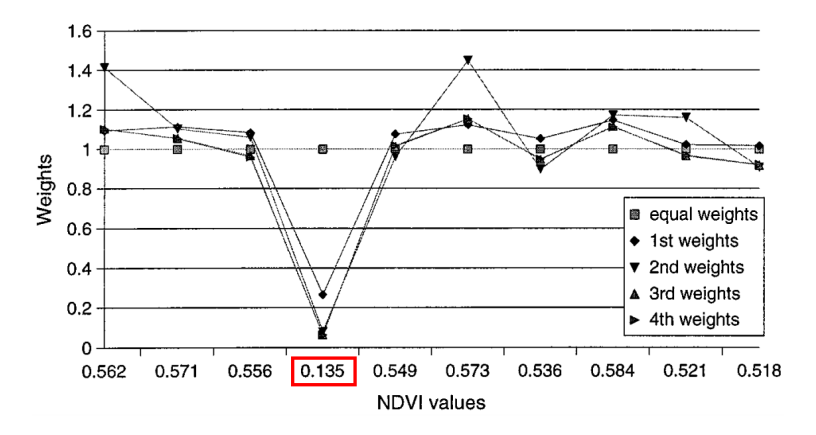


Figure 2.13: Weights assigned to each observation in a sample according to the Li-Gao BRDF fitting method. The NDVI value highlighted in red is a cloud-contaminated observation with a NDVI significantly lower than the mea NDVI value of all observations. Its weight is reduced according to equations 2.10 and 2.12. Adapted from Gao et al. (2002)[11].

2.5.3. Changing-Weight Iterative (CWI) fitting method

The Changing-Weight Iterative (CWI) BRDF-fitting method presented in Zeng et al. (2016) [61] was designed to explicitly consider both the asymmetric distribution of noise (adopted from the Li-Gao method) and also the unequal accuracy of the observations within the sample. It uses a posteriori variance estimation combined together with the NDVI indicator presented in 2.4.2 to iteratively estimate the Ross-Li-Maignan BRDF model, adjusting the weight of each observation in the sample according to its suspected noise level.

The implication of considering observation errors is that the sample contains an anisotropic feature that can be described using the Ross-Li-Maignan BRDF model. Observations that contain a large amount of noise will no longer be well-described using a surface BRDF model, and hence will have a larger observation error when the sample is fitted with such a model. Hence, CWI considers that observations have an unequal accuracy within the sample,

CWI is at the core of the MuSyQ NDVI composite algorithm and is employed to estimate the red and NIR band BRDF model parameters, and subsequently calculate the NDVI at standardised geometry. Zeng et al. (2016) [61] states that although the Li-Gao method assigns variables weights to observations based on their NDVI value, it does not quantitatively estimate the noise of each observation. As such, heavily contaminated observations can still have an impact.

The iterative procedure for CWI is similar to that of Li-Gao, and can be seen in flowchart 2.14. A key difference is that the observations are weighted by taking into account their *a posteriori* calculated variance in a weight matrix *P*.

At each iteration, CWI calculates an F-test on a statistic based on the computed variance to detect suspected heavily-contaminated observations. From this, a weight matrix P^k is calculated, with weights for each observation along its principal diagonal. P accounts for the estimated observation errors, however it does not consider the asymmetric noise distribution from clouds. Therefore, the weight matrix from the Li-Gao approach W^k is also adopted in the CWI approach, with the covariance matrix being:

$$(\Sigma_{CWI}^{-1})^k = P^k \cdot W^k \tag{2.13}$$

Where the calculation of the weight matrix *W* was explained in 2.4.2. The main steps of the CWI method to invert the Ross-Li-Maignan BRDF model are as follows, taken from [61]:

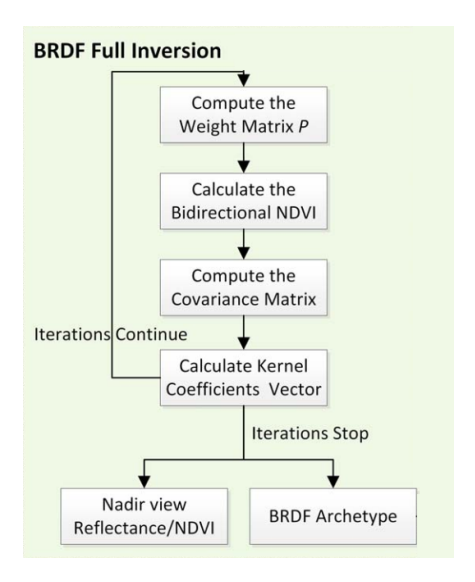


Figure 2.14: Flowchart of the Changing-Weight Iterative (CWI) BRDF fitting method . Adapted from [61].

For the initial iteration, the weight matrix P can not be calculated using a posteriori variance, because no estimate has been made yet. It is therefore set to unity, making the initial error covariance matrix for iteration k = 0:

$$(\Sigma^{-1})^{k=0} = I \cdot W^{k=0} \tag{2.14}$$

In the CWI approach, the Li-Gao weight matrix W is calculated as a first order metric, instead of a second order one. It is in principle the same, only the NDVI-based indicator is not squared, so W is written nearly identical to 2.10 as:

$$W_{ii}^{k=0}(\theta_S, \theta_V, \phi_r) = \frac{NDVI_{i,obs}(\theta_S, \theta_V, \phi_r)}{NDVI_{mean}}$$
(2.15)

The BRDF inversion is then performed with $(\Sigma^{-1})_{ii}^{k=0} = W_{ii}^{k=0}$, with the least-squares solution for the kernel coefficients vector once again being written as:

$$X_{red} = (K^T \Sigma^{-1} K)^{-1} (K \Sigma^{-1} M_{red})$$

$$X_{NIR} = (K^T \Sigma^{-1} K)^{-1} (K \Sigma^{-1} M_{NIR})$$
(2.16)

With a first estimate of the BRDF model parameters, the bidirectional reflectance of the red and NIR bands can now be calculated. The estimated bidirectional reflectances M_e are in effect calculated as $M_e = KX_e$, where X_e is the vector of estimated BRDF model parameters (in this case after the initial fitting). The error equation is then defined as:

$$V_{n\times 1} = M_{e,n\times 1} - M_{n\times 1}$$

$$V_{n\times 1} = K_{3\times n}X_{3\times 1} - M_{n\times 1}$$
(2.17)

Where V is the inverse of the measurement noise vector E from equation 2.4. This is then used to compute the *a posteriori* variance over *all* the observations in the sample, using:

$$\sigma_0^2 = \frac{V^T \Sigma^{-1} V}{r}$$

$$r = n - t$$
(2.18)

r is the degree of freedom, n is the number of observations, and t is the number of coefficients to be derived. We then also calculate the *a posteriori* variance per individual observation i. For the ith observation, its error v_i is the ith element of the error vector V, and its variance is:

$$\sigma_i^2 = \frac{v_i^2}{r_i}$$

$$r_i = R_{ii}$$
(2.19)

Here, r_i is the redundant component of the ith observation, and the ith element of the principal diagonal of reliability matrix R. The trace of R represents the redundant component of all the observations, while r_i represents the ith observation's component in the total redundant observations.

$$r = \sum_{i=1}^{n} r_i = \text{tr}(R)$$
 (2.20)

With the *a posteriori* calculated variance for all observations, and for each individual observation, a statistic T_i is calculated. CWI employs a standard F-test to identify suspected outliers among the observations, based on their calculated variance. The null hypothesis is that the ith observation is not an outlier, and the alternative hypothesis is that it is a heavily contaminated observation. So with the test statistic being defined as:

$$T_i = \frac{\sigma_i^2}{\sigma_0^2} \tag{2.21}$$

We can now compute the CWI *a posteriori* variance-based weight matrix *P*, where the weight of the *i*th observation is set as:

$$P_{ii}^{k+1} = \begin{cases} 1 & \text{if } T_i \le F_{\alpha,1,r} \\ \frac{\sigma_0^2}{\sigma_i^2} & \text{if } T_i > F_{\alpha,1,r} \end{cases}$$
 (2.22)

Where the test statistic T_i for the ith observation has an F-distribution under the null hypothesis, where α is the significance level, and r is the degree of freedom. If $T_i \leq F_{\alpha,1,r}$ holds, then the null hypothesis is valid for the ith observation, and $T_i > F_{\alpha,1,r}$, there is sufficient evidence to reject the null hypothesis, and the ith observation is a suspected outlier. A suspected outlier's weight is then set as the ratio of the variance of all observations σ_0^2 , and that observation's variance σ_i^2 .

So after the first estimate from the initial iteration k = 0, the CWI-weight matrix P^k was calculated using equation 2.22, based on the *a posteriori* variance estimation. The model is once again inverted using equation 2.16, now with both the asymmetric noise distribution as well as the unequal observation accuracies accounted for, with the error covariance matrix:

$$(\Sigma^{-1})^{k \ge 1} = P_{CWI} \cdot W_{LiGgo} \tag{2.23}$$

After the model inversion, a new estimate for the red and NIR BRDF model parameters $X_{e,red}$ and $X_{e,NIR}$ is obtained. The *a posteriori* variance of the observation errors can then again be calculated from equations 2.17, 2.18, and 2.19, with matrices W^k and P^k being newly computed from equations 2.15 and 2.22.

This process is repeated for a maximum of 10 iterations, or until the change in weights between subsequent iterations is less than 0.001 [61]. With this iterative approach to computing the covariance matrix Σ using both a posteriori variance estimation and the Li-Gao NDVI-based indicator, the CWI method adjusts the weights of each observation during the inversion of the red and NIR kernel coefficients vector. So from a set of observations taken during a composite cycle, this results in estimates X_{red_e} and X_{NIR_e} .

As was explained in section 2.3.1, the surface's red and NIR bidirectional reflectance factors can be calculated for any sun-view-target geometry using X_{red_e} and X_{NIR_e} and the Ross-Li-Maignan model. In equation form, for a a sun-target-view geometry of $(\theta_S, \theta_V, \phi_r) = (30^\circ, 0^\circ, 0^\circ)$, this is calculated for the red and NIR bands as:

2.6. Validating BRDF estimates

In section 2.4.1 the theory behind modeling a surface's BRDF using parametric kernel-driven models was explained. These semi-empirical models were shown to be invertible, doing so allows a surface's BRDF to be estimated by fitting such a BRDF model to its sample. Estimation of the BRDF parameters to get the best fit is done using the methods explained in section 2.5, which use different approaches to reduce the impact of noise in the sample.

Validating novel methods or data products presents many challenges - first and foremost is evaluating the estimated BRDF model parameters and calculated reflectance and NDVI values. Retrieving *in situ*-measurements at the same time as satellite retrievals using a spectroradiometer combined with a goniometer like in figure 2.15 is one option, and would allow for a direct comparison of the ground truth with the estimated NDVI composite. But ground validation is costly, time-consuming, and is limited to the surface types present at the site. Furthermore, there are limitations to the tools used to measure surface reflectance, as well as measurement errors, as deliberated by Aosier et al. (2007) [4].



Figure 2.15: Dual-view goniometer system used to take field BRDF measurements. Adapted from [40].

For validation purposes it is beneficial to know exactly which observations in a sample are contaminated, and to what degree. An alternative to using ground data is to use a physical model to simulate pseudo-observations. As briefly mentioned in 2.4.1, these types of models describe the physical processes that lead to a surface's anisotropy, and can be used to approximate the scattering of a surface. In the case of a vegetated surface, canopy reflectance models are used ¹⁰. The benefit of using a simulation system is that pseudo-observations can be simulated for arbitrary conditions. Therefore when testing BRDF fitting techniques, we have before-hand knowledge on the noise conditions of the sample, and can use the simulation system to calculate NDVI at normalised conditions as a reference for the NDVI composite estimated using the RLM model.

2.6.1. PROSAIL radiative transfer model

Of the existing canopy models, PROSAIL is one of the most researched and has been validated by numerous experiments [16] [17] [18], and is often considered the standard for simulating vegetation canopies.

Hence it was chosen for this thesis as the most appropriate radiative transfer model for simulating canopy reflectance. PROSAIL is a coupling of two separate models: the PROSPECT leaf optical properties model [15], and the SAIL canopy bidirectional reflectance model [50]. This combines the

¹⁰See [5] for a review of canopy reflectance models.

Symbol	Parameter	Unit
$\overline{C_{ab}}$	Chlorophyll a+b	μg/cm2
$\overline{C_w}$	Equivalent water thickness	cm
$\overline{C_m}$	Dry Matter content	μg/cm2
$\overline{C_b}$	Brown pigment content	-
$\overline{C_{car}}$	Leaf carotenoid	μg/cm2
$\overline{C_{anth}}$	Leaf anthocyanins	μg/cm2
N	Leaf structure parameter	-

Table 2.1: Input leaf biophysical parameters for the PROSPECT-5 model, with associated descriptions and units.

Symbol	Parameter	Unit
r_{soil}	Soil brightness factor	-
ρ_{soil}	Dry/wet soil ratio	-
LAI	LAI green+brown	-
ALA/LIDFa	Average leaf slope	deg
h	hotspot parameter	-
SZA	Solar zenith angle	deg
VZA	Viewing zenith angle	deg
RAA	Relative azimuth angle	deg

Table 2.2: Input canopy and background soil parameters for the SAIL model, with associated descriptions and units.

spectral variation of canopy reflectance as modelled by PROSPECT, linked to the biochemical contents of leaves, with the anisotropic feature associated with canopy architecture, modelled by SAIL.

As reviewed by Jacquemoud et al. (2009) [18], thanks to its popularity many variations and extensions of the PROSPECT and SAIL models exist. For the purpose of this thesis, the versions 'PROSPECT 5' and 'FourSAIL' were chosen, respectively. A diagram of the inputs of each half of the coupled model can be seen in figure 2.16.

Certain aspects of these models should be highlighted to understand the types of surfaces they simulate together. PROSPECT represents a leaf using a flat plate model: the leaf is simulated as a single layer or several stacked layers of flat, Lambertian scatterers [15]. The leaf's biochemical composition, as specified with the input parameters summarised in table 2.1, determine its simulated optical properties.

As leaves form the main surface of the canopy, the leaf properties from PROSPECT are the main input for SAIL to model the canopy reflectance [16]. The canopies modelled by SAIL are a semi-infinite and homogeneous cluster of leaves (same leaf type throughout), and with random leaf azimuth distribution (randomly rotated in the horizontal plane) [14]. Additionally, SAIL also accounts for the background soil's reflectance properties. In the version of PROSAIL used for this thesis, the soil's reflectance is calculated as a linear mixture of a wet and dry soil spectra, scaled by a brightness term r_{soil} . The canopy variables and sun-target-view geometry used as inputs by SAIL are summarised in table 2.2.

These two models were re-written in Python and paired together by J. Gomez-Dans ¹¹, making it relatively convenient to simulate canopy reflectance repeatedly for different surfaces. The pairing of the two allows for a broad range of surface types to be simulated, within the physical assumptions made by the PROSAIL model that were detailed above.

¹¹https://pypi.org/project/prosail/

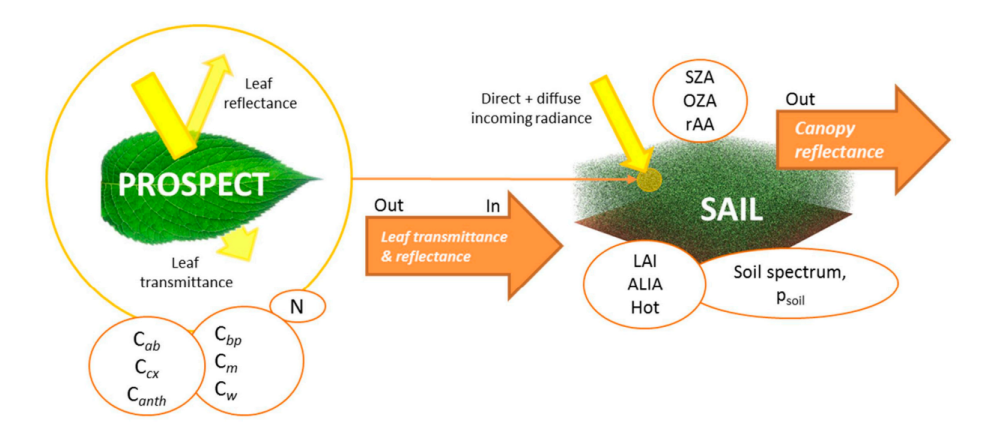


Figure 2.16: Simulating bidirectional reflectance factor for a canopy using the PROSAIL model. Leaf transmittance and scattering as modelled by PROSPECT is passed on as input to the SAIL canopy model to which it is coupled [5].

2.7. Theory - conclusion

Surface reflectance retrieval from space comes with its challenges, namely limited temporal and angular sampling, compensating for the BRDF effect, and heavily-noisy or blocked retrievals. This is the reason that different types of compositing techniques have been developed, in order to create usable time-series of data. Contaminated observations are not always straight-forward to detect and surpress, although it is certain that they are negatively-biased in NDVI for the case of sub-pixel cloud contamination. That is the case which this research focuses on, and the CWI BRDF-fitting method which intends to reconstruct the RLM BRDF model while suppressing the effect of these noisy observations. To be able to evaluate CWI's performance for a variety of surface types, PROSAIL proves to be a powerful tool that simulates surface reflectance retrievals by pairing the leaf optical properties model PROSPECT, and the canopy reflectance model SAIL.

With an understanding of the fundamental principles of remote sensing, NDVI retrieval, and the effect of clouds and atmospheric contamination, the context has been set for the research methodology.

Methodology: Numerical Experiment Using PROSAIL

MuSyQ's CWI BRDF-fitting method is evaluated by means of a numerical experiment, that simulates the surface reflectance of vegetation canopies using a radiative transfer model.

In order to be able to compare the CWI method to the more conventional OLS and Li-Gao methods, PROSAIL is used to simulate pseudo-observations of a surface's BRDF. This set of synthetic measurements forms a sample of the surface BRDF, to which the Ross-Li-Maigan model can be fitted, using three different methods to obtain estimates of the kernel coefficients. Resulting estimates are used to calculate nadir-normalised NDVI composite values - which are compared to reference values from PROSAIL. In this way, an understanding of the accuracy of the estimates can be obtained.

The simulated pseudo-observations form a sample of a given surface's BRDF, as modelled by PRO-SAIL. Different values can be set for the PROSAIL parameters to describe different surface types, and the sun-view-target geometries of the pseudo-observation can also be changed. Additionally, synthetic noise due is also added to simulate undetected cloud-contamination of the observation, varying both in amount of contaminated observations and in cloud fraction. Depending on which cloud contamination scenario is simulated, a different noisy sample is created and used by the different methods to estimate the BRDF model parameters.

A key advantage of a numerical experiment is control over the simulation conditions. Since CWI was designed and intended to be used as a global NDVI product, the experiment varies the surface types, acquisition geometry, and cloud contamination scenarios to cover a globally-representative broad range of cases.

In this chapter the design of this system, as well as the various input variables, are documented and presented to the reader. Beginning with a roadmap of the methodology, it continues with a detailed explanation of the work performed at each step. Each step is concluded with a small summary, to maintain an overview of the process.

3.1. Roadmap

The methodology of the simulation system is summarised on a conceptual level in figure 3.1. There are three groups of input variables that describe the simulation conditions: biophysical variables that describe the leaf, canopy, and background soil properties of the surface, the sun-view-target geometry of each observation, and the cloud-contamination scenario variables. How these variables are used in the simulation system is outlined as follows:

For the surface variables, nearly the entire parameter space of PROSAIL was sampled, simulating a broad range of vegetation canopies and background soils. This was done using Sobol sampling, a sampling strategy for multivariate parameter spaces that doesn't produce clusters or gaps ¹. A list of 6,000 different sets of surface variables was produced in this way, covering the entire parameter space of the PROSAIL model's input biophysical variables. This is reported in section 3.3.

¹See [46], [39] for further reading.

To link the experiment to real-life conditions, the sun-target-view geometry of actual observations is used when simulating the pseudo-observations - which is explained in section 3.4. For this, images are used from the sensors Terra and Aqua, aboard NASA's MODIS satellites, and the sensors MERSI-I and MERSI-II, aboard China's FengYun 3 satellites. For 3 globally-distributed locations, each with a different 'view' from these sensors, 3 sets of sun-target-view geometries were determined from these images. In this way the angular sampling is derived from actual operational conditions, and is used as an input for PROSAIL when simulating the pseudo-observations.

With one set of variables describing the canopy and background soil, and a set describing the geometry of the satellite measurements, pseudo-observations are simulated with PROSAIL. This step is described in section 3.5. For each surface, three noise-free sample of the surface's BRDF are created - one for each study site and its associated sun-target-view geometry.

These are then used to create noisy samples, by using a linear spectral mixing model to introduce noise due to cloud contamination - which is explained in section 3.6. Using this model, the presence of sub-pixel clouds in measurements is modelled. For each simulated surface noisy samples were created in this way for each cloud contamination scenarios. Scenarios varied by looking at cases of low, medium and high cloud fractions ($f_c = (0.01\%, 0.015\%, 0.03\%)$, respectively), and by varying the number of contaminated observations between 1 and 5 ($\alpha = (1, 2, 3, 4, 5)$).

Using the created noisy samples, the Ross-Li-Maignan model was reconstructed by estimating the kernel coefficients. This BRDF model's parameters were estimated using three different methods: ordinary least squares (OLS), Li-Gao weighted least squares, and CWI weighted least squares. Estimating the parameters with three different methods allows for the impact of the noisy observations in the sample to be compared across the methods.

3.2. Assumptions made

The above roadmap outlines the workflow of the simulation experiment. However, due to the complexity of surface reflectance simulation, the MuSyQ algorithm, and BRDF estimation, the following assumptions were made:

- The PROSAIL model simulates reflectance spectra from 400 to 2500 nm. Red and NIR band reflectances were derived from these using the spectral response of MODIS Aqua bands 1 and 2, with bandwidths of 620-670 nm and 841-876 nm, respectively. The same bandwidths and spectral response were assumed for all observations.
- Noise due to sources other than cloud contamination in the observations is not considered ².
- Undetected cloud contamination of an observation is simulated as a mixed-pixel retrieval, using a linear spectral mixing model.
- The surface types simulated are restricted to the lower and upper limits set on the PROSAIL input variables, and the number of surfaces simulated was limited to 6,000 due to computational cost³.

3.3. Creating a set of representative surfaces

One half of the parameters required for simulating a surface's reflectance with PROSAIL is the suntarget-view geometry, and the other half is the surface type. A surface type is in this case the coupling of a vegetation canopy, and background soil under the canopy.

The purpose of this step was to creat a set of surface types that covers a broad range - in this way making the experiment globally representative in terms of realistic surface types. Therefore, the set of surfaces should cover the entire parameter space of PROSAIL within defined upper and lower limits, without clusters or gaps.

The sampling of the surfaces was performed using a script provided by the authors of [34], and is based on a quasi random number generator. Sobol's sequence generator draws an initial sample from a multivariate uniform distribution, and on subsequent loops fills in unsampled gaps, maximising

²Side studies showed that sensor noise did not have a noticeable impact on the BRDF reconstruction.

³See section 3.3 for details on the sampling of PROSAIL's input parameter space.

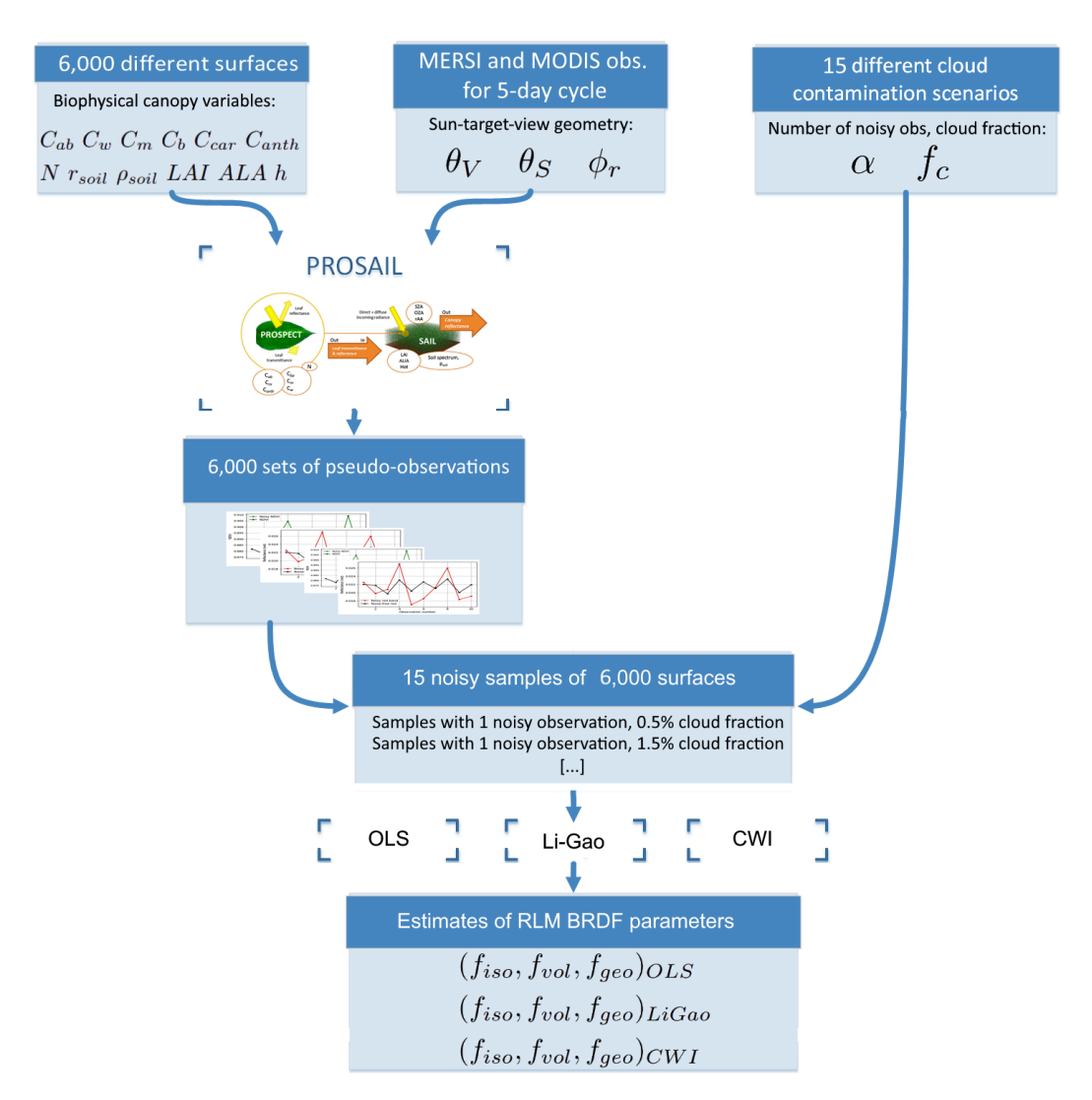


Figure 3.1: Conceptual roadmap of the numerical experiment's methodology. The three groups in the top row are the types of variables used: variables describing the canopy and background soil types (inputs for PROSPECT and SAIL), variables describing the sun-target-view observation geometry (input for SAIL) and variables describing the different cloud contamination scenarios. The pseudo-observations simulated with PROSAIL form noise-free samples of the surfaces' BRDFs, and these are combined with the reflectance of cloudy pixels using a linear spectral mixing model (not shown here, see subsection 3.6 for details on simulated noise). For each surface in total 15 noisy samples are simulated, and for each one the Ross-Li-Maignan BRDF model parameters are estimated using the OLS, Li-Gao, and CWI fitting methods.

uniformity and reducing gaps and clusters [34]. Each individual biophysical parameter was varied one at a time, creating a new sampling point each time.

PROSAIL has a large amount of input variables, with 3 acquisition geometry variables and 15 leaf and canopy variables (as explained in section 2.6.1). Therefore the total number of permutations had to be limited for the numerical experiment to be computationally feasible. Based on papers that either implemented PROSAIL or studied its sensitivity to input variables [60] [13] [34] [35], measures were taken to constrain the scope of the surface portion of the study. This was done in order to focus on the variables which had a strong influence on reflectance in the red and NIR bands, and neglect variables with little or no effect. The following assumptions were made:

- 1. Parameter values were given lower and upper limits, encompassing the surface types seen globally.
- 2. Certain biophysical parameters were kept fixed, as they have a negligible influence on the reflectance in the red and NIR regions, based on [34].

Parameter	Unit	Min	Max	Sampling
C _{ab} - Chlorophyll a+b	μg/cm2	20	80	Sobol
C _w - Equivalent water thickness	cm	0.005	0.04	Sobol
C _m - Dry Matter content	μg/cm2	0.005	0.005	Fixed
C _b - Brown pigment content	-	0.5	0.5	Fixed
C _{car} - Leaf carotenoid	μg/cm2	1	1	Fixed
Canth - Leaf anthocyanins	μg/cm2	0	0	Fixed
N - Leaf structure parameter	-	1.75	1.75	Fixed
r _{soil} - Soil brightness factor	-	0.0	1.0	Sobol
$ ho_{soil}$ - Dry/wet soil ratio	-	0.01	0.3	Sobol
LAI - LAI green+brown	-	0.5	7	Sobol
ALA/LIDFa - Average leaf slope	deg	5	85	Sobol
h - hotspot parameter	-	0.05	0.05	Fixed

Table 3.1: Input biophysical parameters of PROSPECT-5 model, with associated descriptions and units

3. Sobol sampling, a more efficient method for sampling the parameter space, was applied⁴ [46] [34].

In table 3.1 the scope of biophysical variables that were used can be found. According to Mousivand et al. 2014 [34], the parameters of greatest influence to the reflectance in the red and NIR band are C_{ab} , C_w , r_{soil} , ρ_{soil} , LAI and ALA. Remaining parameters with little to no influence on the red and NIR band reflectance were set at fixed values. This parameter space was sampled 6,000 times using Sobol sampling [46], varying individual biophysical parameters within their range, to create a set of surfaces to be synthesised with the PROSAIL model.

3.3.1. Removing unrealistic surfaces

In figure A.1 (appendix A) we see a representation of the original sampling of the parameters space. Due to the sampling being uniform across the parameter space, there are certain surfaces with a near-maximum value for one variable combined with a near-minimum value for another. For certain variable pairs, these surfaces at the edges of the parameter space have little physical meaning. For example, a high LAI value implies a relatively high amount of vegetation, which is unlikely to have a low chlorophyll content.

Surfaces with these unlikely pairings were 'trimmed' and removed from the parameter space, in order not to affect the sensitivity analysis. This was done by drawing an exponential line through the top left and bottom right corners of the joint distributions of these linked variables. The inversely related variable pairs were $LAI - C_{ab}$, $LAI - C_{w}$ and $LAI - \rho_{soil}$. In figure 3.2 we see the surfaces at the extreme ranges for the $LAI - C_{ab}$ pairing. In total 800 surfaces, approximately 15%, were removed by this method.

In summary

In summary, a realistic and computationally manageable set of surfaces uniformly covering the parameter space was created. Biophysical variables that are irrelevant to the red and NIR bands' reflectance were kept at fixed values, and the remaining variables were constrained to realistic ranges. Using Sobol sampling, the parameter space was uniformly sampled without clusters and gaps to create 6,000 combinations of PROSAIL input parameters. 800 surfaces with unrealistic combinations of variables were removed so as not to influence the sensitivity analysis. A globally representative set of combinations of biophysical parameters remained, that can individually be paired with the geometry described in step 3.4 to simulate surface reflectance retrievals.

⁴See [34] for further reading on Sobol sampling.

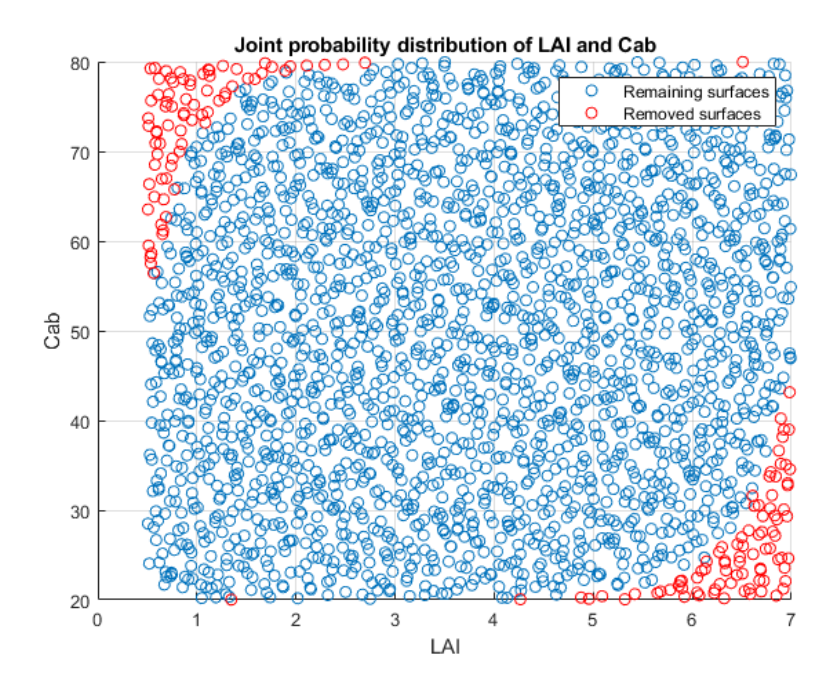


Figure 3.2: Joint distribution density function of biophysical variables LAI and C_{ab} . An exponential curve was drawn in the 'corners' of the joint distribution, selecting surfaces at the edges of the bi-variate parameter space to be removed.

3.4. Extracting actual geometry

MuSyQ's CWI algorithm is designed to be used on a multi-sensoral dataset comprising of images from the MODIS⁵ and MERSI⁶ sensors, which can potentially be expanded to include more sensors. Therefore, images from these sensors were studied for three study sites chosen for their global distribution, summarised in table 3.2. The latitude, longitude, and MODIS grid tile number for each location was found on the EOS land validation website. All MODIS and MERSI images that measured these sites in the 5-day time period from 27/6/2015 to 1/7/2015 were downloaded.

Site name	Country	Latitude (°)	Longitude (°)
Chang Baishan	Jilin, China	42.403	128.096
Mongu	Western Prov., Zambia	-15.438	23.253
Harvard forest	Massachussets, USA	42.540	-72.178

Table 3.2: Name and location of EOS validation sites used as study sites for accuracy evaluation.

For MOD09GA the scenes were downloaded using the Python package 'pyModis' ⁷, an example of which can be seen in figure 3.2. The MERSI images from the FY3A and FY3B satellite platforms were provided through direct contact with colleagues at the Chinese Academy of Sciences. A sample of one MODIS image tile can be seen in figure 3.3.

Satellite scenes are typically stored as HDF (Hierarchical Data Format) files, which is comprised of multiple sub-datasets. Each sub-dataset contains different data rasters, such as surface reflectance, quality flags, or cloud masks, for example. For this study, the information needed from the scenes are the viewing and illumination geometry, the cloud quality flag, and the red and NIR band reflectance (used for the cloud study, discussed in section 5.3.4). The bands used from the MODIS and MERSI images are summarised in table 3.3.

Using the python package 'pyHDF' for MODIS scenes and GDAL for C for the MERSI scenes, the relevant sub-datasets were extracted as rasters from the original HDF files. See table 3.3 for the satellite products and the respective sub-datasets used. With the required rasters extracted, the sub-datasets'

 $^{^{5}}MOD09A1.006$ MODIS image accessed at https://doi.org/10.5067/MODIS/MOD09A1.006

⁶MERSI images shared by colleagues at RADI.

⁷http://www.pymodis.org/

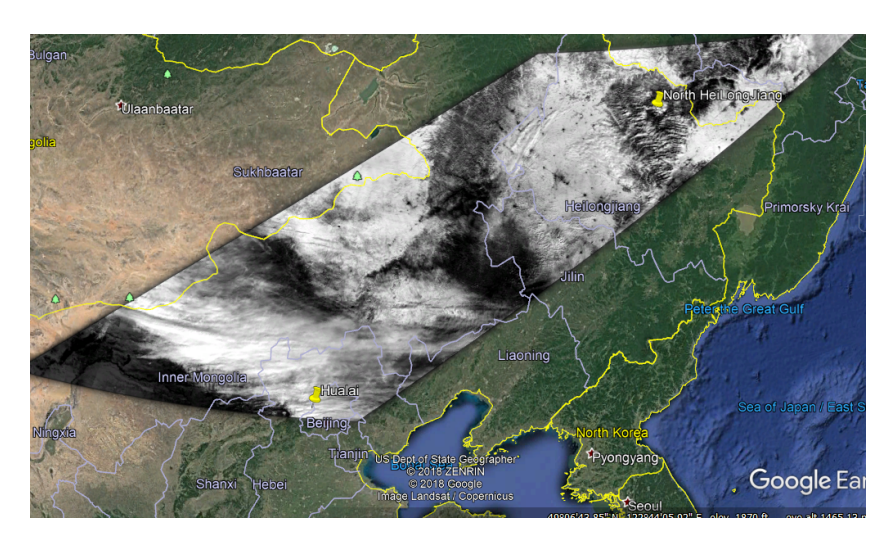


Figure 3.3: Grayscale image of band 1 of a single MODIS image tile, overlaid on a Google Earth image of northeastern China.

Product name	MxD09GA	FY3x MERSI
Resolution (m)	500	500
Sub-datasets used	'state_1km_1'	'Latitude'
	SensorZenith_1	'Longitude'
	SolarZenith_1	solar_azimuth
	SensorAzimuth_1	solar_zenith
	SolarAzimuth_1	view_azimuth
	'sur_refl_b01_1'	view_zenith
	'sur_refl_b02_1'	DataSet_CloudMask

Table 3.3: Summary of sub-datasets used from MODIS and MERSI sensors.

values at the pixel containing the study site was selected.

3.4.1. Pre-screening

The extracted bands were analysed at the pixels containing the study sites. For MODIS, the band 'state_1km_1' which describes the 'Reflectance Data State' was inspected, and for MERSI data the band 'DataSet CloudMask was used.

Each observation was inspected and tested on several criteria to determine if they would be valid retrievals. Observations were invalid when captured during nighttime, when retrieval failed, when the angle was too far off-nadir, and when clouds were detected. In effect, they were invalid if:

- 1. Cloud mask band value was '1' (MERSI) or 'Cloudy' (MODIS).
- 2. Retrieval failed due to sensor malfunction, lack of sunlight, or othe reasons..
- 3. The viewing angle was too far off-nadir (VZA < 60).

Extraction of acquisition geometry was performed for all 3 study sites. For each observation, a set of angle tuples was created, defining its viewing and illumination angle. Each set defines the nominal observations available for a composite, assuming no cloud contamination. In table 3.4 we see the angular sampling for study site Changbai, China.

In summary

To summarise: All MODIS and MERSI scenes which captured the study site(s) were collected for a 5-day period from June 27th 2015 to July 1st 2015. The pixel containing the study site was identified in each scene, and the sub-datasets were studied to see if the observation was valid for that pixel. It was considered valid when the VZA was not too high ($< 60^{\circ}$), it was taken during the day (based on SZA), was identified as cloud-free by the MODIS and MERSI cloud masks, and the sensor did not

Platform	Year and day	$\theta_V(^\circ)$	$\theta_{\mathcal{S}}(\degree)$	$\phi_V(^\circ)$	$\phi_S(\degree)$	$\phi_r(^\circ)$
MODIS Terra	2015-178	55.5	19.5	-71.6	166.4	58.0
MODIS Terra	2015-181	38.9	26.4	97.3	129.8	32.5
MODIS Aqua	2015-178	30.9	25.5	-98.1	132.1	34.0
MODIS Aqua	2015-182	10.9	22.5	79.5	-144.5	44.0
FY3B	2015-179	42.1	25.1	73.0	-133.6	26.5
FY3B	2015-181	48.6	36.2	-95.6	-110.1	14.5
FY3B	2015-178	25.2	27.2	75.9	-127.3	23.1
FY3B	2015-182	33.2	33.6	-98.3	-114.5	16.2

Table 3.4: Acquisition geometry of all valid MODIS and MERSI measurements of the study site in Changbai, China.

Observations collected over a 5-day period from June 27 2015 to July 1st 2015.

malfunction. In this way, a list with the geometry of nominally valid observations of the study site(s) was created.

3.5. Simulating pseudo-observations and determining reference BRDF model parameters

The two elements required to define and simulate a cloud-free surface reflectance retrieval were brought together – the biophysical variables required to describe the surface, and the acquisition geometry extracted from 5-days of actual MODIS and MERSI imagery. The radiative transfer model PROSAIL was chosen for this task of simulating the anisotropy of a surface's reflectance ⁸.

It was assumed that the leaf and canopy radiative transfer model PROSAIL characterises a surface's reflectance anisotropy well. This decision was based on the many existing papers [62] [5] [47] that either implemented or studied the PROSAIL model.

Firstly, the set of approx. 6,000 surface types from step 3.3 and on-average 10 valid observations over the composite period from step 3.4 were paired together. PROSAIL was used to evaluate the different surface reflectance retrievals for each given surface. This resulted in approx. 60,000 simulated retrievals, and for each simulation the output was the reflectance spectrum, an example of which is shown in figure 3.4.

To derive red and NIR band-specific reflectances from a spectrum, the response of the sensor for which the retrieval is being simulated must be taken into account. The Spectral Response Function (SRF) of a sensor describes hows a particular sensor responds to, and records, the incoming irradiance. As an example, the SRF overlaid with the input reflectance spectrum is shown in figure 3.5.

The SRF of the MODIS Aqua sensor was applied to the spectrum to derive the red and NIR band reflectances. It was assumed that MODIS Terra, FY3A MERSI and FY3B MERSI all had virtually the same SRF as MODIS Aqua. The scope of research was limited to the surface BRDF and its estimation, and the effect of differences between the sensors on was not considered.

The end result of using PROSAIL was cloud-free, synthetic surface reflectance pseudo-observations. With 10 different retrievals being simulated per surface, the set of pseudo-obsevations together formed a noise-free sample of the surface's BRDF. The surface input variables, sun-target-view geometries of the pseudo-observations, and noise-free red and NIR band reflectances were recorded to a flat-text file.

3.5.1. Baseline Ross-Li-Maignan BRDF model fitting

From this noise-free sample, the weights of each kernel in the Ross-Li-Maignan (RLM) model were estimated using Ordinary Least Squares (see explanation of methods in section 2.5). These kernel coefficients formed the best case estimate from a noisefree sample, to which the estimates from cloud-contaminated samples could be compared.

For each surface, the best-estimate RLM model parameters were denoted as $(f_{iso}, f_{vol}, f_{geo})_{ref}$, and were recorded for future reference. The BRDF model estimates resulting from noise-contaminated samples, performed later in step 3.7, could then be compared to these as reference values.

⁸The reasons for choosing PROSAIL are explained in 2.6.1

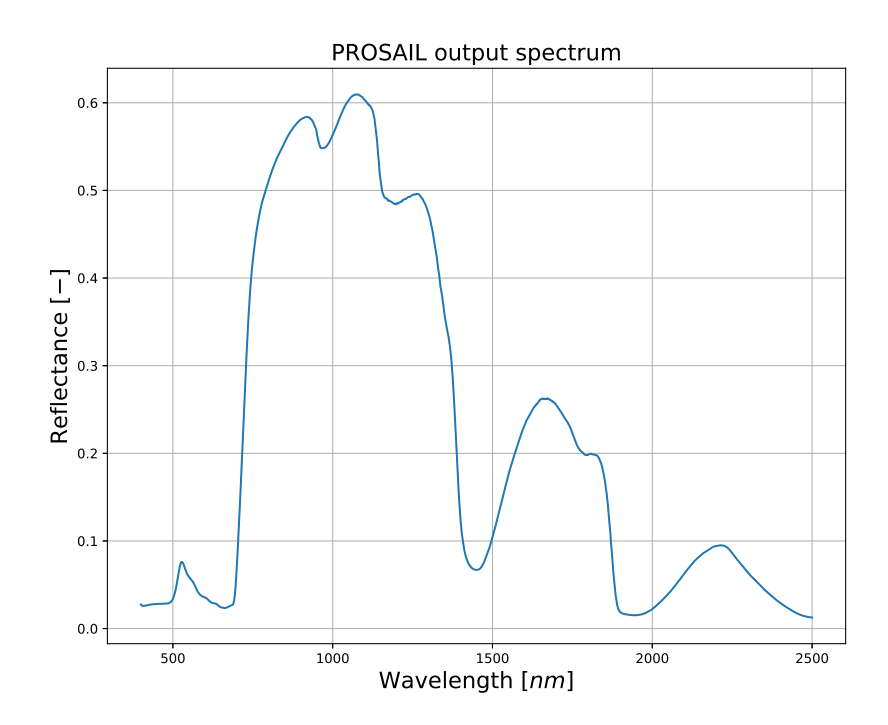


Figure 3.4: Reflectance spectrum from 400 to 2500 (nm) for a vegetated surface with NDVI = 0.9 and acquisition geometry of $(\theta_V, \theta_S, \phi_T) = (0, 30, 0)$, as simulated by PROSAIL.

In summary

For a given set of leaf and canopy parameters (i.e. a surface), and acquisition geometry, the PROSAIL model was used to simulate the entire spectrum of the surface reflectance, from 400-2500 nm. The red and NIR band reflectances were derived from these spectra, assuming all sensors had the spectral response function as the MODIS Aqua sensor.

For each surface 10 red and 10 NIR band pseudo-observations were synthesised, depending on which site was studied. This was done for 6,000 surface types, paired with on average 10 observations per surface, meaning approx. 60,000 simulations were performed per study site. The results were noise-free samples of the surface's BRDF, as modelled by PROSAIL.

A noisefree estimate of the Ross-Li-Maignan model's kernel coefficients was also calculated using ordinary least squares and recorded to be used a reference.

3.6. Cloud noise contamination scenarios / Noise contamination

Due to the large variety in cloud types, and different ways in which they can contaminate observations without being detected, a practical approach was taken to quantify the effect of clouds. Based on related literature, a linear spectral mixing model defined by 3.1 [33] [44] was used to simulate the effects of sub-pixel cloud contamination.

Sub-pixel clouds can be present in a surface reflectance retrieval, typically decreasing the NDVI of the pixel [33]. Equation 3.1 defines the reflectance of such a mixed pixel as the linearly proportional contributions of the top of cloud reflectance $\rho_{c,i}$, and the reflectance of the actual surface $\rho_{g,i}$.

$$\rho_i = f_{c,i} \cdot \rho_{c,i} + (1 - f_{c,i}) \cdot \rho_{g,i} \tag{3.1}$$

In order to quantify the top of cloud reflectance, a minor side-study was performed ⁹. Using the same sample of observations from which data was extracted in 3.4, a study was performed using MOD09GA surface reflectance scenes from EOS land validation site ChangBai. From the 10 images, the following steps were performed:

⁹put any additional details in appendix

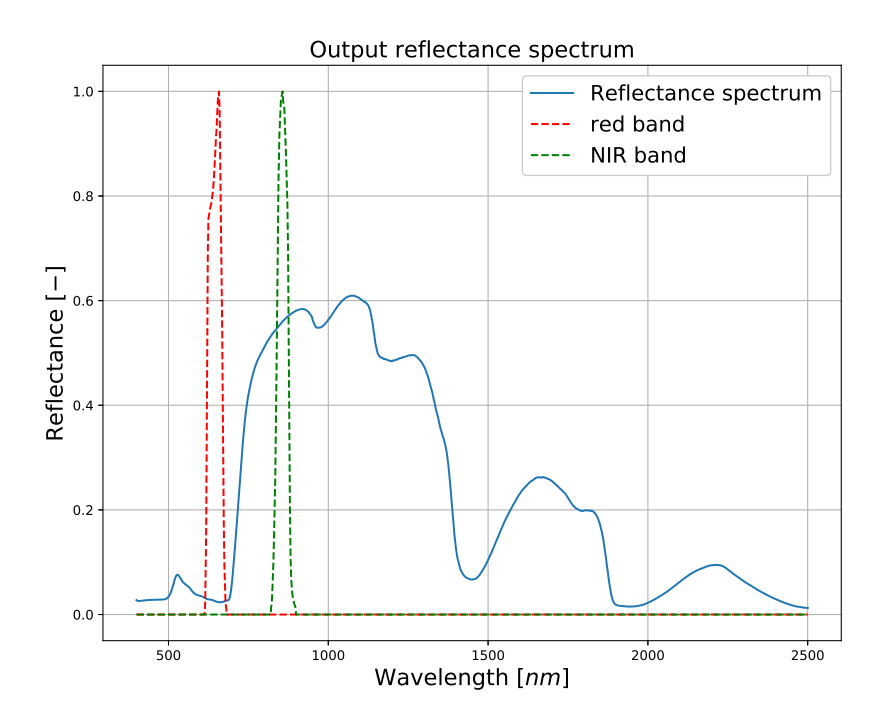


Figure 3.5: Spectral Response Function (SRF) of MODIS Aqua sensor overlaid on surface reflectance spectrum as simulated by PROSAIL.

α f_c	$f_c = 0.5\%$	$f_c = 1.5\%$	$f_c = 3\%$
$\alpha = 1$	(1, 0.5%)	(1, 1.5%)	(1,3%)
$\alpha = 2$	(2, 0.5%)	(2, 1.5%)	(2,3%)
$\alpha = 3$	(3, 0.5%)	(3, 1.5%)	(3,3%)
$\alpha = 4$	(4, 0.5%)	(4, 1.5%)	(4,3%)
$\alpha = 5$	(5, 0.5%)	(5, 1.5%)	(5,3%)

Table 3.5: Table of all cloud contamination scenarios, defined by varying the fraction of cloud contamination f_c , and the number of contaminated observations α .

- Selected all pixels in each image with a quality state flag of 'definitely cloudy'.
- 2. Filtered out all pixels with a land cover flag of 'water'.
- 3. Filtered out all pixels with a positive NDVI value.
- 4. Calculated the average red and NIR band reflectances for all 3,000,000 remaining pixels.

The result was a 'generic cloud' pixel with $\rho_{red}=0.813$, $\rho_{NIR}=0.789$ and NDVI=-0.015. With this information and the linear spectral mixing model 3.1, noisy samples representing several types of contamination scenarios could be calculated.

A range of possible scenarios that could occur were defined. Two variables were varied per composite scenario: the fraction of cloud contamination f_c , and the number of contaminated observations α . f_c was varied between cases of low (0.5%), medium (1.5%) and high (3.0%) cloud contamination, and α was varied from $\alpha = 1$ to $\alpha = 5$ (1 to 5 noisy observations). All permutations of f_c and α were used to define a grid of possible scenarios, shown in table 3.5.

For each noise-free sample simulated in 3.5, all of the noise scenarios in table 3.5 were applied using equation 3.1. In figure 3.6 an example of noise-free retrievals versus those from the cloud contamination scenario $(\alpha, f_c) = (3, 1.0\%)$ can be seen.

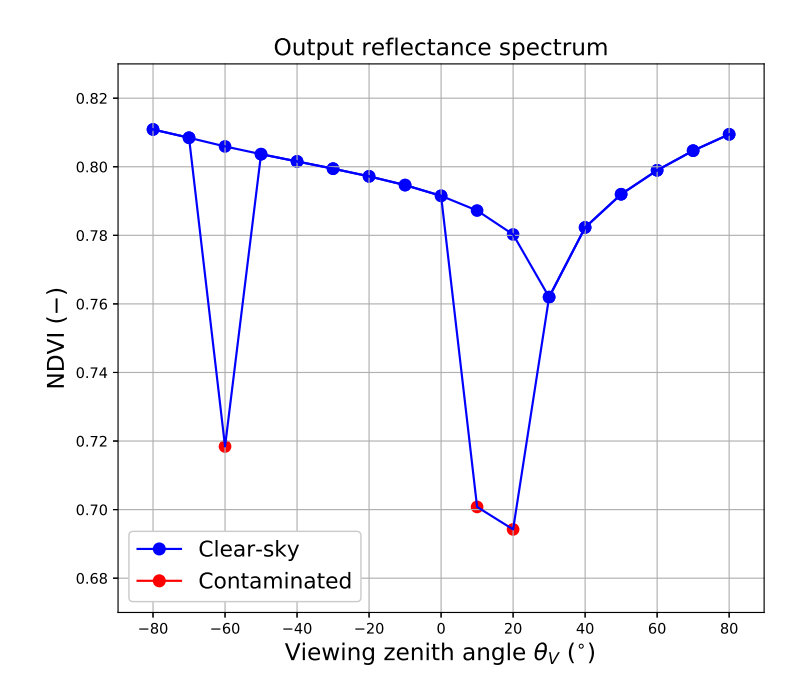


Figure 3.6: Comparison of noise-free (blue points) pseudo-observations in sample and contaminated observations (red points). Generated along principal plane ($\phi_r = 0$) so that the v-shaped directionality is clearly visible, as well as the red points deviation from it. The observations are contaminated with a low cloud fraction of $f_c = 0.5\%$ using the linear spectral mixing model.

To account for the fact that the accuracy of the BRDF reconstruction may be affected differently depending on which pseudo-observations out of the sample were contaminated, a noisy sample was created for each possible combination of noisy observations and clear-sky observations. In this way, the BRDF reconstructions performed in 3.7 could be repeated for each variation of the noisy sample.

In summary

A linear spectral mixing model was used to simulate the effect of noise due to cloud contamination. Using this method, the top of cloud reflectance was combined with observations in the noise-free surface reflectance simulated in step 3.5. In order to do this a minor side-study was performed to compute the average red and NIR cloud reflectance $\rho_{c,red}$ and $\rho_{c,NIR}$ for a 'generic cloud' for each site. Furthermore, a grid of cloud contamination scenarios was defined, with the number of contaminated observations α on one axis, and degree of contamination f_c on the other.

For a scenario of e.g. two noisy pseudo-observations ($\alpha=2$), all combinations of two contaminated measurements and remaining clear-sky measurements were found and used to create noisy samples. This was done for each scenario in table 3.5.

3.7. Estimating Ross-Li-Maignan model with OLS, LiGao and CWI methods

The final step of the numerical experiment was using three different methods to fit a Ross-Li-Maignan BRDF to the sample. These were the conventional OLS fitting, the iterative LiGao method which uses a NDVI-based indicator to reduce the weight of noisy observations, and the novel CWI method which improves on LiGao's approach by also using *a posteriori* calculated variance of the observations in the weighting process.

Using these three different methods, the RLM model's kernel coefficients were estimated using the noisy samples of each surface's BRDF. As explained in section 3.6 this was repeated for each combination of noisy and noise-free observations per scenario. In this way, a range of possible estimates was produced for each scenario, with contamination of each observation being considered. As an example,

CWI estimate of red BRDF, 2 noisy observations

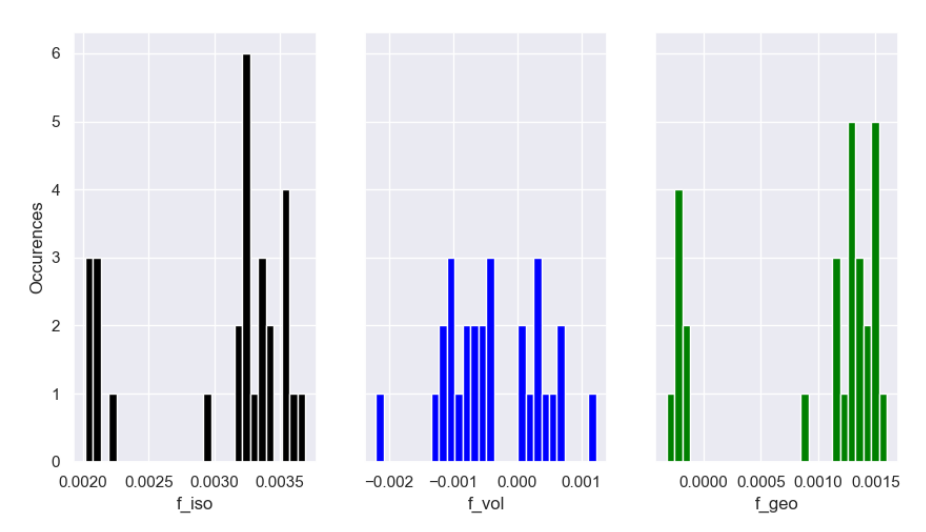


Figure 3.7: Spread of BRDF model parameters $(f_{iso}, f_{vol}, f_{geo})_{CWI}$ estimated using the CWI method. For each permutation of 2 noisy measurements, a noisy sample was calculated according to the method described in section 3.6. The histogram visualises the distribution of possible estimates, depending on which random 2 pseudo-obervatios are contaminated. The median value of each coefficient was used as the resulting estimate for the given surface and scenario.

the variability within the estimates is shown in figure 3.7 for the CWI method.

The median value of each kernel coefficient was taken as the result for a given cloud contamination scenario (α , f_c). So, from the three different methods, this resulted in three different estimates of the RLM BRDF model to characterise a surface's anisotropy:

$$(f_{iso}, f_{vol}, f_{geo})_{OLS}$$

$$(f_{iso}, f_{vol}, f_{geo})_{LiGao}$$

$$(f_{iso}, f_{vol}, f_{geo})_{CWI}$$

$$(3.2)$$

In summary

The OLS, Li-Gao and CWI BRDF-fitting methods were used to estimate the Ross-Li-Maignan BRDF parameters from noisy samples of the surface BRDF. All noise scenarios from table 3.5 were considered, and in each case the median result of each possible combination of noisy/noise-free observations in the sample was selected. The resulted in three different estimates of the same surface's BRDF, for a given surface and cloud contamination scenario.

3.8. Methodology - conclusion

The anisotropical behaviour of surface reflectance varies with canopy architecture, leaf type, and background soil type. As an alternative to validating estimated NDVI composite values with ground data, which is expensive and inherently limited to the surface types present on site, a numerical experiment was designed using the radiative transfer model PROSAIL.

With this experiment, the performance of the Changing-Weight-Iterative (CWI) BRDF-fitting method could be tested on pseudo-observations of many different types of surfaces. Noise in the measurements is a big challenge in NDVI compositing, so it was important to consider situations of cloud contamination. As it intended to be used as a part of the MuSyQ algorithm to create a global NDVI-product, as many possible surface types and retrieval conditions needed to be considered.

Using the methodology explained in this chapter, samples of surface BRDFs in the red and NIR bands were simulated using the PROSAIL model. In order to cover a broad range of globally representative conditions, the parameter space of PROSAIL was sampled 6,000 times, each sampling point yielding a different surface type.

Firstly, noise-free samples on the basis of sun-view-target geometry collected from actual study

sites were created. Synthetic noise was added the observations in the sample, using a linear spectral mixing model to simulate the effects of sub-pixel cloud contamination. Cloud-contaminated observation were synthesised by mixing the noise-free red and NIR surface reflectance measurements, with the reflectance of a 'generic' cloudy pixel - which has a far smaller (negative) NDVI. This led to noisy samples, containing both noise-free and contaminated observations. These samples ranged in amount of noisy observations (α) from 1 to 5, and varied in fraction of cloud mixing (f_c) from 0.5% to 3.0%.

Finally, the Ross-Li-Maignan BRDF model was fitted to these samples, using the OLS, Li-Gao, and Changing-Weight Iterative (CWI) methods. For each of the 6,000 surface types, three estimates were made of the surface BRDF, under each cloud-contamination scenario in table 3.5. With the large amount of experimental data produced, the performance of the CWI method could be evaluated and compared to the alternative, more conventional methods of OLS and LiGao.

4

Results and Discussion

The large amount of data generated by the numerical experiment covers a broad range of noise scenarios, a large set of vegetation canopies, and three different geometries based on the chosen study sites. As CWI was designed to be used in the production of a global NDVI product, this was necessary to cover many different types of conditions. In this chapter, three different BRDF-estimation methods, OLS, Li-Gao, and CWI, are evaluated and compared against each other, using reference values calculated from the PROSAIL model.

The results have been grouped by study site, and sky plots of the sun-view-geometry extracted from each site can be see in figure 4.1. In this chapter the information is summarised, analysed and discussed, in order to be able to evaluate the performance of the Changing-Weight Iterative BRDF-fitting method compared to the conventional OLS and LiGao methods.

In the first part of the results chapter, section 4.1, the noise-free scenario is considered. First, for ideal-conditions, the suitability of the RLM BRDF model is evaluated. As kernel-driven BRDF models are parametric models that only approximate a surface's BRDF, the RLM model's ability to describe the anisotropical surface reflectance must be studied. For these clear-sky conditions, baseline estimates of the BRDF model parameters are also reported - these are the best-achievable results for estimates made from noisy samples. The term BRDF model parameters and kernel coefficients may be used interchangeably, as they are essentially the same.

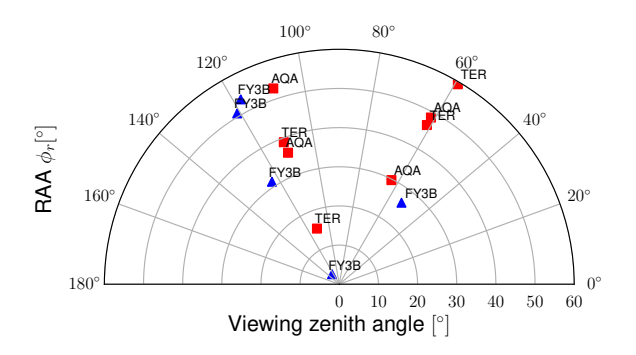
In section 4.2, the estimates resulting from noisy samples are considered. The results of the estimated BRDF parameters, as well as the NDVI composites calculated using these parameters, are both presented. OLS, LiGao, and CWI NDVI composites are compared to the baseline estimates, and also compared to reference values from PROSAIL.

Finally, the methodology implemented by this experiment and the implications of some design choices are presented in section 4.3. Results from the experiment are also related to existing literature where possible, and similarities or differences with other research are discussed.

(a) Site Chang Baishan, geographic location: 42°4′N127°36′E.

36

(b) Site Harvard Forest, geographic location: 42°37′N70°51′W.



(c) Site Mongu, geographic location: 58°17′N14°49′E.

Figure 4.1: Skyplot of all valid MODIS and MERSI measurements for a single pixel containing the study site. 8 observations were extracted for the site Chang Baishan (China), 10 for Harvard Forest (USA), and 13 for Mongu (Zambia). The pixel closest to the site was used. Red squares indicate retrievals from the MODIS sensor, while blue triangles are from the MERSI sensor.

4.1. Clear-sky conditions

MODIS and MERSI viewing geometry over 5 days was extracted for the study sites at St. Petersburg, Chang Baishan, and Mongu. Only valid observations were considered, meaning there were no obvious clouds based on the cloud masks, no sensor failures, or night-time measurements. This was done in the same way as the MuSyQ algorithm [21] and CWI paper [61], as explained in section 3.4.1.

The extracted geometry showed variability between the study sites, both in the total number of retrievals, and the amount of observations ultimately being deemed valid. These are visualised in figure 4.1, with 8 valid observations for site Chang Baishan, 10 for Harvard Forest, and 13 for Mongu.

This variability in sample size between sites is not only due to weather conditions and sensor failures, but due to the orbital tracks of the satellite platforms on which the sensors are installed. Coverage and geometry therefore vary depending on the latitude of the study site, as well as how far off-nadir the site is (the latter determins the viewing zenith angle θ_V).

Noise-free samples were simulated for each surface generated in section 3.3, according to the methodology of chapter 3, using the sun-target-view geometries shown in figure 4.1. These were used to evaluate the RLM model and composite NDVI estimates under ideal conditions, which are presented in this chapter.

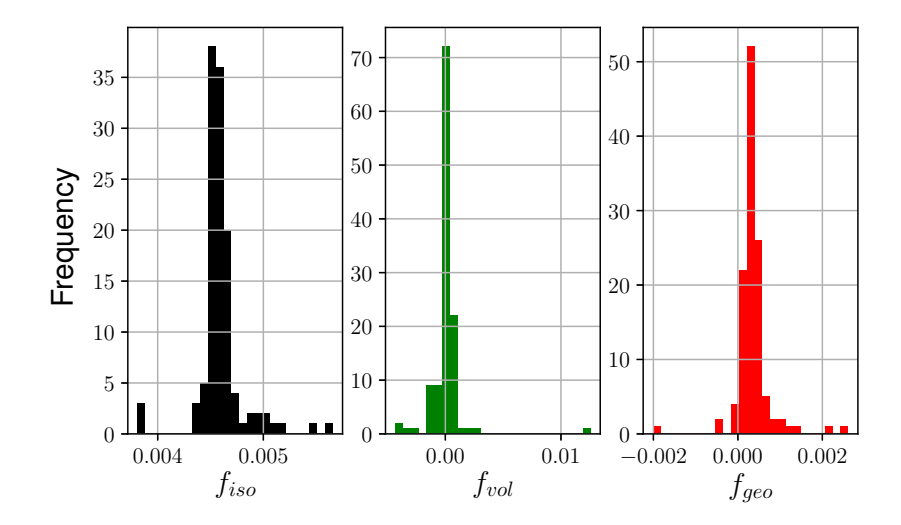


Figure 4.2: Histogram of possible RLM model parameter estimates from noise-free sample for the NIR band. Shown here for a single surface, for site Harvard Forest. Each triplet of observations within the sample yielded one set of solutions $(f_{iso}, f_{vol}, f_{geo})_e$. The coefficients are all focused on narrow bands of values with some outliers, with low variances of $(\sigma_{f_{iso}}^2, \sigma_{f_{vol}}^2, \sigma_{f_{aeo}}^2) = (3.55e-8, 2.15e-6, 2.99e-7)$

4.1.1. Suitability of RLM model

The RLM model was studied using noise-free samples with the angular sampling of just one site, Harvard forest (see figure 4.1b). If the RLM model is a good descriptor of the surface BRDF, there should be a single set of kernel cofficients that closely describes the shape of all pseudo-observations in the sample. By taking subsets of observations from the sample, and fitting the RLM model to each subset, we can study how the estimated parameters vary. All the pseudo-observations are resultant from the same surface BRDF and its anisotropy, so in the ideal case this variability is minimal or zero.

This was studied as follows: the RLM model was fitted to different combinations of three observations within the sample. With three unknowns in the inverse problem (the kernel coefficients), each triplet of observations was sufficient to estimate a solution for the RLM model. Every triplet therefore yielded one estimate of the RLM kernel cofficients f_{iso} , f_{vol} and f_{geo} . For this set of different possible solutions, the variances $(\sigma_{f_{iso}}^2, \sigma_{f_{vol}}^2, \sigma_{f_{geo}}^2)$ of each coefficient was calculated.

The histogram in figure 4.3 shows the distribution of these variances, limited to a subset of 1,000 surfaces due to high computational cost. In order to judge the significance of this variance, we select a surface which had a variance near the median of these distributions.

The spread of these estimated kernel coefficients is demonstrated for this single surface in figure 4.2. A relatively narrow spread of estimates indicates that the estimates are generally converging to a narrow set of solutions (see variance of the coefficients in the caption of figure 4.2).

Taking the median of this spread to get a unique set of RLM model parameters, we can use the RLM model to calculate the reflectance values of the pseudo-observations, and compare them to the actual pseudo-observations. In figure 4.4, we see that the RLM model matches the shape of the pseudo-observations very closely. The RMSE of the NDVI values is low, at 0.00829.

Looking at the distributions in figure 4.3, we see that for most surfaces the variance of estimates is minimal. The results indicate that the Ross-Li-Maignan model is reasonably accurate descriptor of a surface's BRDF, for most surface types.

The low variance of most surfaces' estimates suggests that the BRDF parameters fitted to one triplet of observations in a sample could also closely match another triplet in the sample - indicating a good description of the samples surface BRDF. A demonstration of this high closeness of fit between the calculated and observed reflectance values was shown for a single case in 4.4 as an example.

This conclusion is also supported by existing literature Li Gao et al. (2002) [11] which considers the RLM model it to have a high accuracy among the existing kernel-models available ¹, and it has been used operationally for the creation of other existing satellite products as well.

¹As was discussed in section 2.4.2, there exist a variety of parametric BRDF models.

Variance of RLM model estimates per surface - NIR band

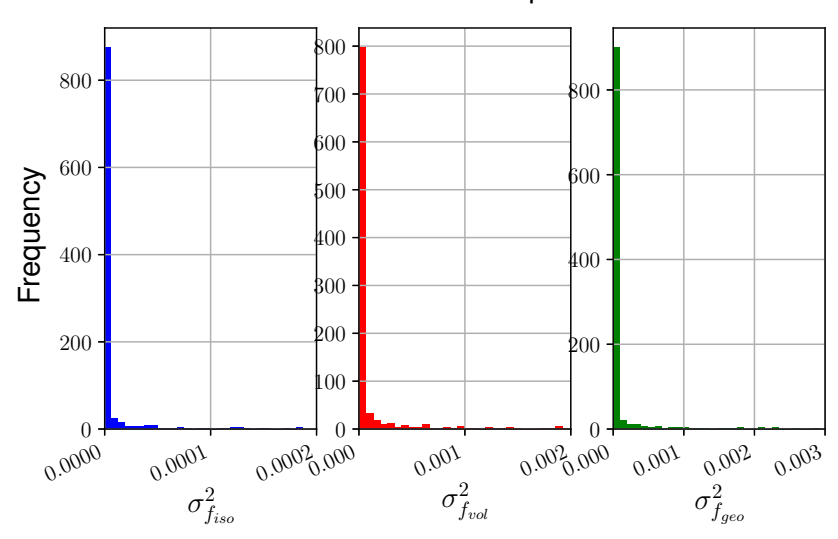


Figure 4.3: Variance of the possible RLM model parameter estimates for the NIR band, shown for a subset of 1000 randomly selected surfaces. The distributions are strongly centered around variance values of 0, indicating that for the majority of surfaces, the RLM model estimates converge to a narrow set of solutions.

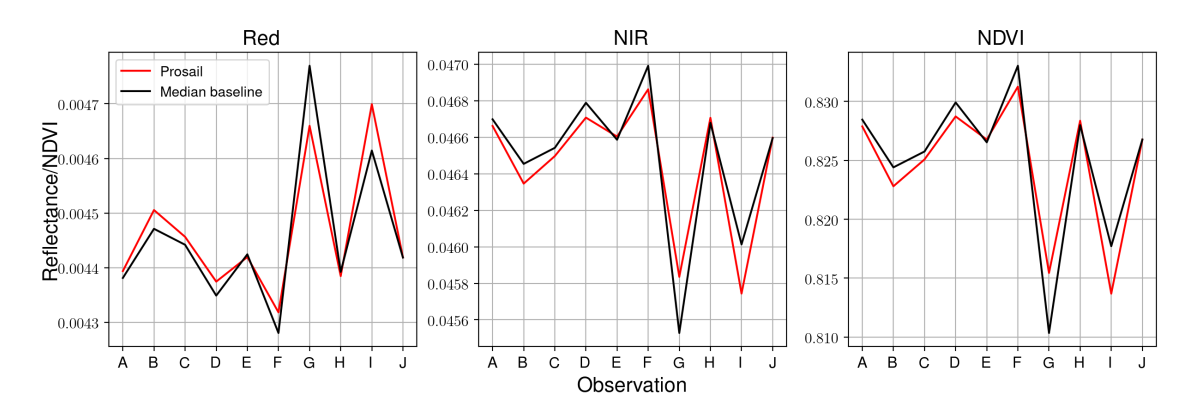


Figure 4.4: Side by side comparison of a noise-free sample as simulated by PROSAIL, compared to same observations as calculated by a fitted RLM model. The model parameters used are the median of the spread shown in figure 4.2, which had a narrow spread within the estimates. The RMSE of the estimated NDVI is 0.0083.

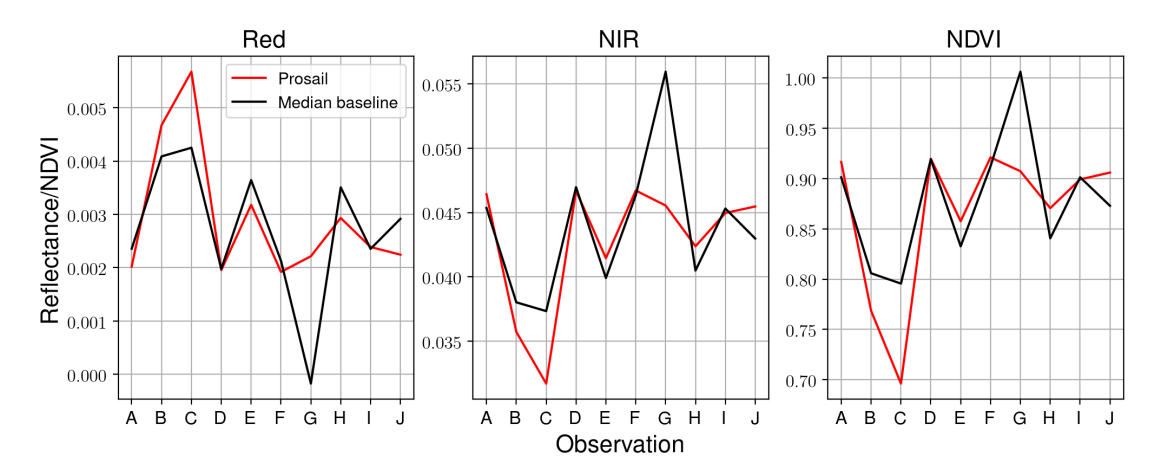


Figure 4.5: Side by side comparison of surface reflectance pseudo-observations as simulated by PROSAIL, compared to reflectance as calculated by the RLM model fitted to the noise-free sample. The model parameters used are for a surface with high variance in the estimated kernel coefficients. The RMSE of the estimated NDVI is 0.0942.

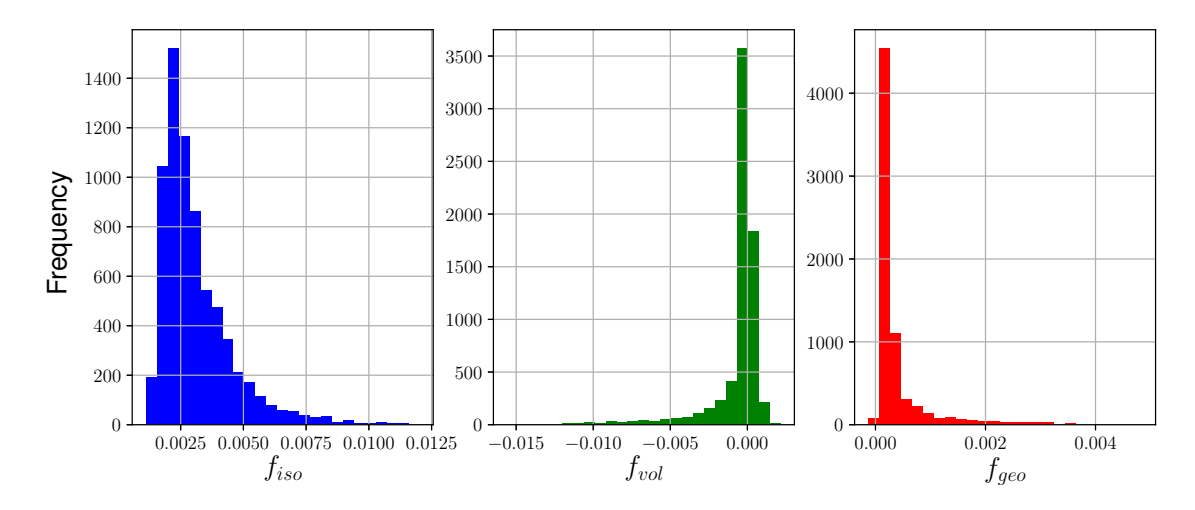


Figure 4.6: Distribution of RLM BRDF model parameters from noise-free samples, for 6,000 surfaces. Angular sampling is for the site Harvard Forest.

Some high variance cases were also observed, and the RLM's fit for these cases is demonstrated in figure 4.5 - where it performs less adequately. A review of parametric BRDF modelling by Lucht et al. (2000) [29] noted that it was unclear if a single BRDF model exists which can be fitted to the majority of the BRDF shapes observed in ground-measured field data. In this case, with 6,000 different surface types being simulated, these outliers are surfaces that are not well approximated by the RLM model. With this limitation of parametric BRDF models in mind, both Lucht et al. (2000) [29] as well as Wanner et al. (1995) [57] drew similar conclusions that the RLM model is applicable to a broad variety of BRDF shapes.

The above discussion is based on the results for the surface's NIR band BRDF, and similar results were observed with the red band, with no notable differences. The closeness off fit of an example red band estimate can also be seen in figure 4.4. In the appendix, figure B.1, the distribution of the variance for the red band can be seen. Furthermore, the results of this section were also reproduced for the other sites Mongu and Chang Baishan and were very similar.

4.1.2. Baseline BRDF model estimates

As discussed in section 2.3.1, a surface's BRDF can not be perfectly described, only estimated a group measurements, which together for a sample. In this case, a Ross-Li-Maignan BRDF model is fitted to the measurements, in an attempt to describe the surface anisotropy.

The suitability of this model and ability to describe the surface BRDF was already described in section 4.1.1, and here the spread of estimated RLM BRDF parameters from noise-free samples are briefly presented, to be used as a reference in section 4.2.1 for the estimates from noisy samples.

Figure 4.6 shows the distributions of the three individual kernel coefficients f_{iso} , f_{vol} and f_{geo} . These distributions do not contain any information on their own, but represent the ideal scenario for the BRDF estimates. If the studied methods reduce the impact of noise perfectly, the estimates from noisy samples can be expected to match these closely. Figure 4.6 shows the baseline scenario for Harvard forest, as each site's estimates should be compared to its respective ideal estimate.

4.1.3. NDVI estimates under clear-sky conditions - baseline scenario

Using the RLM BRDF parameters estimated from noise-free samples of the surfaces, the composite NDVI value was calculated for standardized geometry. This was at nadir-viewing, fixed sun conditions of $(\theta_V, \theta_S, \phi_r) = (0, 30, 0)$. As this calculated using an estimated BRDF model, this nadir-normalised value will be referred to as the NBAR NDVI (Nadir BRDF-Adjusted Reflectance NDVI).

In figure 4.7 these estimated NBAR NDVI values are seen to the reference values from PROSAIL, for site Harvard Forest. For all the sites the main cluster is centered on the 1:1 line, indicating the PROSAIL reference values are matched closely, with some NDVI values outside of the main cluster that are being overestimated.

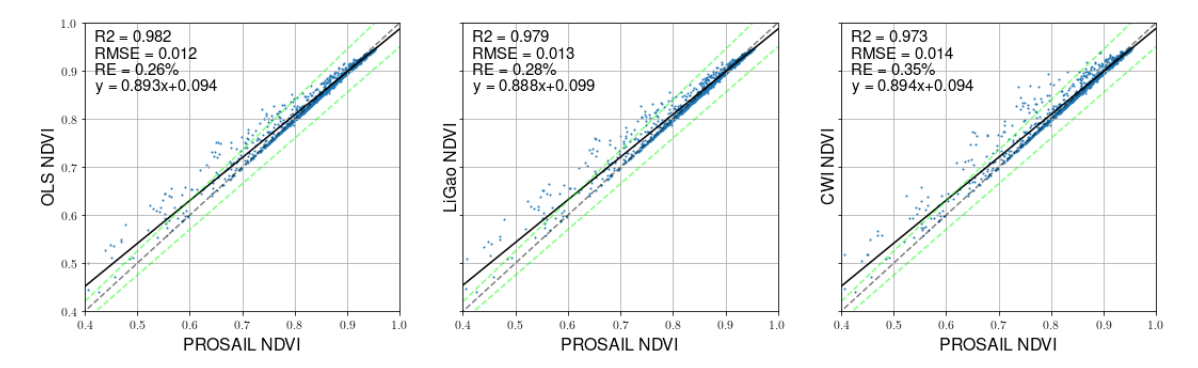


Figure 4.7: Scatter plot of estimated NDVI compared to reference NDVI value from PROSAIL, for site Harvard Forest. Shown here are NDVI values calculated using BRDF parameters estimated from noise-free samples using OLS, Li-Gao, and CWI methods. Dotted line is 1:1 line, green lines are ±5%.

A significant linear agreement is noted between the estimated and reference NBAR NDVI values, for all three methods, with low RMSE values. While they are low, it is noted that the LiGao and CWI methods have slightly higher RMSE values of 0.013 and 0.014, respectively, compared to 0.012 for OLS. As the LiGao and CWI methods iteratively attempt to reduce the weight of noisy observations in the BRDF fitting process, the use of weight matrices appears to have a small negative impact on the accuracy of the estimate, for the noise-free case. The results suggest that observations which are in fact noise-free, have their weight reduced erroneously.

The findings suggest that for the ideal scenario, the Ross-Li-Maignan model matches PROSAIL NBARS for all surfaces very closely, with RMSE values below 0.02 regardless of the estimation method. For reference, we saw in section 4.1.1 and figure 4.2 that a very close fitting NDVI estimate has an RMSE of 0.0083. The majority of surfaces are within 5% of the reference PROSAIL value, suggesting that the (synthetic) surface BRDFs can all be described well using the RLM model. Similar results were observed for sites Chang Baishan and Mongu (see appendix, figures C.1 and C.2) and are not discussed further here.

Looking at Zeng et al. (2016) [61], a similar validation of the CWI method was performed, but on the basis of imagery from the ETM+ sensor aboard the Landsat 7 satellite. These reference images from the ETM+ sensor were near-nadir viewing, and due to this sensor being used in multiple other papers it was deemed by Zeng et al. (2016)[61] to be a reasonable validation source.

In figure 4.8 a scatter plot of NBAR NDVI estimated from MODIS imagery using the CWI method is seen. Zeng et al. (2016) performed it's validation for the same study site of Harvard Forest, but using only MODIS surface reflectance observations, not including data from multiple sensors as this experiment does. Furthermore, 16 days of images were used, instead of 5 days as was done in this experiment. Zeng et al. (2016) [61] performed a careful screening of the observations used and deemed them to be free of cloud-contamination, as was also done for the results presented in figure 4.7 of this experiment

With the differences in mind, similar results are nevertheless observed as in figure 4.7. The results shown in figure 4.8 also show a significant linear relationship between the estimated and reference NBAR NDVI values. The agreement between these two studies further supports that the RLM model, as fitted using the CWI method, is a reasonably accurate descriptor of the surface BRDF.

However, for this experiment, each point in figure 4.7 represents a surface, whereas for Zeng et al. (2016)[61], actual surface reflectance measurements of Harvard Forest were used, meaning each point represents one pixel in the images of the Harvard Forest site. Their findings are therefore restricted to biome of the study site, in this case of a broadleaf forest.

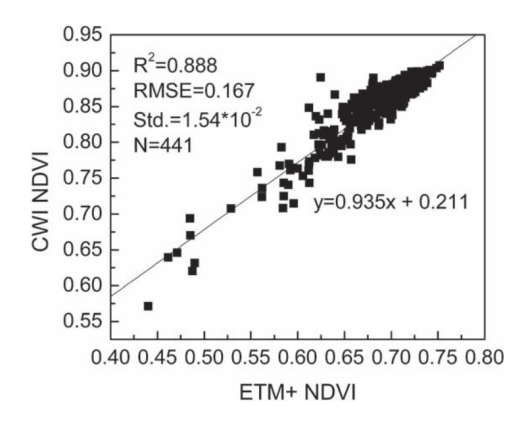


Figure 4.8: Direct validation of CWI method using imagery from the ETM+ sensor, Harvard Forest site, as reported by Zeng et al. [61].

4.2. Estimating from noisy samples

With an understanding of the suitability of the Ross-Li-Maignan model at the centre of the CWI method, and the CWI's performance using noise-free samples, the three methods are compared here for the various cases of noise samples due to cloud-contamination. Firstly the results of estimating the BRDF model parameters are discussed. From these estimates, NBAR NDVI values are calculated, and compared to the reference PROSAIL values.

The results are not directly comparable between sites due to the different sun-target-view geometry and number of observations, and so are grouped by study site. The sky plots of sites Mongu, Chang Baishan and Harvard Forest can be seen in figures 4.1c, 4.1a and 4.1b respectively.

4.2.1. BRDF model estimates from noisy samples

For the 6,000 surfaces, the RLM BRDF parameters were estimated using each of the noisy samples resulting from each of the cloud contamination scenarios. The same was already done in section 4.1.2, but with noise-free samples, creating a baseline scenario.

Distributions of the estimated parameters are shown for two scenarios in figure 4.9, compared with the baseline parameters. If the effect of noisy obserations is effectively suppressed, the estimates of the kernel coefficients, in this case f_{iso} , are expected to have a similar distribution as the baseline, noise-free case.

The cloud-contamination scenario for figure 4.9 is $f_c=3.0\%$, with $\alpha=2$ and $\alpha=5$. For this scenario, the distribution of the CWI estimate appears to be closest to the baseline scenario. When calculating the deviation from the baseline and inspecting the result (bottom figure), this is confirmed to be the case.

Looking at another scenario, a different distribution is noted. In figure 4.10, the Li-Gao estimates have a closer shape to the baseline compared to the CWI estimates, although all three methods show significant differences. This is a case of severe cloud contamination, with 5 contaminated observations in a sample of size 10, where all the estimates are significantly negatively impacted.

From these distributions it can be concluded that for some scenarios, for the 6,000 surfaces simulated, the CWI method closely matches the BRDF parameters fitted to the noise-free samples (i.e. the baseline). In other cases, such as in figure 4.10, the impact of noisy observations is not effectively reduced by any of the methods, with CWI appearing to show larger differences than Li-Gao.

The impact of cloud-contamination appears to lead to an overestimation the isometric scattering kernel coefficient f_{iso} of the RLM model in the case of cloud contaminated observations. Isometric scattering is an isotropic feature, and describes the general 'brightness' of a surface. Since pixels with sub-pixel cloud contamination are generally brighter in the red band, these noisy observations lead to an overestimation of the brightness in the red band when their impact is not suppressed.

Due to time constraints, the results for the volumetric scattering and geometric scattering kernel coefficients f_{vol} and f_{aeo} are outside of the scope of this research ². However, as estimating a NDVI

²In appendix D some results for the other coefficients can be viewed.

42

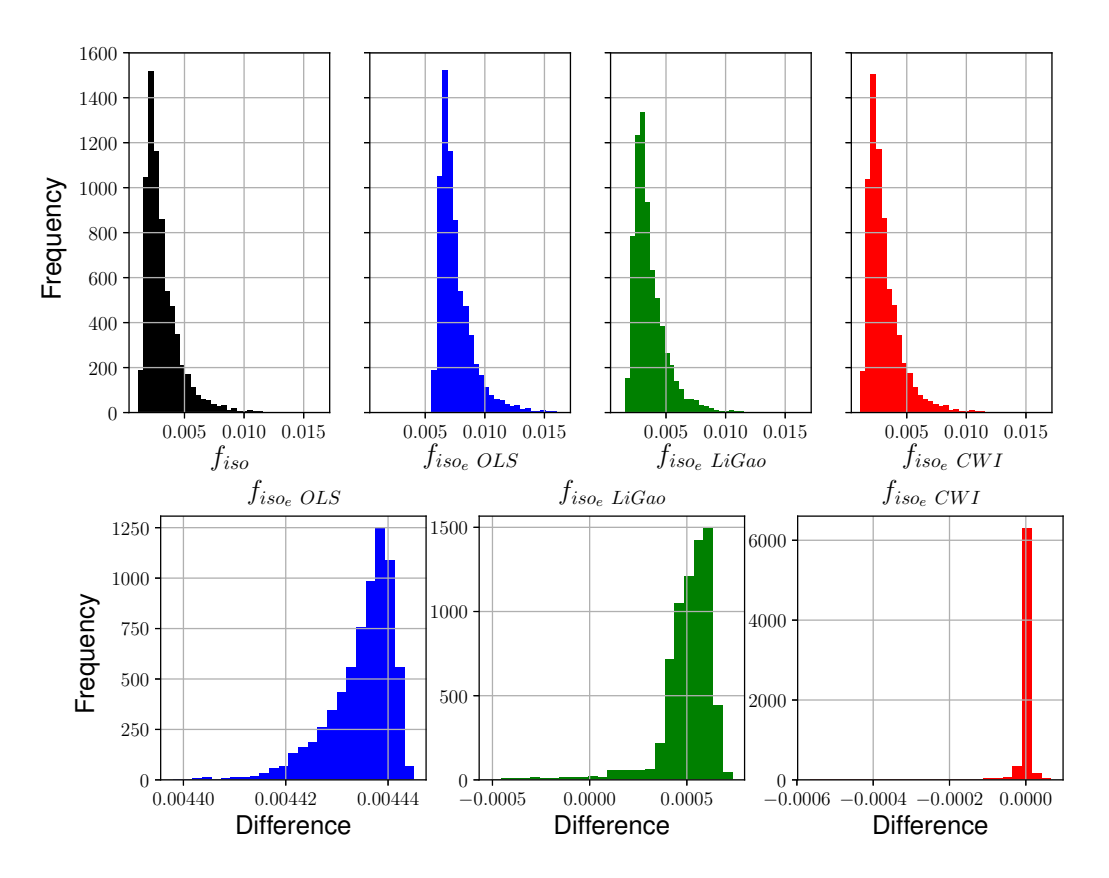


Figure 4.9: Estimates of the red band kernel coefficients, for the scenario $(\alpha, f_c) = (2, 3.0\%)$ at site Harvard Forest. Top: distributions of the baseline f_{iso} parameters and OLS, Li-Gao, and CWI estimates. Bottom: distributions of deviations from baseline f_{iso} values for OLS, Li-Gao, and CWI estimates. Note the scale of the x-axis.

composite value is the major application of CWI in this context, the focus is on the impact of the estimated BRDF parameters on the resulting NDVI estimates - which is discussed in the following sections.

4.2.2. Nadir-normalised NDVI estimates from noisy samples - low cloud fraction

The estimates resulting from the noisy samples showed varying results, depending on the degree of contamination and number of contaminated observations α . First, the case of low cloud contamination $f_c = 0.5\%$ in the sample is considered. The estimated NBAR NDVI values were plotted against the reference PROSAIL values, similar to the clear-sky estimates figure 4.7, in figure 4.11.

With a cloud fraction of $f_c=0.5\%$, the mean reduction in NDVI value of contaminated observations was 15.5%. However, this varies greatly between different surfaces and their measurements, as the linear spectral mixing model used to add sub-pixel cloud noise combines surface reflectance (which varies per surface type) with the top of cloud reflectance.

In figure 4.11, for site Harvard Forest, we notice that the accuracy of each estimation method suffers from the presence of lightly contaminated observations in the sample. For all methods, the RMSE gradually increases with α , and the fitted BRDFs under-estimate the NDVI values compared to PROSAIL (reference values on x-axis).

With $\alpha=1$ the RMSE values for all three methods are equal or nearly equal to the baseline, ideal scenario, ranging from 0.011 for CWI to 0.015 for OLS. At $\alpha=5$, the RMSE is significantly higher than the baseline for all three scenarios, with CWI having an RMSE of 0.084 compared to 0.017 when $\alpha=0$. Bases on these RMSE values, it is observed that both Li-Gao and CWI methods outperform OLS, but not by a large margin on average. The impact of noisy observations does not appear to be significantly reduced by any of the methods, however the impact is also not very high for low α values of 1 or 2.

Table 4.1 summarises the results for the low cloud contamination scenario, also for the Mongu and and Chang Baishan sites. Similar results are observed for these other sites, however the reduction

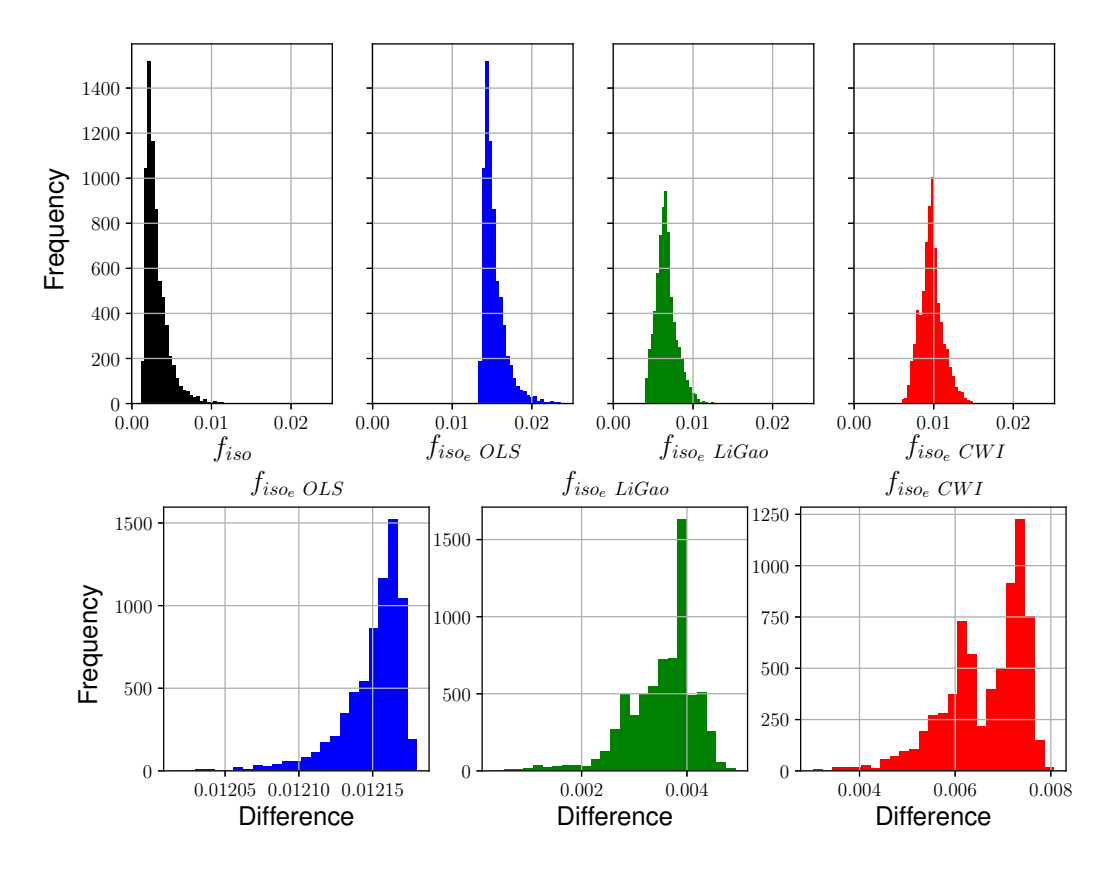


Figure 4.10: Same as figure 4.9, for $\alpha=5$, at site Harvard Forest. Top: distributions of the baseline f_{iso} parameters and OLS, Li-Gao, and CWI estimates. Bottom: distributions of deviations from baseline f_{iso} values for OLS, Li-Gao, and CWI estimates. Note the scale of the x-axis.

in accuracy is lower for the site Mongu (which has a sample size of 13 compared to Harvard Forest's 10) and higher for the site Chang Baishan (sample size of 8). The number of pseudo-observations, or sample size, varied per site due to differences in geography and weather conditions. Differences in sample size lead to differences in the impact of noisy observations for a given α , as evidenced by table 4 1

4.2.3. Nadir-normalised NDVI estimates from noisy samples - high cloud fraction

For the case of contaminated observations having a high degree of cloud contamination, the impact of noisy observations was considerably higher. With the case $f_c = 0.5\%$, the mean reduction in NDVI value of contaminated observations was 53.2%, therefore noisy measurements had a significantly lower NDVI value.

In figure 4.12, for site Harvard Forest, we notice that the accuracy of each estimation method responds differently to the increasing amount of contaminated observations in the sample. As was suggested by the findings of section 4.2.1, sub-pixel clouds have a negative NDVI and increase the measured red reflectance, leading to an overestimated f_{iso} and underestimated NBAR NDVI. This appears to be the case for the OLS-reconstructed Ross-Li-Maignan BRDF model, which does not effectively reduce the impact of noisy observations. It has the highest RMSE of the three methods, and hence the lowest accuracy, which decreases further and further as α increases.

For the Li-Gao and CWI methods, the impact of noisy observations is more subtle. From the spread of the estimates in figure 4.12, we see that a significant linear relationship is maintained between the estimates and the reference PROSAIL value with just one or two contaminated observations in the sample, with RMSE values close to the baseline scenario of 0.013 and 0.014.

From the RMSE values summarised in table 4.2, the CWI and Li-Gao methods both appear to perform as intended, identifying and reducing the impact of the two cloud-contaminated measurements.

Table 4.1: Mean error for each scenario, quantified by the RMSE using PROSAIL as a reference value. Summarized here for α from 1 to 5 for the case of low cloud contamination $f_c = 0.5\%$, which results in a mean relative NDVI noise of 15.5% in the contaminated observations. Greener boxes indicate lower RMSE value, and red indicates higher. Note: all tables are standardised to the same scale of RMSE-colour.

	Number of contaminated observations					
Estimation method	<i>α</i> = 0	<i>α</i> = 1	α = 2	<i>α</i> = 3	α = 4	<i>α</i> = 5
			Chang	Baishan		
OLS	0,009	0,014	0,03	0,056	0,073	0,09
Li-Gao	0,01	0,011	0,018	0,04	0,059	0,078
CWI	0,017	0,01	0,014	0,051	0,068	0,084
			Ha	rvard		
OLS	0,012	0,012	0,024	0,047	0,057	0,073
Li-Gao	0,013	0,015	0,019	0,037	0,044	0,06
CWI	0,014	0,011	0,011	0,03	0,05	0,066
	Mongu					
OLS	0,021	0,027	0,042	0,041	0,054	0,059
Li-Gao	0,021	0,025	0,03	0,034	0,043	0,051
CWI	0,028	0,025	0,022	0,022	0,043	0,055

Table 4.2: Mean error for each scenario, quantified by the RMSE using PROSAIL as a reference value. Summarized here for α from 1 to 5 for the case of low cloud contamination $f_c = 3.0\%$, which results in a mean relative NDVI noise of 53.2% in the contaminated observations. The simulated samples have size 8 (Chang Baishan), 10 (Harvard Forest) and 13 (Mongu). Greener boxes indicate lower RMSE value, and red indicates higher. Note: all tables are standardised to the same scale of RMSE-color.

Number of contaminated observations						
Estimation method	<i>α</i> = 0	α = 1	α = 2	<i>α</i> = 3	α = 4	<i>α</i> = 5
			Chang	Baishan		
OLS	0,009	0,065	0,151	0,232	0,312	0,361
Li-Gao	0,01	0,012	0,031	0,083	0,136	0,176
CWI	0,017	0,01	0,009	0,114	0,228	0,263
			Har	vard		
OLS	0,012	0,086	0,118	0,22	0,259	0,312
Li-Gao	0,013	0,029	0,017	0,05	0,082	0,105
CWI	0,014	0,01	0,01	0,009	0,11	0,199
	Mongu					
OLS	0,021	0,103	0,186	0,183	0,237	0,259
Li-Gao	0,021	0,035	0,046	0,048	0,076	0,104
CWI	0,028	0,025	0,022	0,021	0,022	0,022

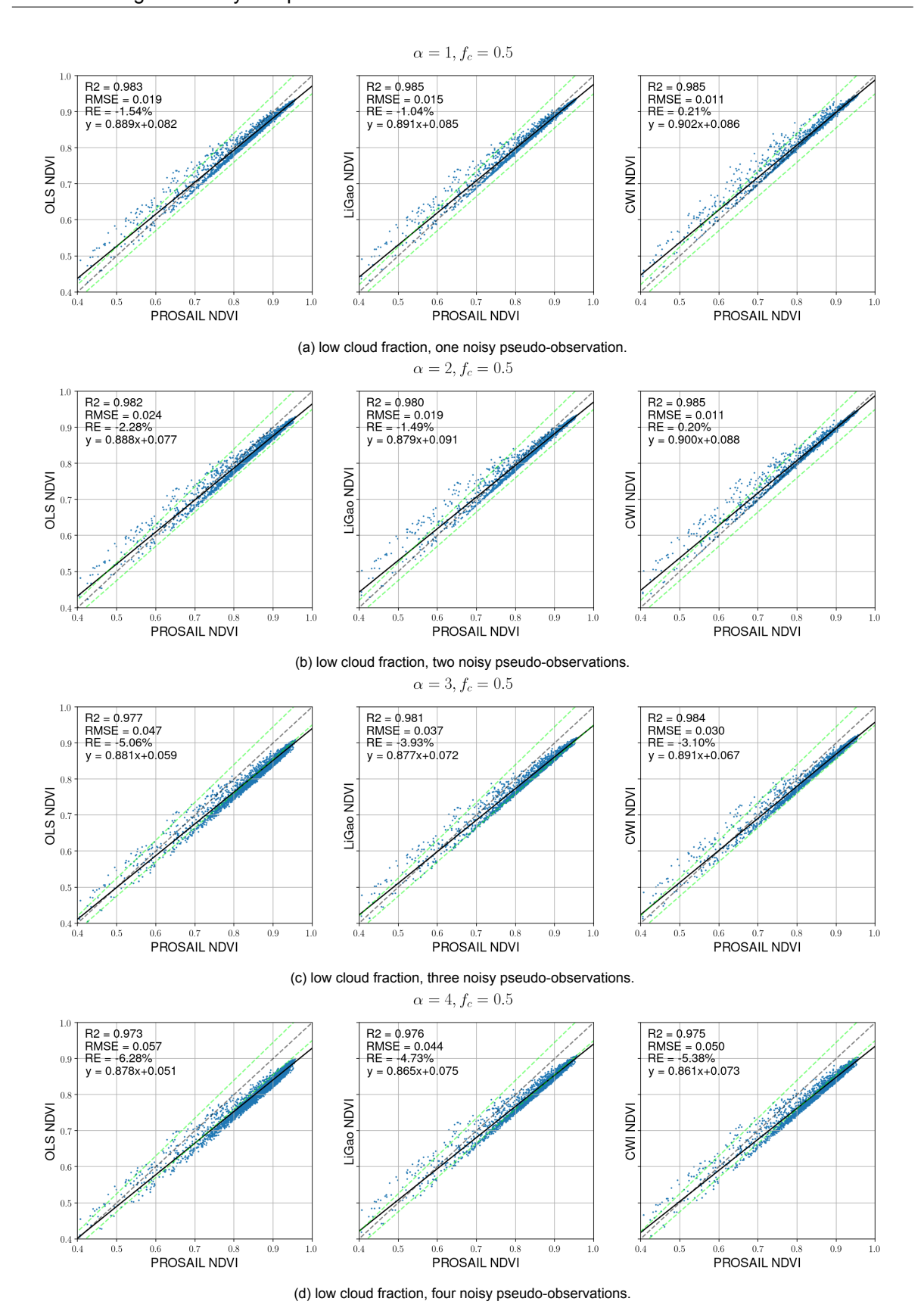


Figure 4.11: Estimated nadir-normalised NDVI versus reference PROSAIL values for study site Harvard Forest - for the case of low noise $f_c = 0.5\%$. Fitted RLM BRDF models were used to calculate the NDVI values, using the fitting methods OLS (left), LiGao (middle), CWI (right). Angular spread of the 10 observations used for the BRDF fitting can be seen in 4.1b. Each point represents the calculated values for one surface type, the black dotted line a 1:1 relationship and the green dotted indicates the threshold for the references values $\pm 5\%$.

Taking $\alpha=3$ as an example, the CWI estimates have a mean RMSE of 0.009, while those of Li-Gao have a mean of 0.05. Both CWI and Li-Gao outperform OLS, which at this point has an RMSE value nearly 20 times higher than the baseline, at 0.22.

When the proportion of contaminated observations passes a certain point, in the case of Harvard Forest the point being $\alpha=4$, the accuracy of the CWI method rapidly drops off. From $\alpha=3$ to $\alpha=4$ RMSE increases tenfold from 0.009 to 0.11. From table 4.2 this point can be clearly seen, also for site Chang Baishan where it occurs earlier, at $\alpha=3$. We note once again that Chang Baishan has a smaller sample size of 8 pseudo-observations compared to Harvard Forest which has 10 and Mongu which has 13.

At this 'tipping' point and as α increases (see full set of figures in appendix G.1), the CWI method fails to accurately adjust the weight matrix as defined in equation 2.23. As such the impact of the contaminated observations is not effectively reduced and the RMSE increases.

This sudden drop-off isn't observed for the Li-Gao estimates, which decrease gradually in mean accuracy as quantified by the RMSE values presented in table 4.2. Therefore, after the observed sudden drop-off in the accuracy of the CWI method, the Li-Gao method outperforms CWI. For example, for site Chang Baishan, when $\alpha=3$ the RMSE of the Li-Gao estimates is lower 0.083 compared to 0.114 for CWI.

This isn't observed for the site Mongu, where the CWI method very effectively suppresses the impact of the noisy observations for every α tested in the simulation. The (mean) RMSE of the estimates is even lower than the baseline scenario at 0.022, whereas the Li-Gao RMSE goes as low as 0.259.

4.2.4. Discussion of NBAR NDVI estimates

The findings suggest that low levels of sub-pixel cloud contamination are challenging to detect and mitigate in a sample, with all three methods effectively failing to do so. Gao et al. (2002) [11] made a similar observation, stating that: "if all observations are slightly contaminated, it is almost impossible to retrieve a true value from those observations without proper ancillary information".

This quote was made in reference to the Li-Gao method in particular, but is applicable to other methods as well. As was explained in the literature review, section 2.1, a surface's BRDF leads to variations in the observed surface reflectance. When light degrees of contamination are introduced, this noise is challenging to distinguish from directional variations. As such, the negative impact of these slightly contaminated observations is expected, with little difference between the reduced accuracy for the OLS, Li-Gao, and CWI methods as shown in table 4.1.

In cases where the degree of cloud contamination was high ($f_c=3.0\%$), Li-Gao and CWI showed more promising results. Both showed significant reduction of the impact of noise, when compared to OLS, with CWI out-performing Li-Gao when the number of contaminated observations was sufficiently low. These findings are corroborated by Zeng et al. (2016) [61], which also performed a validation of the CWI method, shown side by side with the results of this numerical experiment in figure 4.13.

The results from Zeng et al. (2016) [61] assumes data from a (validated) sensor ³ as a reference, and fitted the BRDF model to a sample consisting of only MODIS surface reflectance observations. This was done for 441 pixels at the site Harvard Forest.

The MODIS images used were collected over a 16-day composite cycle as opposed to a 5-day one, therefore the sample was larger, at 16 observations on average. Of these 16, an average of 6 were suspected to be noisy per pixel, according to Zeng et al. (2016) [61]. On the other hand, the estimates shown in figure 4.13b are for a sample of only 10 observations, with 3 contaminated ones. Additionally, this numerical experiment considers a globally representative set of 6,000 surface types, whereas Zeng et al. (2016) [61] is limited to the surface types present at the validation site of the Harvard Forest, which is a broadleaved forest.

Despite the differences, it is promising that the result from this experiment are qualitatively similar to existing literature on CWI. Both experiments also used the same Ross-Li-Maignan model to estimate the surface BRDFs. The results agree that the CWI method outperforms Li-Gao and OLS for this scenario, yielding higher accuracy NDVI composite estimates. But considering what was presented in sections 4.2.2 and 4.2.3, and at tables 4.1 and 4.2, it is clear that the highly accurate performance of the CWI estimate does not apply to all scenarios.

When the proportion of 'good quality' clear sky observations to contaminated ones is too low, the

³Enhanced Thematic Mapper Plus (ETM+), aboard the Landsat 7 satellite mission.

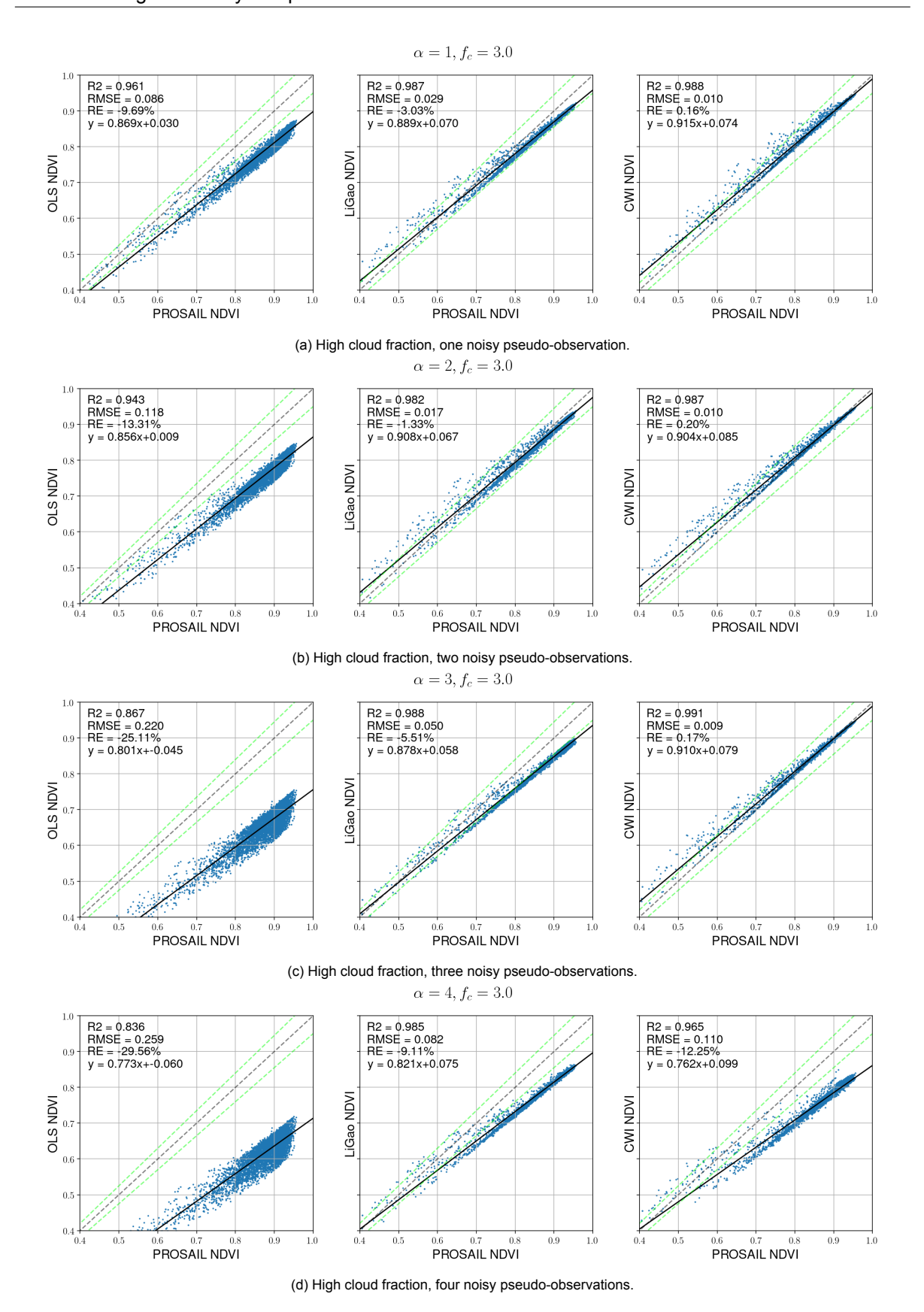
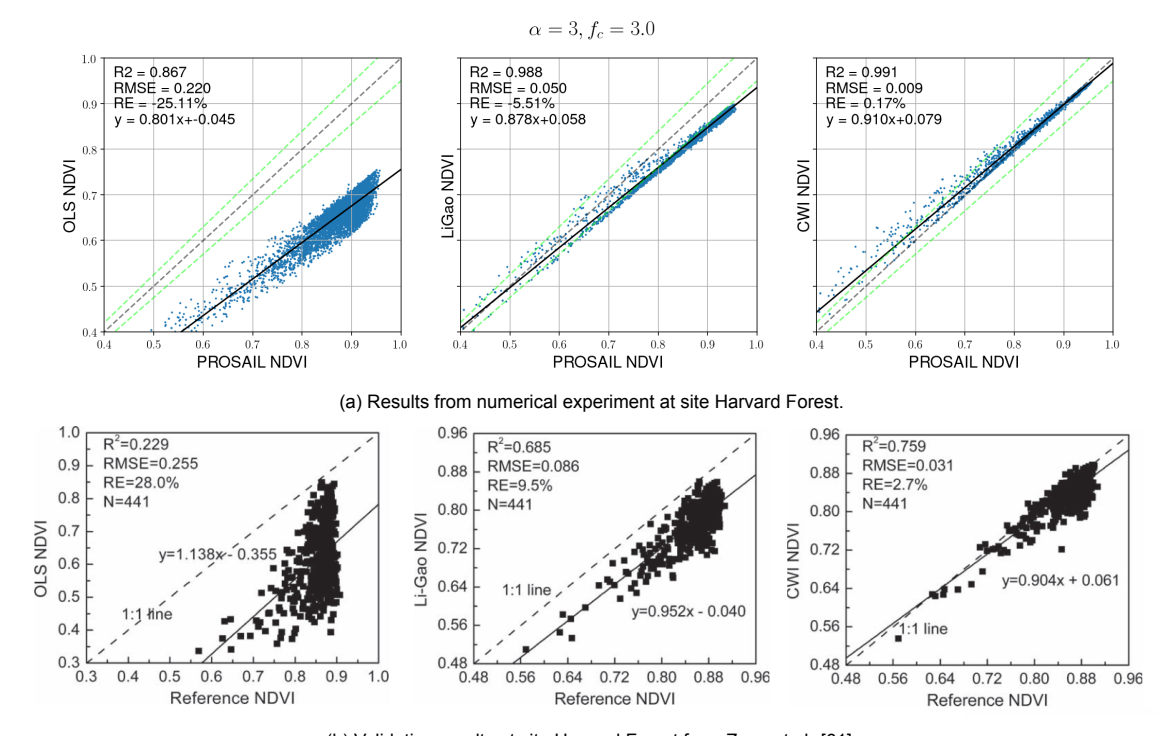


Figure 4.12: Estimated nadir-normalised NDVI versus reference PROSAIL values for study site Harvard Forest - for the case of high noise $f_c = 3.0\%$. Fitted RLM BRDF models were used to calculate the NDVI values, using the fitting methods OLS (left), LiGao (middle), CWI (right). Angular spread of the 10 observations used for the BRDF fitting can be seen in 4.1b. Each point represents the calculated values for one surface type, the black dotted line a 1:1 relationship and the green dotted indicates the threshold for the references values $\pm 5\%$.

48 4. Results and Discussion



(b) Validation results at site Harvard Forest from Zeng et al. [61].

Figure 4.13: Side by side of results from this experiment (upper), and Zeng et al. (2016) [61] (lower). Zeng et al. (2016) performed direct validation of CWI method using imagery from the ETM+ sensor as a reference, while this experiment used NDVI values modelled by PROSAIL as a reference.

The sample used by Zeng et al. (2016). to calculate the estimates contained an average of 16 observations, with 6 being suspected contaminated outliers. In the results of this experiment, for site Harvard Forest the simulated sample contained 10 observations, 3 of which are contaminated in this particular scenario.

accuracy of the CWI method drops off significantly. This point is strongly dependent on the sample size and the number of contaminated observations α , as was determined by repeating the experiment for different study sites. For high levels of cloud contamination $f_c=3.0\%$, this 'tipping point' occurs at $\alpha=3$ for site Chang Baishan with sample size 8, $\alpha=4$ for site Harvard Forest with sample size 10, and $\alpha=6$ for site Mongu with sample size 13.

For the situations successfully detects and reduces the impact of noisy observations, such as in figure 4.13b, the CWI estimates are very similar to the noise-free scenario in figure 4.7, with a very low RMSE. This implies that the weights of the contaminated observations in the sample are effectively being reduced to nearly 0, virtually completely suppressing their impact. The Li-Gao method assigns non-zero, non-negligible weights to these outliers, leading to less accurate estimates compared to CWI. Zeng et al. (2016) [61] observed the same behaviour, stating that "...by Li-Gao, the heavily contaminated observations still had non-negligible weights which had a considerable effect on the BRDF retrieval results" and "In contrast, by CWI, the weights [...] were all less than 0.01" [61].

4.3. Evaluating the experiment

The final aspect of the results is an evaluation of the methodology described in chapter 3, which was used to generate the experimental data. The design choices made in the design of the numerical experiment, and their implications, are discussed here. These are grouped by the themes of: processing of a multi-sensoral dataset, the conditions and constraints selected for the experiment, and the experiment's design as a whole.

4.3.1. Multi-sensoral dataset calibration and corrections

The combining of dataset from multiple sensors is a broad and active field of research and development in itself. Methods for quantifying sensor SRFs and the accuracy of cross-calibration are specific to the reflectance bands, sensor types, land surface processes, and sensor degradation over time. Addition-

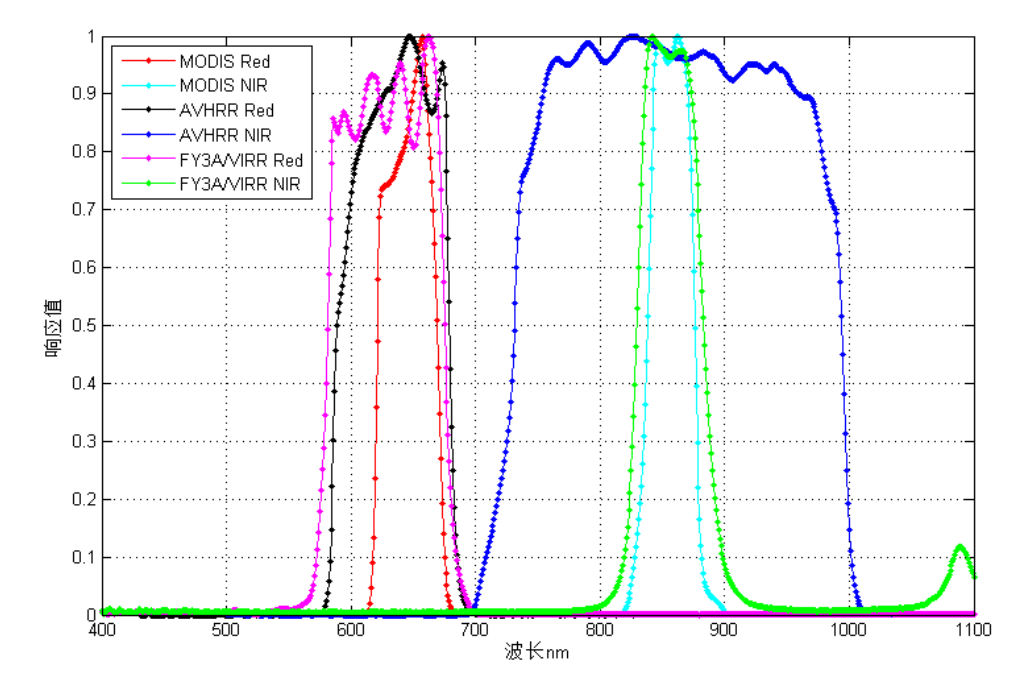


Figure 4.14: Intercomparison of the red and NIR spectral response functions (SRF) of the MODIS, AVHRR and VIRR sensors. X-axis is the wavelength in nanometers, y-axis is the responsivity.

ally, geo-locating and normalizing pixels between images is another necessary step in normalising a group of datasets.

The two sensors (MODIS and MERSI ⁴) used in this experiment have their own specific characteristics, yet the surface reflectance spectra simulated by PROSAIL were all convoluted with the same SRF, that of MODIS Aqua. This convolution converts the spectra to a single band measurement, based on the experimentally-determined responsivity of the sensor.

In effect, although the sun-target-view geometry of different sensors are considered, the same sensor characteristics were assumed between them when synthesising the red and NIR band reflectance measurements. For actual operational conditions, as done in the MuSyQ algorithm which implements CWI [22] [21] on a multi-sensoral dataset at its core, cross-calibration between the datasets of different sensors must be performed to correct for these differences. In figure 4.14 these differences are demonstrated for a different sensor aboard the same satellite as MERSI, where for example the red band of MODIS (red line) has a different spectral response to VIRR (pink line), and has a narrower effective bandwidth.

Similarly, perfect atmospheric correction was assumed. As was briefly explained in section 2.1.1, the atmosphere is the propagation medium between the surface and the sensor, and its (anisotropic) scattering and absorption properties also affect the signal measured by the sensor. This is why the top of atmosphere (TOA) reflectance measured by a sensor must be converted to a surface reflectance measurement.

Atmospheric correction introduces a dimension of variability and error propagation not directly related to surface BRDFs and their estimation, which is the focus of this research, and was therefore only briefly discussed and not accounted for. Likewise, and due to time constraints, perfect cross-calibration and geolocation was assumed, and all pseudo-observations were generated with the same SRF.

4.3.2. Simulation conditions and constraints

A design choice was made on the angular sampling to be simulated. As reported in section 2.1.1, the Ross-Li-Maignan BRDF model calculates the surface reflectance as a function of the acquisition geometry variables θ_S , θ_V and ϕ_r according to equation 2.3. If each variable were sampled at a resolution of 10° for example, and the maximum off-nadir viewing zenith angle and maximum solar zenith angle

⁴The two MODIS sensors and two MERSI sensors are aboard the Earth-orbiting satellites Terra & Aqua and FY3A & FY3B, respectively.

50 4. Results and Discussion

were constrained to $\theta_V=50^\circ$ and $\theta_S=60^\circ$, there would be 540 different possible sun-target-view geometries. Then, to consider the combinations of different observations in a sample, this number is multiplied by the sample size to get the total number of angular sampling scenarios - which must then be simulated for 6,000 surfaces and 15 cloud-contamination scenarios.

This would be computationally challenging and would generate an enormous amount of data to analyse. The choice was made to constrain the sun-target-view geometries to those of actual validation sites, as was illustrated in 4.1. A benefit of this choice was linking the numerical experiment to actual operational conditions, and being certain that the angular sampling isn't unrealistic. A more analytical approach could have been to analyse the orbital tracks of the satellites hosting the studied sensors, in order to build a database of possible sun-target-view geometries.

Furthermore, as explained in section 2.6.1, the input variables of PROSAIL can be divided into acquisition geometry variables and surface biophysical variables. The latter was varied by generating 6,000 sampling points with the aim to get an even representation of all surface types as simualted by PROSAIL. A limit of 6,000 surfaces was chosen due to the high computational cost of running the simulation system in Python (in particular the PROSAIL module).

The current results and conclusions (such as the RMSE findings in table 4.1) may change if the amount of surfaces were to be increased, or if the upper and lower limits of the input variables were extended. For example, in section 4.1.1 the Ross-Li-Maignan model was found to be a suitable approximator for the majority of terrestrial surface BRDFs. This only holds for the set of surface types defined in section 3.3, and only for the PROSAIL model's representation of these surfaces.

Therefore, the use of a different model could also affect the results of the experiment. For this experiment, FourSAIL's built-in Lambertian soil model was used, which describes the background soil's reflectance spectra as a linear combination of two wet and dry soil reflectance spectra [17][18]. Although the mixing ratio $\rho soil$ and brightness factor r_{soil} of this model were varied, a more complex soil model could have been implemented.

An extensively used alternative is the soil-leaf-canopy SLC model published in Verhoef et al. (2007) [51]. SLC uses a soil BRDF model instead of assuming the background soil to be a Lambertian scatterer, and uses a two-layer version of the canopy model SAIL, 4SAIL2. Using a (semi-)physical soil model or defining a list of soil spectra would allow for either a more comprehensive list of surfaces to be defined, or a more targeted list representative of particular surface types of interest. Berger et al. (2018) [5] provides a further review of the different canopy models developed until now.

4.3.3. General discussion on methodology

The results of this numerical experiment had been compared in sections 4.1.3, 4.2.2 and 4.2.3 to the validation of CWI performed by Zeng et al. (2016) [61], which used comparative validated satellite imagery.

The advantage of the methodology used here over using comparative satellite data, is the ability to control the simulation conditions, the noise conditions, and have a reference value with which to compare the reference too. As discussed above, the freedom allowed by a numerical experiment demands design choices to be made - some of which have may have considerable consequences. The findings presented, eventual ground validation, and the validation performed by Zeng et al. (2016) [61] are therefore not directly comparable, but complement each other. Furthermore, several assumptions were made for this experiment. However, similar experiments have also been conducted with a more indepth consideration of atmospheric effects and sensor characteristics. For example, Segl et al. (2015) [43], developed an end-to-end simulation of Sentinel-2 images, with reportedly accurate representation of the image acquisition, sensor calibration and preprocessing steps.

Due to time constraints, the focus for this reserach has been solely on surface reflectance anisotropy and BRDF estimation techniques. However, the design of the experiment can potentially accommodate more steps to make a more representative simulation. Additionally, it can easily be made applicable for other BRDF models, other sensor SRFs, with the benefit of considering a broad range of surface types.

4.4. Results and discussion - conclusion

As a first step to understanding the data produced by the numerical experiment, the suitability of the RLM BRDF model and its ability to describe a surface BRDF was analysed. It was found that the model

could be adequately fitted to the BRDF of most surfaces, converging to a narrow set of solutions. For these cases, the surface reflectance as calculated by RLM matched the samples accurately. Existing literature such as Lucht et al. (2000) [29] also supported the assertion that the RLM model is widely applicable for various surface types.

Then, a baseline scenario was considered. The BRDF parameters estimated from noise-free samples and the resulting nadir-normalised NDVI composites were presented. NDVI values generated by PROSAIL were used as a reference for the NDVI values calculated by the fitted RLM BRDF model. These were shown to have low RMSE values of around 0.01 for Chang Baishan, and 0.023 for Mongu, while no significant differences in accuracy were found between the different methods for the ideal, clear-sky scenario.

These findings were used as a baseline for the estimates from noisy samples, for each site. Comparisons with the baseline showed that in particular the isometric kernel coefficient f_{iso} was prone to being overestimated due to noise in the sample. In the case of high cloud fraction $f_c=3.0\%$, it was noted that the distribution of f_{iso_e-CWI} closely matched the baseline scenario when $\alpha=2$, with smaller differences than $f_{iso_e-LiGao}$. However, when $\alpha=5$ it was noted that the Li-Gao estimated f_{iso} had a better fit than CWI.

For the NDVI estimates, it was found that low sub-pixel contamination of $f_c = 0.5\%$ is challenging to distinguish from BRDF-related directional variations, and it's impact was not effectively suppressed by any of the methods. However, due to the low degree of contamination, this impact was also relatively small. These are summarised in table 4.1.

When the degree of contamination was high at $f_c=3.0\%$, and α was relatively low, the CWI estimates were highly accurate, and very closely matched the reference PROSAIL values. This was strongly dependent on the sample size and the value of α , as if the proportion of highly contaminated observations was too high, the CWI method's accuracy would drop significantly. For the site Mongu, with a large sample size of 13 observations, the CWI estimates RMSE of 0.022 was close and evenly slightly lower than the baseline of 0.028. Since there is no physical reason for the CWI estimate to actually be more accurate than the baseline scenario, the reduction in RMSE is assumed to be an artifact due to averaging over 6,000 surfaces.

For the site Chang Baishan, CWI failed to produce an accurate estimate at $\alpha=3$ already. The Li-Gao method then yielded a more accurate NDVI estimate with a comparatively lower RMSE. The accuracy of the Li-Gao method was found to decrease gradually as α increased. The contrast between the two performance of the two methods is caused by the different approaches to calculating the weight matrices. These are iteratively calculated and used to reduce the impact of contaminated observations in the sample.

Few experiments comparable to this research exist, and English-langauge literature on the MuSyQ and CWI algorithms is very sparse, making it challenging to corroborate the reported results. However, we were able to link the above results to the publications of the Li-Gao method Gao et al. (2002) [11] and CWI method Zeng et al. (2016) [61]. Although they used different methodologies and had different scopes, their conclusions qualitatively supported this experiment's findings on the performance of the OLS, Li-Gao, and CWI methods for estimating NDVI composites from noise-contaminated samples.

Conclusion and Recommendations

5.1. Conclusion

In this thesis, a simulation system was designed and executed to analyse the performance of the novel CWI BRDF-fitting method. With the CWI method being implemented and suggested as an improvement over the LiGao method by Zeng et al. (2016) [61], it was evaluated for its accuracy in estimating the BRDF parameters, and creating a NDVI composite. The same experiment was performed for the more conventional methods, OLS and Li-Gao.

For a composite cycle of 5 days, pseudo-observations were generated using the PROSAIL canopy radiative transfer model. These were then used to create noisy samples for different contamination scenarios, varying in number of cloudy observations α and magnitude of contamination f_c . The OLS, LiGao and CWI fitting methods were implemented to reconstruct the Ross-Li-Maignan BRDF model from noisy samples, yielding estimates of the RLM model's kernel coefficients f_{iso} , f_{vol} and f_{geo} .

The experiment was conducted for three different locations around the globe: Chang Baishan, China; Mongu, Zambia, and Harvard Forest, USA. Each site was observed with different MODIS and FY acquisition geometry due to their varying locations, as was shown in figure 4.1. Additionally, the experiment was repeated for 6,000 surface types, covering a broad range of vegetation structure and conditions, since the CWI method was designed to be used in a global MuSyQ NDVI product.

5.1.1. Concluding statements related to research questions

At the beginning of this report, three research questions were stated. These provided structure to guide the design experiment and the analysis of its results, in order to be able to comment on the performance of the novel CWI method. From the results of this experiment, which were presented and discussed in detail in chapter 4, the following conclusions were drawn and linked to each question:

Can the Ross-Li-Maignan parametric BRDF model be an accurate representation of the surface BRDF?

 For the majority of surfaces, the RLM models converge to a narrow set of solutions that described the surface BRDF well. It was also found in existing literature Lucht et al. (2000) [29] that although it is unlikely any kernel-driven parametric model could describe all possible surface BRDFs, the RLM model describes most surface types with a high accuracy.

How accurate is the nadir-normalised NDVI value, calculated using the fitted RLM model, for the noise-free scenario?

In the clear-sky case, where no noise due to cloud contamination was present in the sample, the Ross-Li-Maignan BRDF model accurately describes the surface BRDF for the vast majority of surface types. This finding was supported by the validation work performed by Zeng et al. (2016) [61], and existing literature Lucht et al. (2000) [29]. Furthermore, in these cases, no significant differences were observed between the three methods, which all performed similarly. The CWI BRDF-fitting method therefore performs accurately for the noise-free scenario.

How accurate is the CWI BRDF fitting method, as compared to the OLS and Li-Gao methods. at reconstructing the BRDF model from a sample containing cloud-contaminated observations?

- For the case of low cloud-contamination conditions ($f_c=0.05\%$), all methods failed to reduce the impact of the noisy observations, regardless of α , resulting in increased RMSE values. This impact was relatively low, however. This is due to low amounts of noise in the sample being difficult to distinguish from surface anisotropy, as also suggested by Gao et al. (2002) [11].
- CWI is very resistant to the impact of highly contaminated observations ($f_c=3.0\%$) when the ratio of contaminated to clear-sky observations is low. This ratio was sufficiently low when $\alpha<3$ for a sample size of 8 pseudo-observations (site Chang Baishan) and $\alpha<4$ for 10 observations (Harvard Forest). For the site Mongu the CWI estimates were highly accurate for all values of α tested, which was up until $\alpha=5$. For these cases the estimated NDVI composites had a very low RMSE that was approximately the same as the baseline estimate, and lower than the Li-Gao RMSE.
- Once a certain threshold of noisy observations was passed, the accuracy of the CWI method was noted to drop off rapidly, with the RMSE of the estimate increasing approximately ten-fold after the addition of one contaminated observation. For these scenarios/sites with a higher proportion of noisy observations, the NDVI value as estimated by LiGao is more accurate than CWI. The CWI method relies on the a posteriori calculated observation error to reduce the weights of suspected outliers. When this calculation is erroneous, the CWI method assigns non-negligible weights to the contaminated observations in the sample and the accuracy of the estimates are significantly reduced.

In conclusion, this numerical experiment has confirmed that the CWI method is effective at reducing the impact of noisy observations on the RLM BRDF model reconstruction, given a sufficiently large sample size, and a high contamination level that can be successfully corrected by the algorithm. In these cases, the weights of these contaminated observations are reduced to nearly 0, so that the RLM BRDF model is fitted to only the remaining, noise-free observations. This results in an estimate of the BRDF parameters that closely match the ideal, noise-free case. The conventional Li-Gao method performs worse than CWI in these scenarios, as it assigns non-negligible weights to the contaminated observations in the sample, whereas the OLS method performs worse than both methods in virtually all regards.

However, when there are too many contaminated observations in the sample, the CWI method can yield significantly inaccurate BRDF estimates and NDVI composite estimates, with a higher RMSE than the Li-Gao method. The findings suggest that the CWI method is prone to a sudden drop-off in accuracy under worsening noise conditions, while the accuracy of the estimates calculated from the Li-Gao method decrease more gradually. In virtually all cases, both methods outperform OLS, likely due to it assuming Gaussian noise, whereas noise due to undetected clouds is negatively biased in the NDVI [61].

5.1.2. Final thoughts

Although the MuSyQ algorithm [21] chooses to use the CWI algorithm when 5 or more valid, clear-sky observations are available, the results of the simulation might suggest that a more conservative threshold should be chosen under operational conditions. If pre-screening and/or cloud mask failures lead to detect too many highly-contaminated observations, the CWI estimate would be significantly impacted.

Parametric linear kernel-driven models are favourable due to their high-calculation speed, and are therefore frequently used in the production of satellite products. A single MODIS image tile ¹ contains approximately 5,760,000 pixels covering an area of 1,200 by 1,200 kilometers - and the surface BRDF for each pixel must be estimated. If this high rate of production required to create daily global coverage is to be maintained while simultaneously increasing its accuracy, improvements on BRDF-fitting methods such as CWI are of crucial importance.

¹Considering the MOD09GA global daily surface reflectance product at a resolution of 500m as an example. See https://lpdaac.usgs.gov/products/mod09gav006/ for details on this satellite product.

5.1. Conclusion 55

As a newly proposed BRDF-fitting method, the Changing-Weight Iterative method showed promising results. Increasing the coverage and accuracy with which we monitor the Earth's is paramount to mapping out and mitigating the effects of climate change. Therefore studying and validating such new methods is a necessary, continuous process, furthering the field of terrestrial remote sensing step by step. And with each small step, the picture becomes just a little bit sharper.

5.2. Recommendations

The findings of this thesis, and the method designed to create them, may prove to be a basis for further research on CWI and its applications. Additionally, it may be of interest to improve certain aspects of the methodology, as has already been briefly discussed in section 4.3.3.

From the results and discussion presented in this report, the following recommendations for future work are made:

Developing an improved quality flag

When the MuSyQ algorithm is used to produce a NDVI product by implementing CWI, it assigns quality flags to each resulting estimate. These are detailed in the MuSyQ ATBD v1.0 [21], and are performed on a per pixel basis.

Determination of this quality flag is based on input data quality, weather, BRDF inversion method (CWI is the main algorithm) and other factors that affect the quality of the composite.

With further development, this numerical experiment could be used to define a confidence interval for the quality of the estimated NDVI composite. As was reported, there appears to be a 'tipping point' after which the CWI method's accuracy to drastically fail.

With further study, a relationship betwen this point and the spread of the angular sampling could be explored. For example, if two observations are clustered very close together in angular space, it's hypothetically possible that CWI is then more likely to detect if one of the two is contaminated.

The risk of of CWI failing could be incorporated in the determination of the product's quality flag, perhaps as a function of sample size and some factor that describes how widely the observations are spread out within the sample. This information could also be appended as an additional flag or confidence indicator.

Numerical experiment with SLC model

The canopy model chosen for this experiment, PROSAIL, is especially suited for simulating homogeneous vegetation canopies [18]. Therefore this study's results hold primarily for the surface types simulated under this assumption, as well as other assumptions made by the PROSAIL model.

An alternative research project could be to repeat the numerical experiment using the soil-leaf-canopy (SLC) model to simulate canopies instead. As was briefly discussed in section 4.3, one of the major differences of SLC is the use of a more advanced soil BRDF model. Another is that SLC is one of the few canopy models that models clumping, which is the clustering of canopy foliages [51].

These two differences have implications on the modeling of the surface BRDF, essentially simulating different surfaces compared to this experiment. However, the methodology of this experiment could be maintained, except that the sampling of SLC's parameter space must be carefully designed to create a set of surfaces. Further research using SLC would lead to interesting results, and perhaps be more globally representative of the surface types on Earth.

Relating results to other vegetation parameters

Another possible research topic is to link the NDVI estimation errors to variables that are derived from NDVI. Various relationship exist to calculate for example Leaf Area Index (LAI) from NDVI measurements. From Zhou et al. (2017) [63], one such empirical relationship for rice crops is equation 5.1.

$$LAI = 0.361 \cdot e^{3.69NDVI} \tag{5.1}$$

In this case an error in the NDVI estimate would lead to a propagated error in the LAI estimate. This could be further investigated and quantified, for other LAI-NDVI relationships as well.

Furthermore, there also exists room for interesting research into the estimation of vegetation parameters from a BRDF model. This thesis has focused on NDVI composites calculated from an estimated BRDF model, but the RLM BRDF parameters can also be used on their own to estimate LAI, among other vegetation parameters.

An additional topic could therefore be to quantify the relevance of a more accurate BRDF estimate on its derived vegetation parameters. Two potentially useful papers are "Leaf Area Index Estimates Using Remotely Sensed Data and BRDF Models in a Semiarid Region" by Qi et al. (2017) [38], and "Potentials and limits of vegetation indices for LAI and APAR assessment" by Baret et al. 1991 [9].

Appendices



PROSAIL input variables

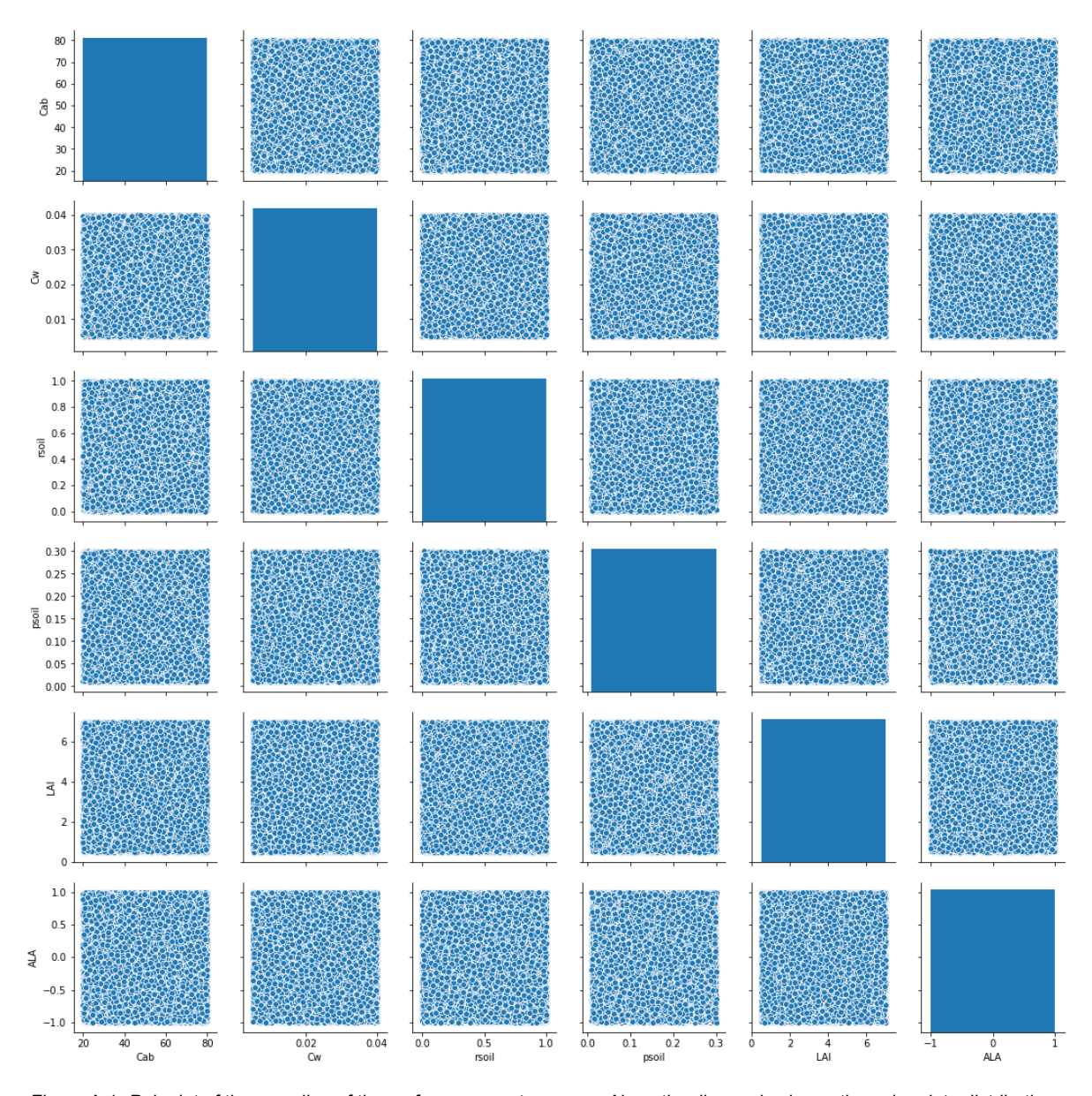


Figure A.1: Pair plot of the sampling of the surface parameter space. Along the diagonal axis are the uni-variate distributions (i.e. histograms) of individual variables, and along the horizontal and vertical axes are the joint distribution density functions (JDDFs) per variable pair.

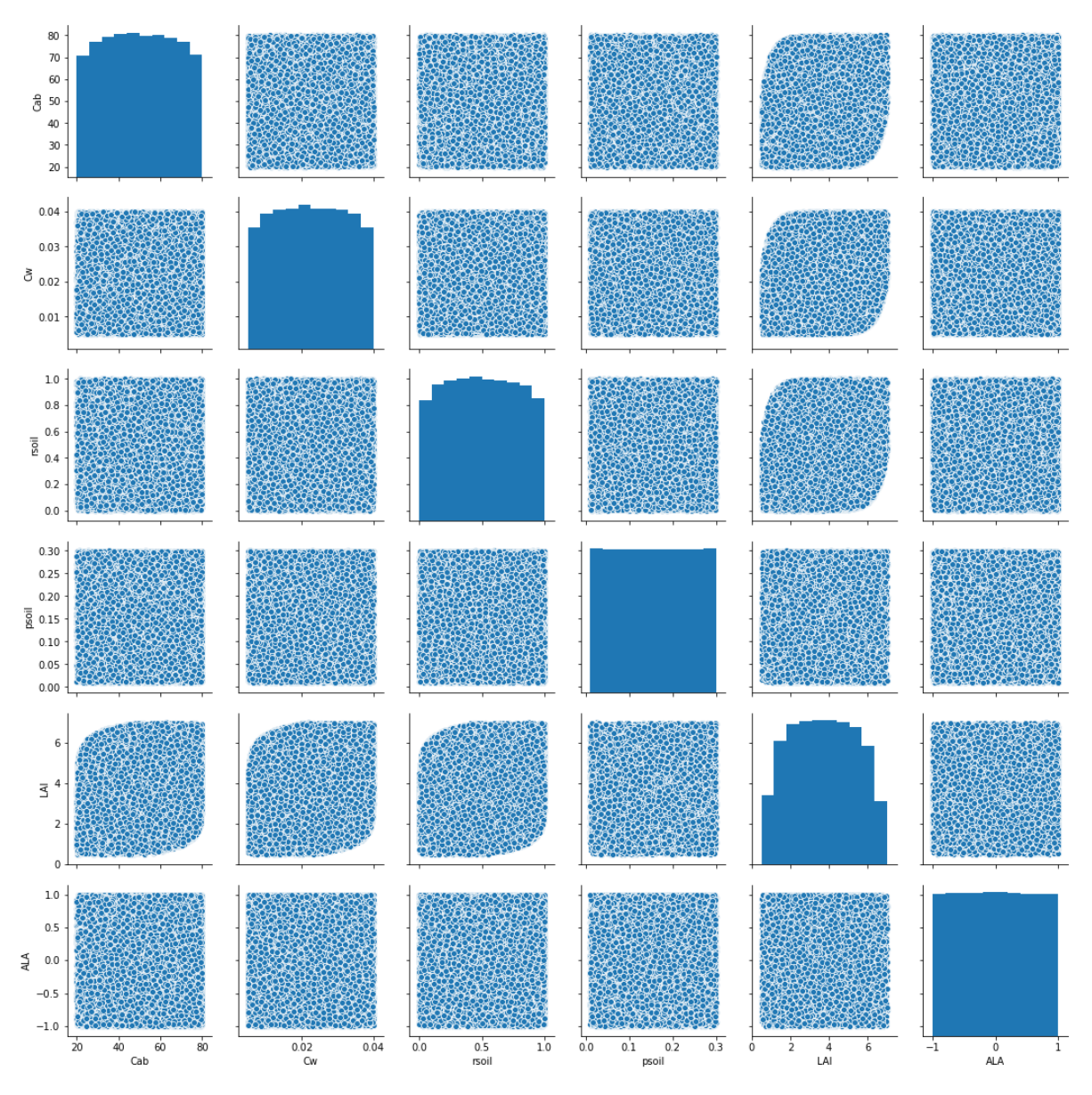


Figure A.2: 'Trimmed' pair plot of the sampling of the surface parameter space. Unrealistics pairings of variables were removed according to the methodology section 3.3.1.



Variance of RLM model parameters

Variance of RLM model estimates per surface - red band

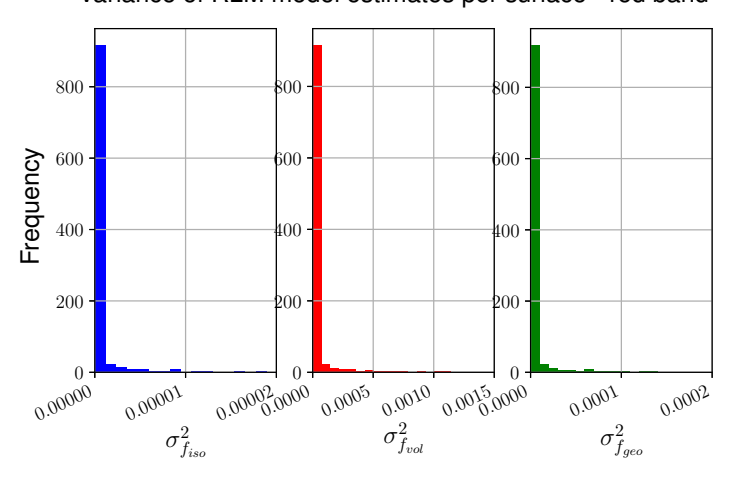
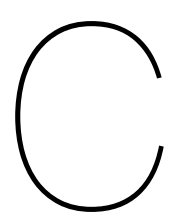


Figure B.1: Variance of the possible RLM model parameter estimates for each surface, for a subset of 1000 randomly selected surfaces. Red band, study site Harvard Forest.



Comparison of estimated nadir-normalised NDVI to reference - noisefree case

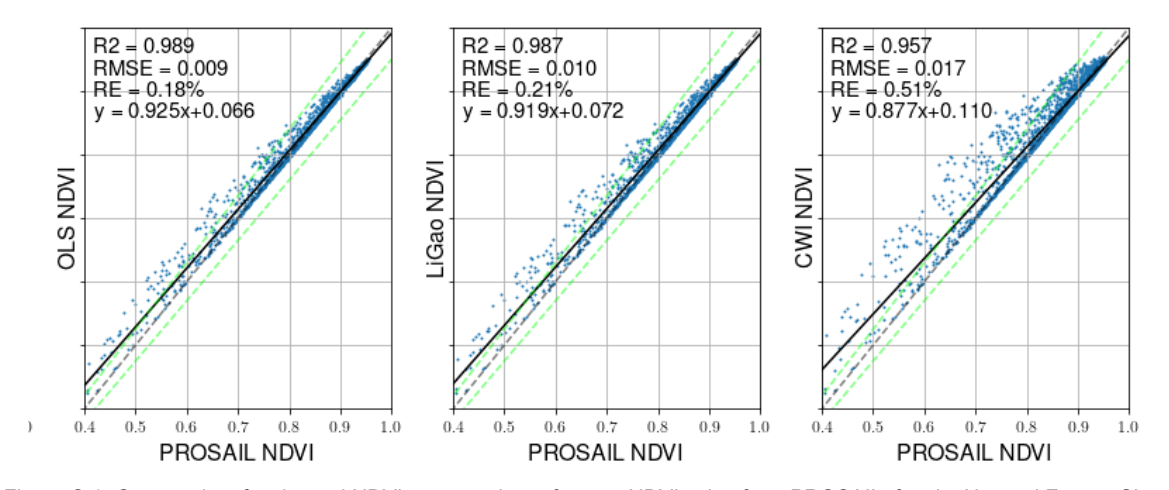


Figure C.1: Scatter plot of estimated NDVI compared to reference NDVI value from PROSAIL, for site Harvard Forest. Shown here are NDVI values calculated using BRDF parameters estimated from noise-free samples using OLS, Li-Gao, and CWI methods. Dotted line is 1:1 line, green lines are $\pm 5\%$.

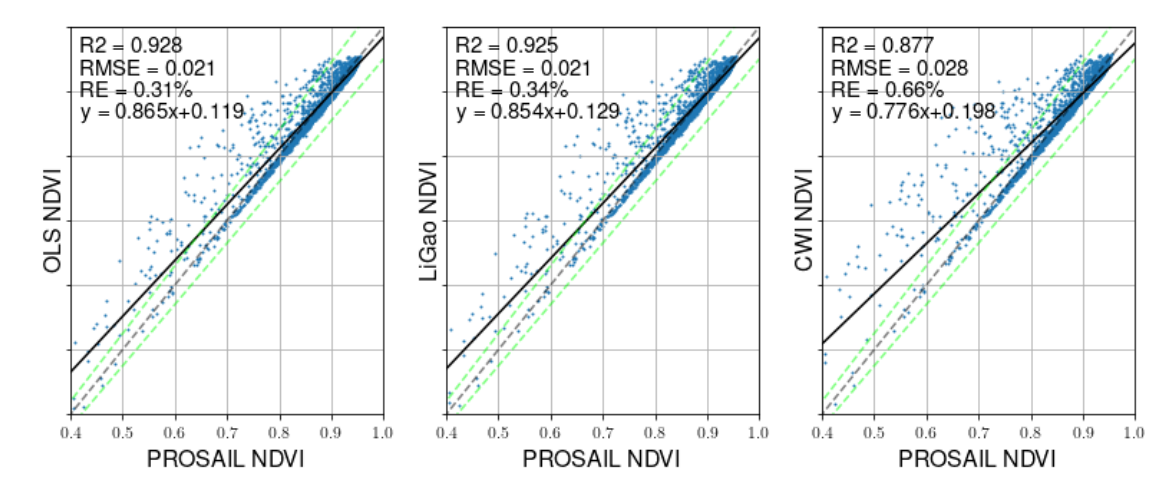
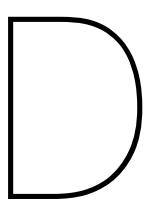


Figure C.2: Scatter plot of estimated NDVI compared to reference NDVI value from PROSAIL, for site Harvard Forest. Shown here are NDVI values calculated using BRDF parameters estimated from noise-free samples using OLS, Li-Gao, and CWI methods. Dotted line is 1:1 line, green lines are $\pm 5\%$.



BRDF parameters estimates

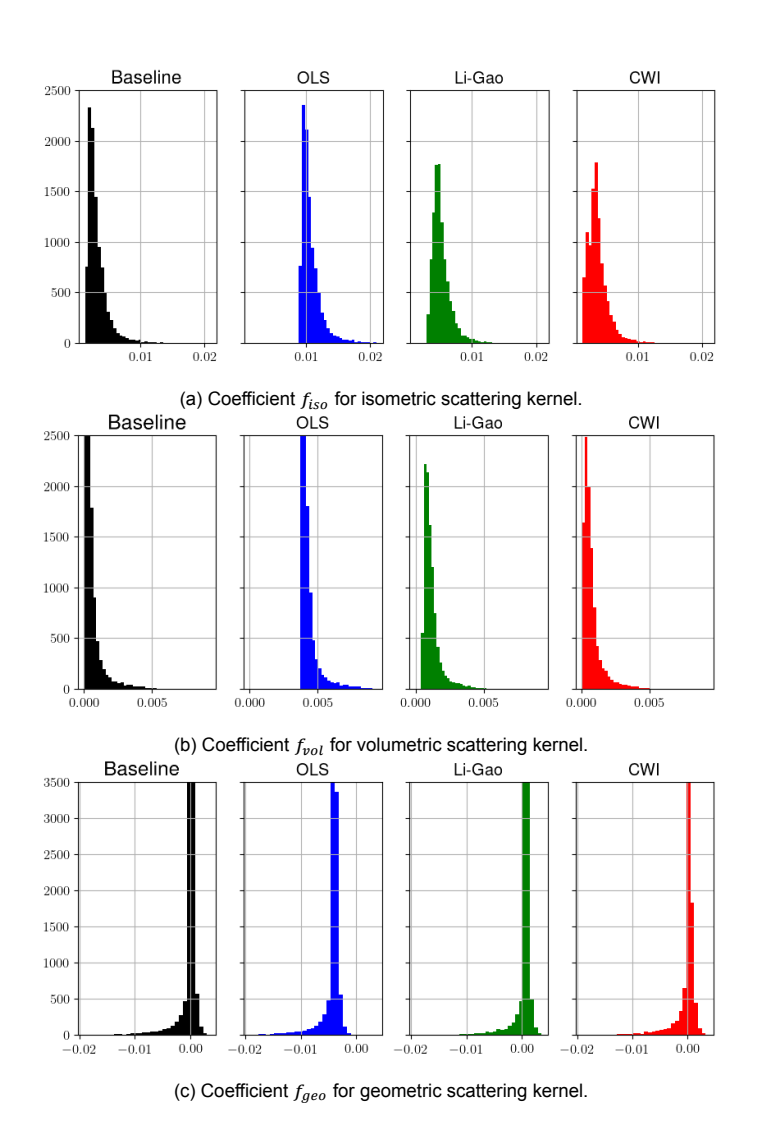
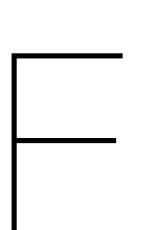


Figure D.1: Distribution of estimated red band BRDF parameters, for site Harvard Forest. Left-most histogram is the baseline distribution of parameters from the noise-free sample, and the remaining histograms are estimates for the scenario of (α = 2, f_c = 1.5%), with a total sample size of 10 observations. Angular spread of the 10 observations used for the BRDF fitting can be seen in 4.1b.



Comparison of estimated nadir-normalised NDVI to reference - Low cloud contamination

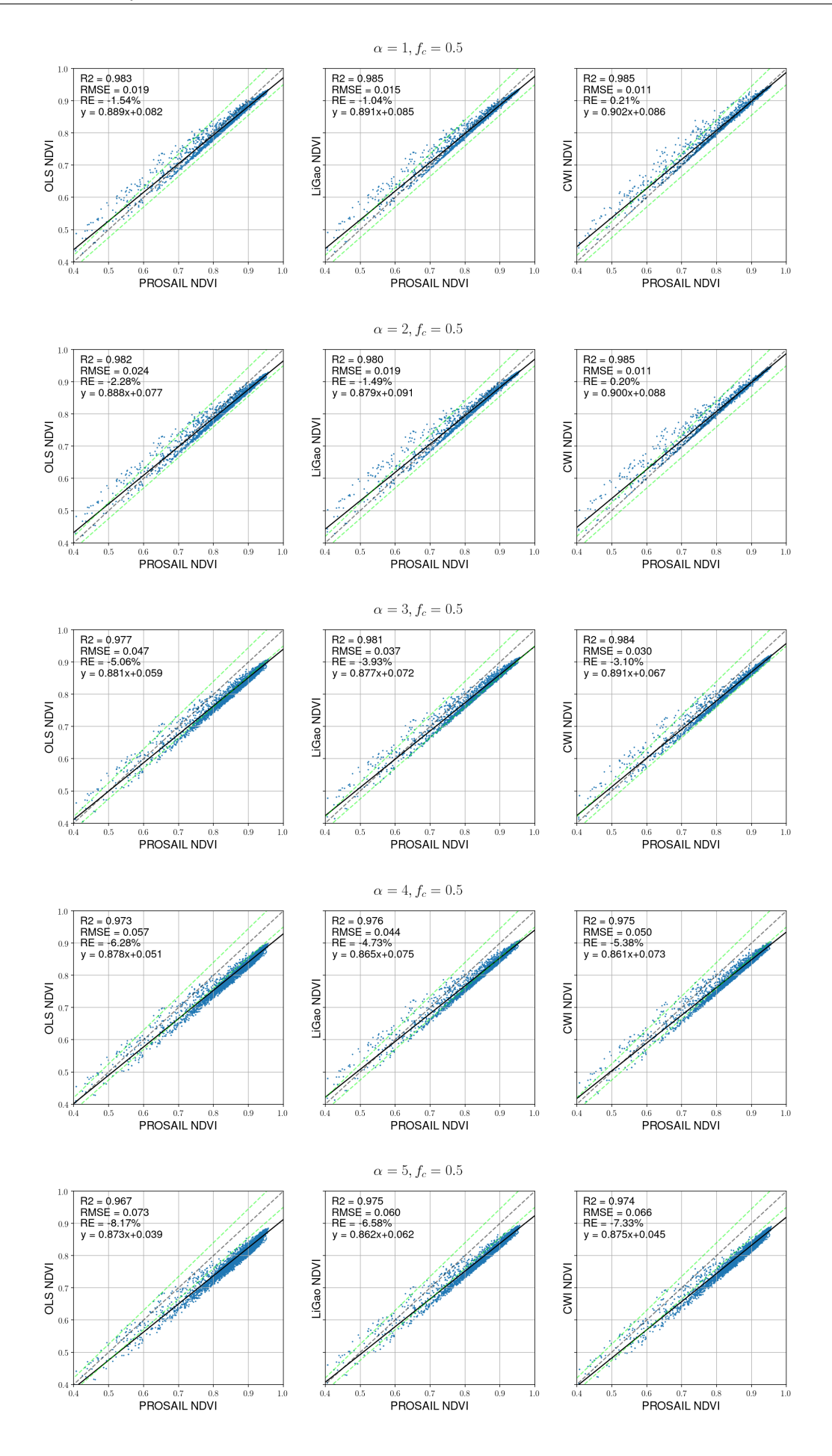


Figure E.1: Estimated nadir-normalised NDVI versus reference PROSAIL values for study site Harvard Forest, for sun-target-view geometry see fig.4.1b.

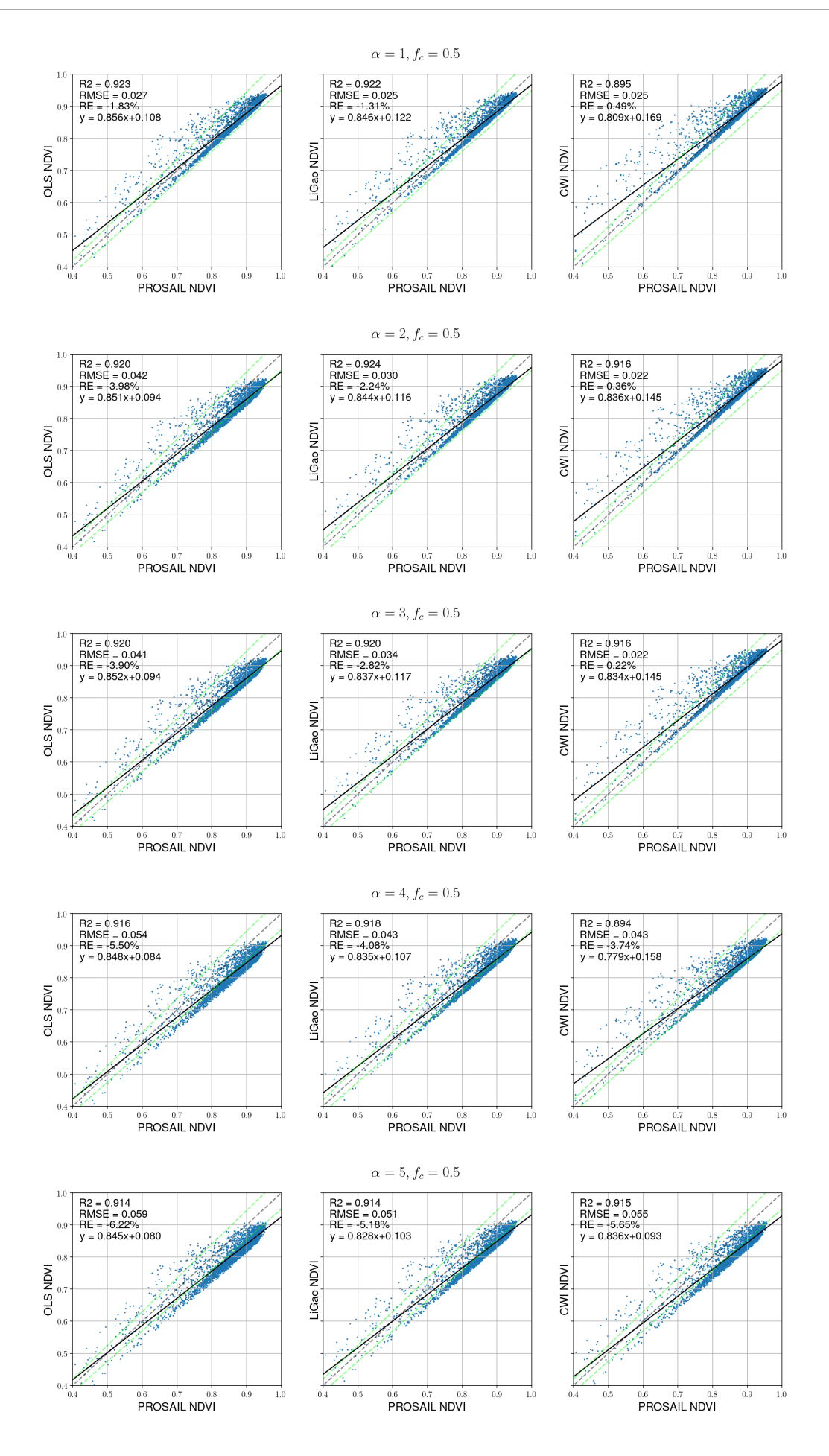


Figure E.2: Estimated nadir-normalised NDVI versus reference PROSAIL values for study site Mongu, for sun-target-view geometry see fig.4.1c.

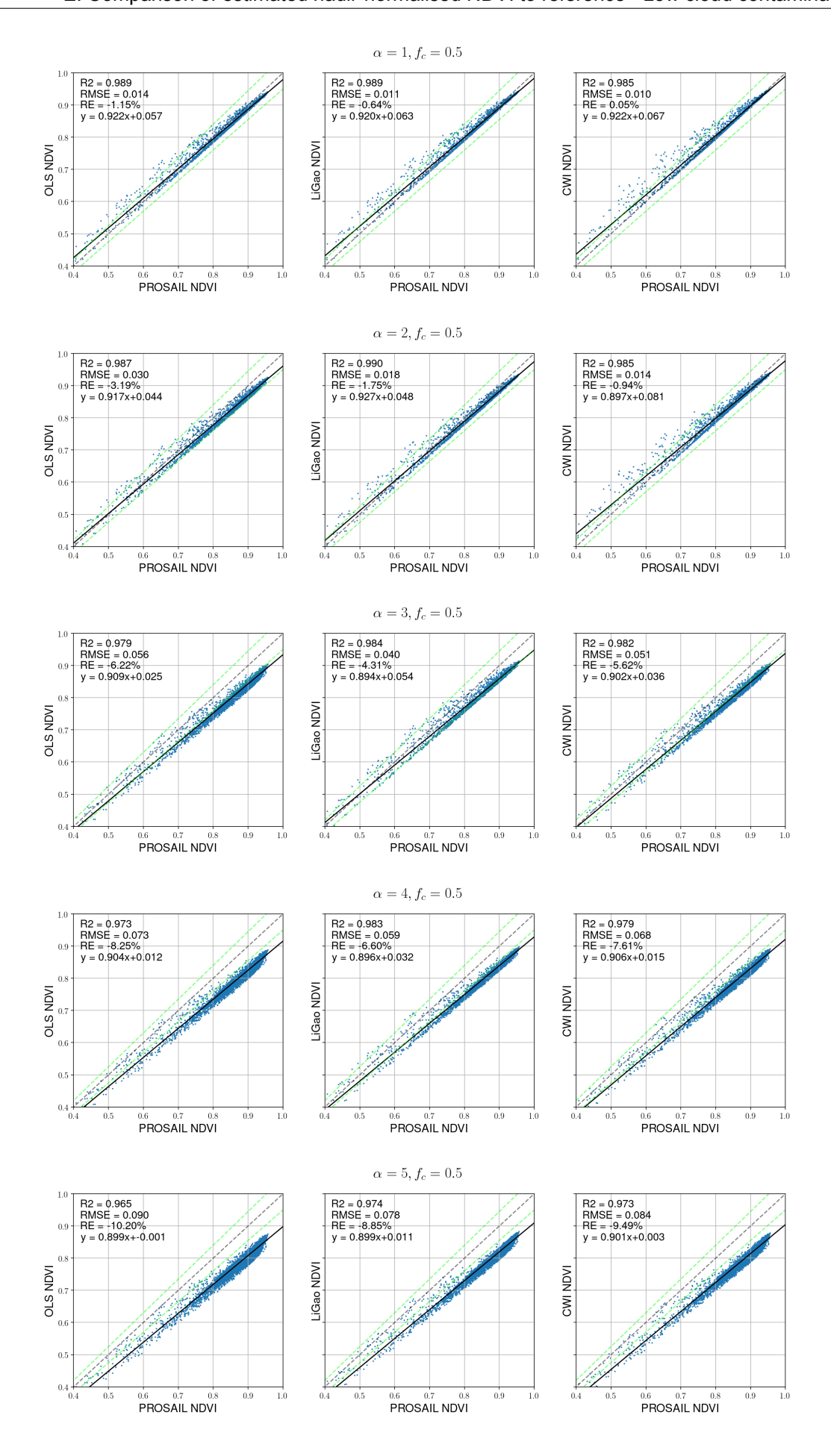


Figure E.3: Estimated nadir-normalised NDVI versus reference PROSAIL values for study site Chang Baishan, for sun-target-view geometry see fig.4.1a.



Comparison of estimated nadir-normalised NDVI to reference - Medium cloud contamination

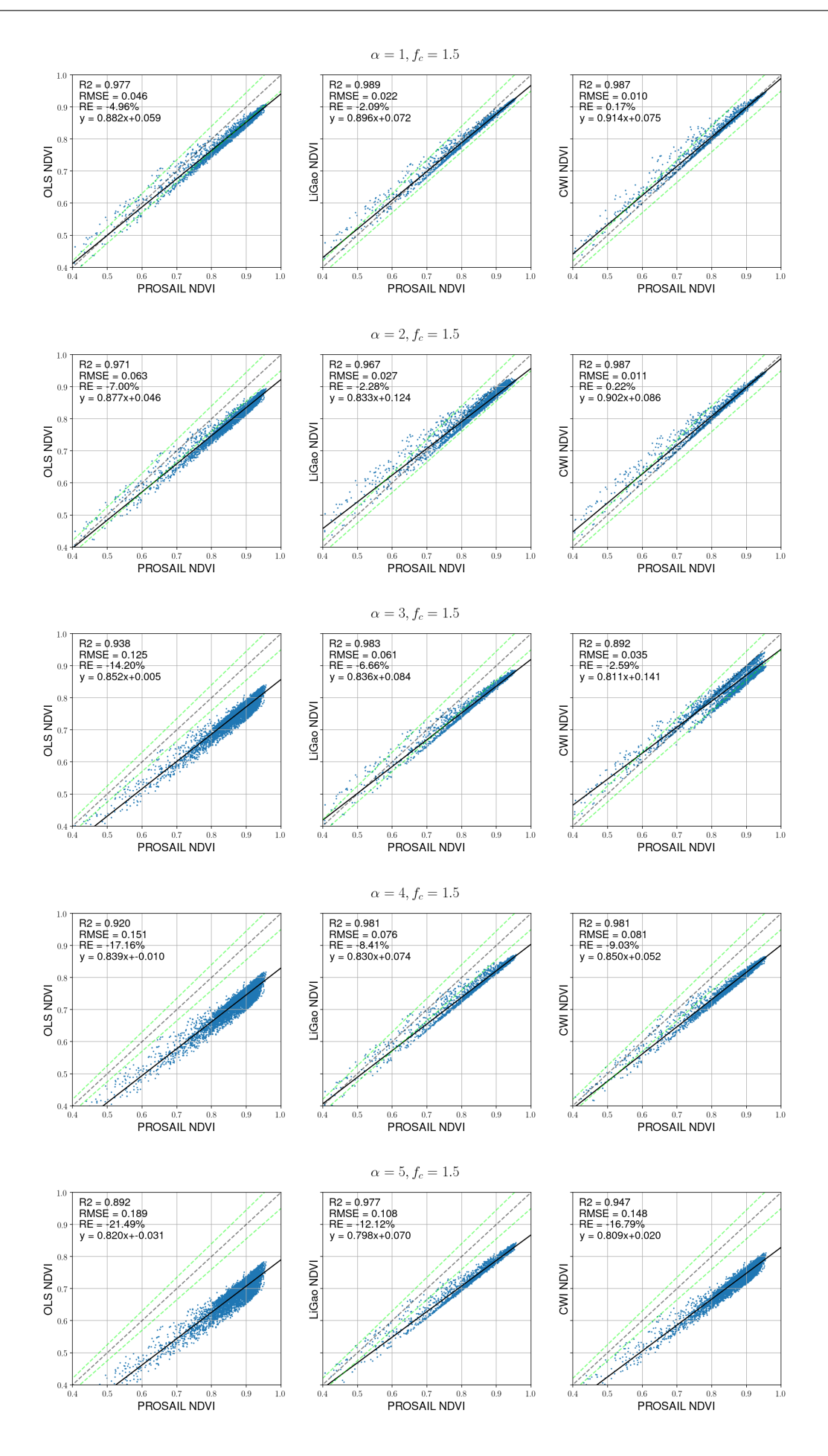


Figure F.1: Estimated nadir-normalised NDVI versus reference PROSAIL values for study site Harvard Forest, for sun-target-view geometry see fig.4.1b.

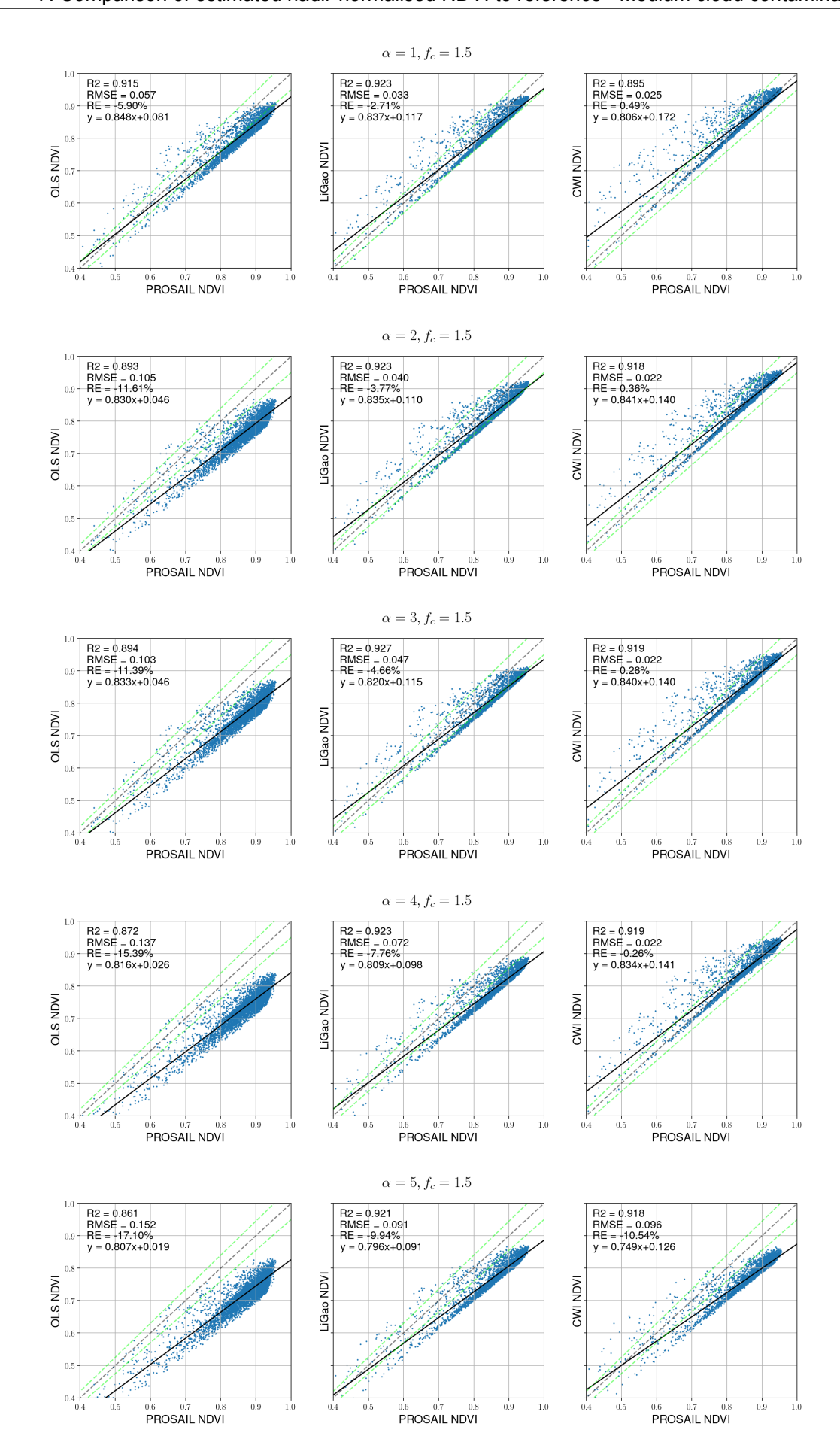


Figure F.2: Estimated nadir-normalised NDVI versus reference PROSAIL values for study site Mongu, for sun-target-view geometry see fig.4.1c.

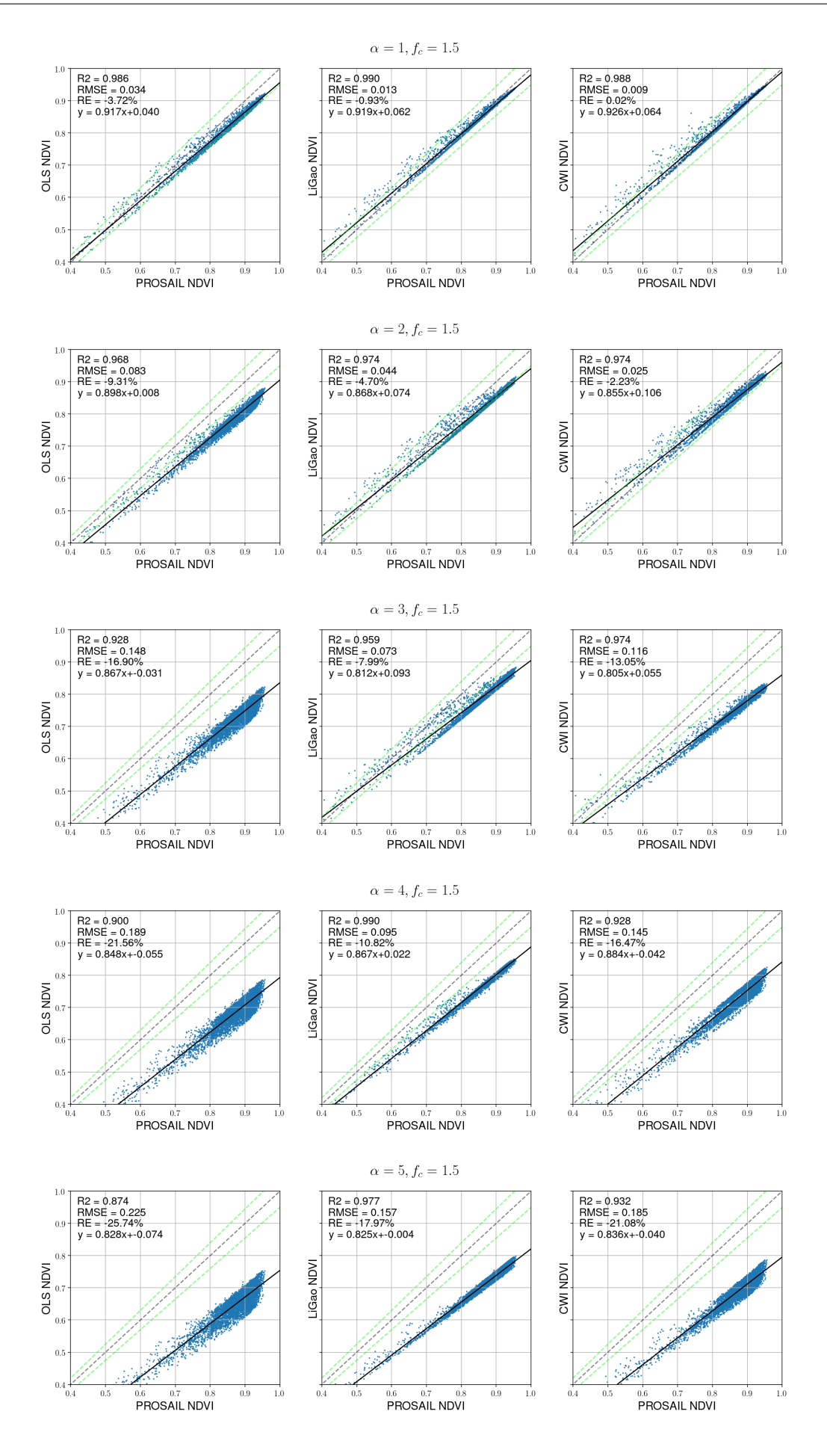


Figure F.3: Estimated nadir-normalised NDVI versus reference PROSAIL values for study site Chang Baishan, for sun-target-view geometry see fig.4.1a.

Comparison of estimated nadir-normalised NDVI to reference - High cloud contamination

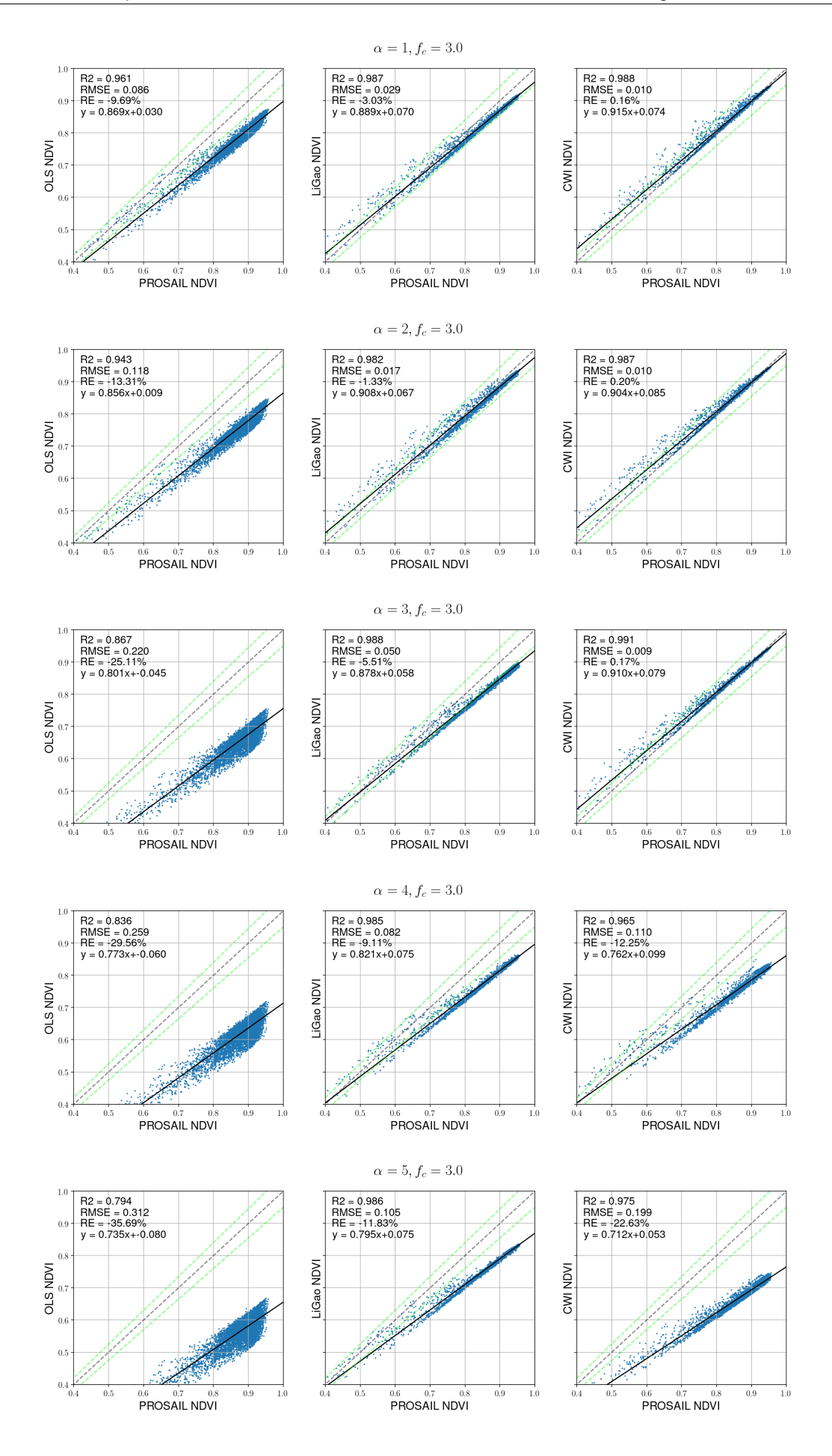


Figure G.1: Estimated nadir-normalised NDVI versus reference PROSAIL values for study site Harvard Forest, for sun-target-view geometry see fig.4.1b.

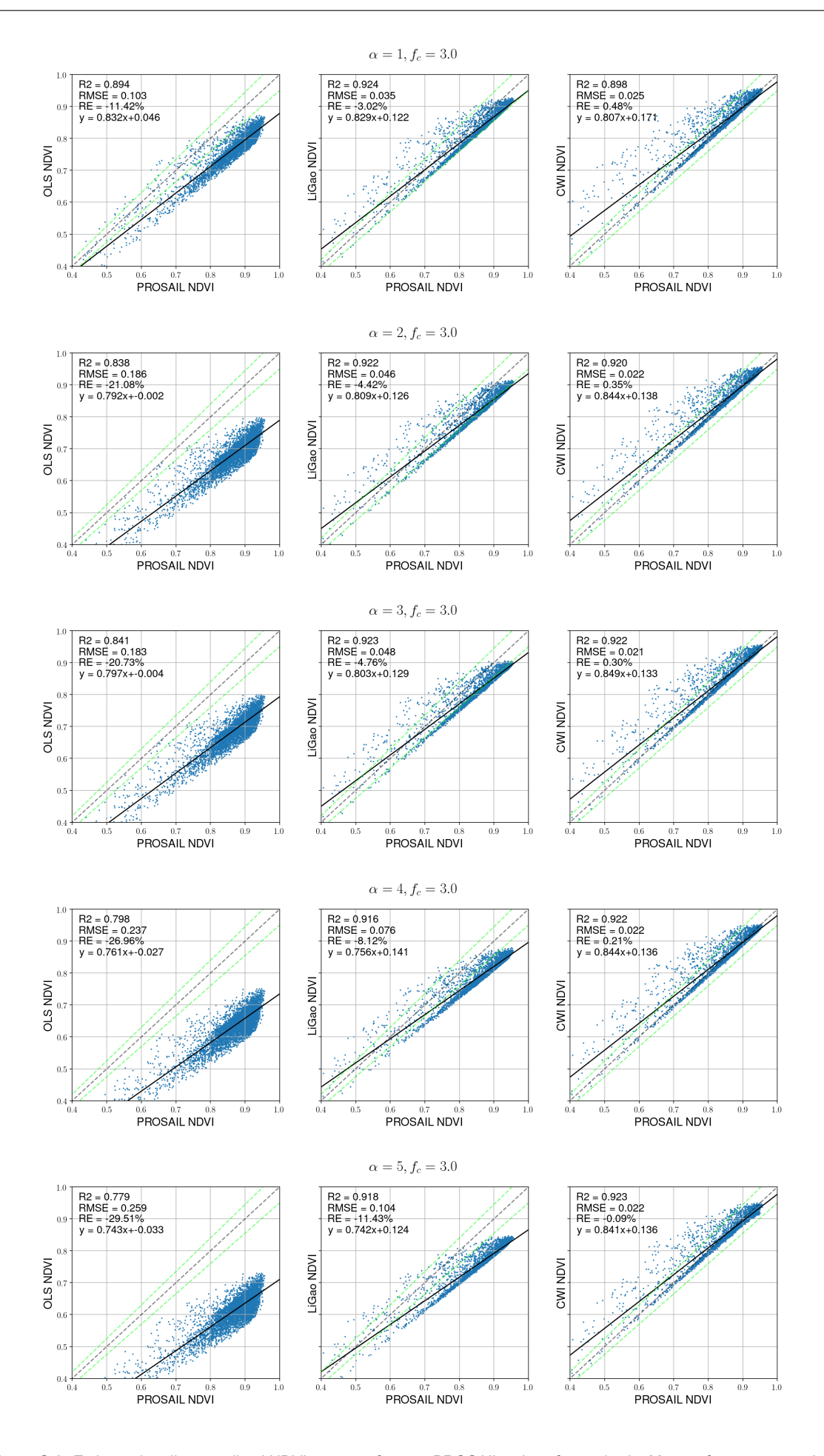


Figure G.2: Estimated nadir-normalised NDVI versus reference PROSAIL values for study site Mongu, for sun-target-view geometry see fig.4.1c.

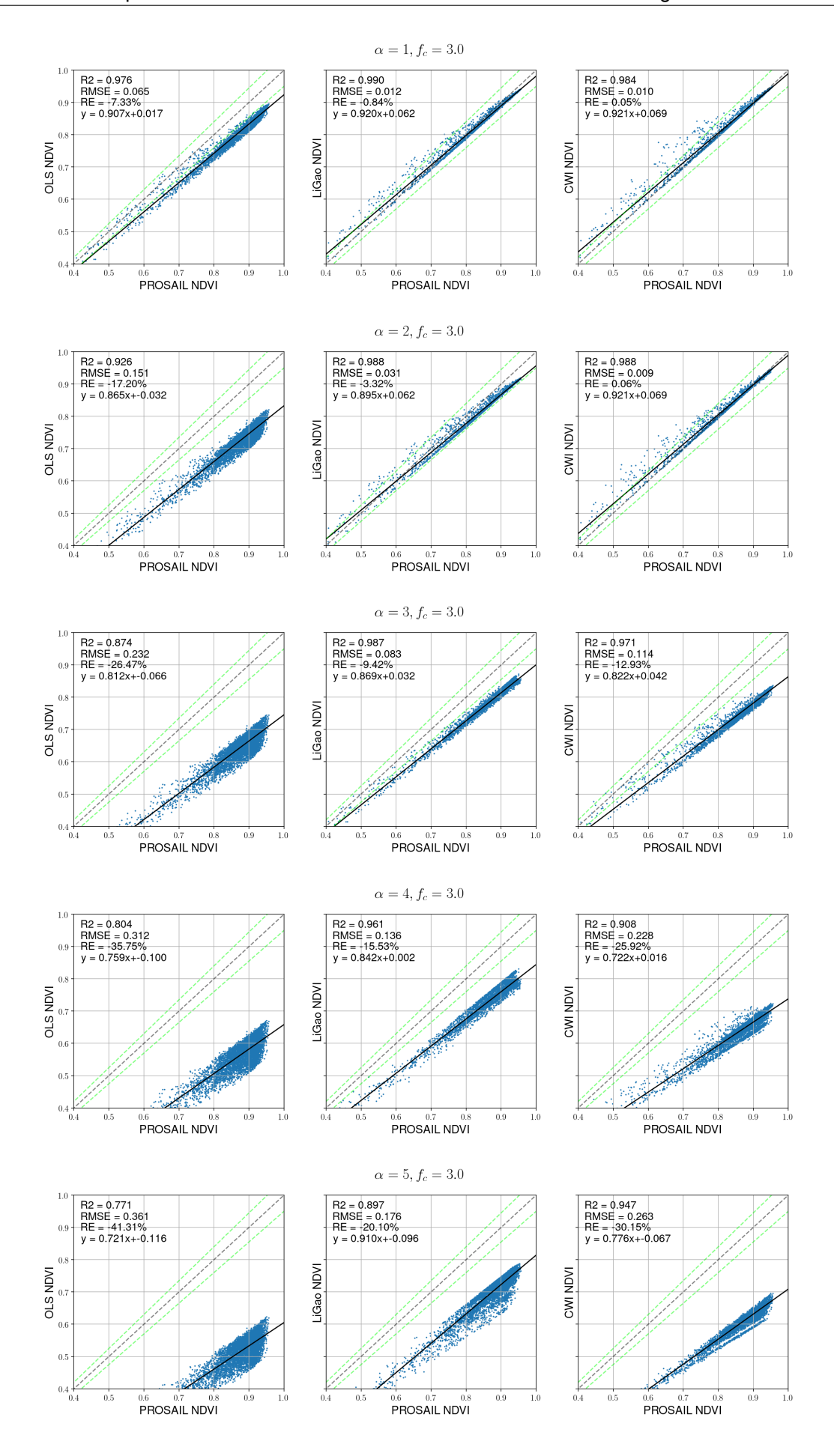


Figure G.3: Estimated nadir-normalised NDVI versus reference PROSAIL values for study site Chang Baishan, for sun-target-view geometry see fig.4.1a.



Tables of RMSE analysis results

Table H.1: Mean error for each scenario, quantified by the RMSE using PROSAIL as a reference value. Summarized here for α from 1 to 5 for the case of low cloud contamination $f_c=0.5\%$, which results in a mean relative NDVI noise of 15.5% in the contaminated observations. Greener boxes indicate lower RMSE value, and red indicates higher. Note: all tables are standardised to the same scale of RMSE-color.

	Number of contaminated observations					
Estimation method	<i>α</i> = 0	<i>α</i> = 1	<i>α</i> = 2	<i>α</i> = 3	α = 4	<i>α</i> = 5
	Chang Baishan					
OLS	0,009	0,014	0,03	0,056	0,073	0,09
Li-Gao	0,01	0,011	0,018	0,04	0,059	0,078
CWI	0,017	0,01	0,014	0,051	0,068	0,084
	Harvard					
OLS	0,012	0,012	0,024	0,047	0,057	0,073
Li-Gao	0,013	0,015	0,019	0,037	0,044	0,06
CWI	0,014	0,011	0,011	0,03	0,05	0,066
	Mongu					
OLS	0,021	0,027	0,042	0,041	0,054	0,059
Li-Gao	0,021	0,025	0,03	0,034	0,043	0,051
CWI	0,028	0,025	0,022	0,022	0,043	0,055

Table H.2: Mean error for each scenario, quantified by the RMSE using PROSAIL as a reference value. Summarized here for α from 1 to 5 for the case of low cloud contamination $f_c=1.5\%$, which results in a mean relative NDVI noise of 35.8% in the contaminated observations. Greener boxes indicate lower RMSE value, and red indicates higher. Note: all tables are standardised to the same scale of RMSE-color.

	Number of contaminated observations					
Estimation method	α = 0	α = 1	<i>α</i> = 2	α = 3	α = 4	<i>α</i> = 5
	Chang Baishan					
OLS	0,009	0,034	0,083	0,148	0,189	0,225
Li-Gao	0,01	0,013	0,044	0,073	0,095	0,157
CWI	0,017	0,009	0,025	0,116	0,145	0,185
	Harvard					
OLS	0,012	0,046	0,063	0,125	0,151	0,189
Li-Gao	0,013	0,022	0,027	0,061	0,076	0,108
CWI	0,014	0,01	0,011	0,035	0,081	0,148
	Mongu					
OLS	0,021	0,057	0,105	0,103	0,137	0,152
Li-Gao	0,021	0,033	0,04	0,047	0,072	0,091
CWI	0,028	0,025	0,022	0,022	0,022	0,096

Table H.3: Mean error for each scenario, quantified by the RMSE using PROSAIL as a reference value. Summarized here for α from 1 to 5 for the case of low cloud contamination $f_c=3.0\%$, which results in a mean relative NDVI noise of 53.2% in the contaminated observations. Greener boxes indicate lower RMSE value, and red indicates higher. Note: all tables are standardised to the same scale of RMSE-color.

_	Number of contaminated observations					
Estimation method	<i>α</i> = 0	<i>α</i> = 1	<i>α</i> = 2	<i>α</i> = 3	α = 4	<i>α</i> = 5
	Chang Baishan					
OLS	0,009	0,065	0,151	0,232	0,312	0,361
Li-Gao	0,01	0,012	0,031	0,083	0,136	0,176
CWI	0,017	0,01	0,009	0,114	0,228	0,263
	Harvard					
OLS	0,012	0,086	0,118	0,22	0,259	0,312
Li-Gao	0,013	0,029	0,017	0,05	0,082	0,105
CWI	0,014	0,01	0,01	0,009	0,11	0,199
	Mongu					
OLS	0,021	0,103	0,186	0,183	0,237	0,259
Li-Gao	0,021	0,035	0,046	0,048	0,076	0,104
CWI	0,028	0,025	0,022	0,021	0,022	0,022

- [1] Remote Sensors. https://earthdata.nasa.gov/learn/remote-sensors. [Online; accessed: 2020-03-02].
- [2] F. Achard et al. Use of satellite remote sensing in LULUCF sector. GOFC-GOLD Report, 33, 2008.
- [3] A. Agapiou et al. The importance of accounting for atmospheric effects in the application of NDVI and interpretation of satellite imagery supporting archaeological research: The Case Studies of Palaepaphos and Nea Paphos Sites in Cyprus. *Remote Sensing*, 3(12):2605–2629, 2011.
- [4] B. Aosier, M. Kaneko, and M. Takada. Comparison of NDVI of ground measurement, atmospheric corrected ASTER L1B data and ASTER surface reflectance product (AST07) data. In 2007 IEEE International Geoscience and Remote Sensing Symposium, pages 1806–1811, 2007.
- [5] K. Berger, C. Atzberger, et al. Evaluation of the PROSAIL model capabilities for future hyperspectral model environments: A review study. *Remote Sensing*, 10(1), 2018.
- [6] Z. Cai et al. Performance of smoothing methods for reconstructing NDVI time-series and estimating vegetation phenology from MODIS data. *Remote Sensing*, 9(12), 2017.
- [7] J. Chimot. Global mapping of atmospheric composition from space Retrieving aerosol height and tropospheric NO2 from OMI. PhD thesis, 07 2018.
- [8] T. Cooley et al. FLAASH, a MODTRAN4-based atmospheric correction algorithm, its application and validation. In *IEEE International Geoscience and Remote Sensing Symposium*, volume 3, pages 1414–1418 vol.3, 2002.
- [9] B. Frederic and G. Guyot. Potential and limitations of vegetation indices for LAI and APAR assessment. *Remote Sensing of Environment*, 104:88–95, 01 1991.
- [10] R.A. Frey et al. Cloud detection with MODIS. part i: Improvements in the MODIS cloud mask for collection 5. *Journal of Atmospheric and Oceanic Technology*, 25(7):1057–1072, 2008.
- [11] F. Gao, Y. Jin, C.B. Schaaf, et al. Bidirectional NDVI and atmospherically resistant BRDF inversion for vegetation canopy. *IEEE Transactions on Geoscience and Remote Sensing*, 40(6):1269–1278, 2002.
- [12] J.N. Hird and G.J. McDermid. Noise reduction of NDVI time series: An empirical comparison of selected techniques. *Remote Sensing of Environment*, 113(1):248 258, 2009.
- [13] B Hosgood, S Jacquemoud, G Andreoli, et al. The JRC leaf optical properties experiment (LOPEX'93). Eur. Commiss., Directorate—General XIII, Telecommun, Inf, Market and Exploitation of Res., L-2920, Belgium, CL-NA-16095-EN-C, 1994.
- [14] S. Jacquemoud. Inversion of the PROSPECT + SAIL canopy reflectance model from AVIRIS equivalent spectra: Theoretical study. Remote Sensing of Environment, 44(2):281 – 292, 1993. Airbone Imaging Spectrometry.
- [15] S. Jacquemoud and F. Baret. PROSPECT: A model of leaf optical properties spectra. *Remote sensing of environment*, 34(2):75–91, 1990.
- [16] S. Jacquemoud et al. Comparison of four radiative transfer models to simulate plant canopies reflectance: Direct and inverse mode. *Remote Sensing of Environment*, 74(3):471–481, 2000.
- [17] S. Jacquemoud et al. PROSPECT+ SAIL: 15 years of use for land surface characterization. In 2006 IEEE International Symposium on Geoscience and Remote Sensing, pages 1992–1995. IEEE, 2006.

[18] S. Jacquemoud et al. PROSPECT+ SAIL models: A review of use for vegetation characterization. *Remote sensing of environment*, 113:S56–S66, 2009.

- [19] J.R. Jensen and S.R. Schill. Bidirectional Reflectance Distribution Function (BRDF) characteristics of smooth cordgrass (spartina alterniflora) obtained using a Sandmeier field goniometer. *Geocarto International*, 15(2):23–30, 2000.
- [20] Yufang Jin, Feng Gao, Crystal Schaaf, Xiaowen Li, Alan H. Strahler, Carol J. Bruegge, and John V. Martonchik. Improving MODIS surface BRDF/albedo retrieval with MISR multiangle observations. IEEE Trans. Geoscience and Remote Sensing, 40:1593–1604, 2002.
- [21] L. Jing. 1km composited vegetation index product algorithm theoretical basis document. Chinese language, unpublished.
- [22] L. Jing, Y. Zeng, and Q. Liu. 1 km/5 day NDVI data product over China-ASEAN (2013). *Journal of Global Change Data & Discovery*, 1(3):268–277, 03 2017.
- [23] Y.J. Kaufman. The effect of subpixel clouds on remote sensing. *International Journal of Remote Sensing*, 8(6):839–857, 1987.
- [24] M.D. King et al. Spatial and temporal distribution of clouds observed by MODIS onboard the Terra and Aqua satellites. *IEEE Transactions on Geoscience and Remote Sensing*, 51(7):3826–3852, July 2013.
- [25] A. Kuusk. The Hot Spot Effect in Plant Canopy Reflectance, pages 139–159. Springer Berlin Heidelberg, Berlin, Heidelberg, 1991.
- [26] S.G. Leblanc, J.M. Chen, and J. Cihlar. NDVI directionality in boreal forests: A model interpretation of measurements. *Canadian Journal of Remote Sensing*, 23(4):369–380, 1997.
- [27] R. Liu et al. Global evaluation of gap-filling approaches for seasonal NDVI with considering vegetation growth trajectory, protection of key point, noise resistance and curve stability. Remote Sensing of Environment, 189:164 – 179, 2017.
- [28] A. Lorente, K.F. Boersma, P. Stammes, et al. The importance of surface reflectance anisotropy for cloud and NO2 retrievals from GOME-2 and OMI. Atmospheric Measurement Techniques, 11 (7):4509–4529, 7 2018.
- [29] W. Lucht and J.L. Roujean. Considerations in the parametric modeling of brdf and albedo from multiangular satellite sensor observations. *Remote Sensing Reviews*, 18(2-4):343–379, 2000.
- [30] W. Lucht, C.B. Schaaf, and A.H. Strahler. An algorithm for the retrieval of albedo from space using semiempirical BRDF models. *IEEE Transactions on Geoscience and Remote Sensing*, 38 (2):977–998, March 2000.
- [31] F. Maignan, F.M. Bréon, and R. Lacaze. Bidirectional reflectance of Earth targets: evaluation of analytical models using a large set of spaceborne measurements with emphasis on the Hot Spot. *Remote Sensing of Environment*, 90(2):210 220, 2004.
- [32] J.V. Martonchik, C.J. Bruegge, and A.H. Strahler. A review of reflectance nomenclature used in remote sensing. *Remote Sensing Reviews*, 19(1-4):9–20, 2000.
- [33] T. Motohka, K.N. Nasahara, K. Murakami, et al. Evaluation of sub-pixel cloud noises on MODIS daily spectral indices based on in situ measurements. *Remote Sensing*, 3(8):1644–1662, 2011.
- [34] A. Mousivand, M. Menenti, B.G.H. Gorte, et al. Global sensitivity analysis of the spectral radiance of a soil–vegetation system. *Remote sensing of environment*, 145:131–144, 2014.
- [35] A. Mousivand, M. Menenti, et al. Multi-temporal, multi-sensor retrieval of terrestrial vegetation properties from spectral–directional radiometric data. *Remote Sensing of Environment*, 158:311 – 330, 2015.

[36] A. Mousivand, W. Verhoef, M. Menenti, et al. Modeling top of atmosphere radiance over heterogeneous non-lambertian rugged terrain. *Remote Sensing*, 7(6):8019–8044, Jun 2015.

- [37] F.E. Nicodemus, J.C. Richmond, J.J. Hsia, et al. *Geometrical Considerations and Nomenclature for Reflectance*, page 94–145. Jones and Bartlett Publishers, Inc., USA, 1992.
- [38] J. Qi, Y. Kerr, M.S. Moran, et al. Leaf area index estimates using remotely sensed data and BRDF models in a semiarid region. *Remote Sensing of Environment*, 73:18–30, 07 2000.
- [39] A. Saltelli, M. Ratto, et al. Global sensitivity analysis: the primer. John Wiley & Sons, 2008.
- [40] S.R. Sandmeier and K.I. Itten. A field goniometer system (FIGOS) for acquisition of hyperspectral brdf data. *IEEE Trans. Geoscience and Remote Sensing*, 37:978–986, 1999.
- [41] G. Schaepman-Strub, M.E. Schaepman, T.H. Painter, et al. Reflectance quantities in optical remote sensing—definitions and case studies. *Remote Sensing of Environment*, 103(1):27 42, 2006.
- [42] C. Schlundt et al. Synergetic cloud fraction determination for SCIAMACHY using MERIS. *Atmospheric Measurement Techniques*, 4, 02 2011.
- [43] K. Segl, L. Guanter, F. Gascon, et al. S2eteS: An end-to-end modeling tool for the simulation of Sentinel-2 image products. *IEEE Transactions on Geoscience and Remote Sensing*, 53:1–12, 10 2015.
- [44] J.J. Settle and N.A. Drake. Linear mixing and the estimation of ground cover proportions. *International Journal of Remote Sensing*, 14(6):1159–1177, 1993.
- [45] Y. Shuai, L. Tuerhanjiang, C. Shao, et al. Re-understanding of land surface albedo and related terms in satellite-based retrievals. *Big Earth Data*, 0(0):1–23, 2020.
- [46] I.M. Sobol. Sensitivity estimates for nonlinear mathematical models. *Mathematical modelling and computational experiments*, 1(4):407–414, 1993.
- [47] R. Tripathi, R.N. Sahoo, et al. Inversion of PROSAIL Model for retrieval of plant biophysical parameters. *Journal of the Indian Society of Remote Sensing*, 40(1):19–28, Mar 2012.
- [48] W.J.D. Van Leeuwen, B.J. Orr, S.E. Marsh, et al. Multi-sensor NDVI data continuity: Uncertainties and implications for vegetation monitoring applications. January 2006.
- [49] W.J.D. van Leeuwen et al. MODIS vegetation index compositing approach: A prototype with AVHRR data. *Remote Sensing of Environment*, 69(3):264 280, 1999.
- [50] W. Verhoef. Light scattering by leaf layers with application to canopy reflectance modeling: The SAIL model. Remote sensing of environment, 16(2):125–141, 1984.
- [51] W. Verhoef and H. Bach. Coupled soil–leaf-canopy and atmosphere radiative transfer modeling to simulate hyperspectral multi-angular surface reflectance and TOA radiance data. *Remote Sensing* of *Environment*, 109(2):166–182, 2007.
- [52] E. Vermote, J.C. Roger, and J.P. Ray. MODIS surface reflectance user's guide, 05 2015. Collection 6 - Version 1.4.
- [53] E. F. Vermote, D. Tanre, J. L. Deuze, M. Herman, and J. . Morcette. Second simulation of the satellite signal in the solar spectrum, 6s: an overview. *IEEE Transactions on Geoscience and Remote Sensing*, 35(3):675–686, 1997.
- [54] E.F. Vermote et al. Atmospheric correction of visible to middle-infrared EOS-MODIS data over land surfaces: Background, operational algorithm and validation. *Journal of Geophysical Research: Atmospheres*, 102(D14):17131–17141, 1997.
- [55] F. Vuolo, W. Ng, and C. Atzberger. Smoothing and gap-filling of high resolution multi-spectral time series: Example of Landsat data. *International Journal of Applied Earth Observation and Geoinformation*, 57:202–213, 05 2017.

[56] P. Wang et al. Advanced infrared sounder subpixel cloud detection with imagers and its impact on radiance assimilation in NWP. *Geophysical Research Letters*, 41(5):1773–1780, 2014.

- [57] W. Wanner, X. Li, and A. H. Strahler. On the derivation of kernels for kernel-driven models of bidirectional reflectance. *Journal of Geophysical Research: Atmospheres*, 100(D10):21077–21089, 1995.
- [58] H. Xiang, J. Liu, et al. Algorithms for moderate resolution imaging spectroradiometer cloud-free image compositing. *Journal of Applied Remote Sensing*, 7(1):1 18, 2013.
- [59] Y. Xie, Z. Sha, and M. Yu. Remote sensing imagery in vegetation mapping: a review. *Journal of plant ecology*, 1(1):9–23, 03 2008.
- [60] Y. Zeng, R. Shi, P. Liu, et al. Simulation and analysis of NDVI performance based on vegetation canopy radiative transfer model. In *Remote Sensing and Modeling of Ecosystems for Sustainability XII*, volume 9610, page 961017. International Society for Optics and Photonics, 2015.
- [61] Y. Zeng, J. Li, Q. Liu, et al. An iterative BRDF/NDVI inversion algorithm based on a posteriori variance estimation of observation errors. *IEEE Transactions on Geoscience and Remote Sensing*, 54:6481–6496, 2016.
- [62] X. Zhang, Z. Jiao, et al. Potential investigation of linking PROSAIL with the Ross-Li BRDF model for vegetation characterization. *Remote Sensing*, 10(3), 2018.
- [63] G. Zhou, X. Liu, et al. Estimating FAPAR of rice growth period using radiation transfer model coupled with the WOFOST model for analyzing heavy metal stress. *Remote Sensing*, 9(5), 2017.